



UNIVERSITÀ POLITECNICA DELLE MARCHE
SCUOLA DI DOTTORATO DI RICERCA IN SCIENZE DELL'INGEGNERIA
CURRICULUM IN INGEGNERIA BIOMEDICA, ELETTRONICA E DELLE TELECOMUNICAZIONI

Full-wave analysis and design of opto-mechanical systems

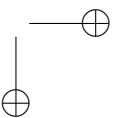
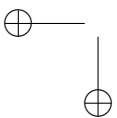
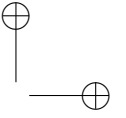
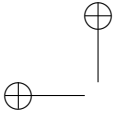
Analisi full-wave e progettazione di sistemi opto-meccanici

Ph.D. Dissertation of:
Matteo Stocchi

Advisor:
Prof. Luca Pierantoni

Curriculum Supervisor:
Prof. Francesco Piazza

XVIII edition - new series





UNIVERSITÀ POLITECNICA DELLE MARCHE
SCUOLA DI DOTTORATO DI RICERCA IN SCIENZE DELL'INGEGNERIA
CURRICULUM IN INGEGNERIA BIOMEDICA, ELETTRONICA E DELLE TELECOMUNICAZIONI

Full-wave analysis and design of opto-mechanical systems

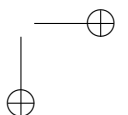
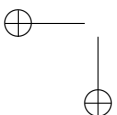
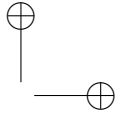
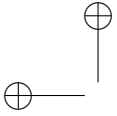
Analisi full-wave e progettazione di sistemi opto-meccanici

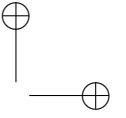
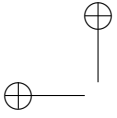
Ph.D. Dissertation of:
Matteo Stocchi

Advisor:
Prof. Luca Pierantoni

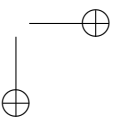
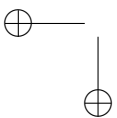
Curriculum Supervisor:
Prof. Francesco Piazza

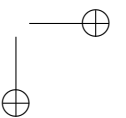
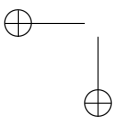
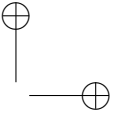
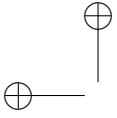
XVIII edition - new series





Ad Anna ed alla mia famiglia...





Acknowledgments

Firstly, I would like to express my sincere gratitude to my advisor Prof. Luca Pierantoni for the continuous support of my Ph.D study and related research, for his patience, motivation, and professionalism. His guidance helped me in all the time of research and writing of this thesis. I could not have imagined having a better advisor and mentor for my Ph.D study.

Besides my advisor, I would like to thank the rest of my thesis committee: Prof. Davide Mencarelli and Prof. Andrea Di Donato, for their insightful comments and encouragement, but also for the hard question which incited me to widen my research from various perspectives.

My sincere thanks also goes to Prof. Daniel Navarro-Urrios, Prof. Yan Pennec, and Prof. Bahram Djafari-Rouhani, who provided me an opportunity to join their team as intern, and who gave access to the laboratory and research facilities. Without their precious support it would not be possible to conduct this research.

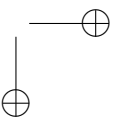
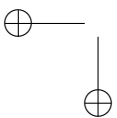
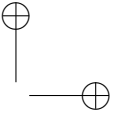
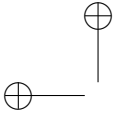
I thank my fellow lab-mates in for the stimulating discussions, for the sleepless nights we were working together before deadlines, and for all the fun we have had in the last three years.

A special thanks goes to my wife Anna: without your support and your positivity, I doubt I would have succeeded in reaching the end of this (for me particularly) tortuous path. The goals achieved belong to you as to me.

Last but not the least, I would like to thank my family: my parents and to my brothers for supporting me spiritually throughout writing this thesis and my my life in general.

Ancona, Novembre 2019

Matteo Stocchi



Ringraziamenti

Innanzitutto, vorrei esprimere la mia piú sincera gratitudine al mio tutor Prof. Luca Pierantoni per il suo costante supporto al mio Ph.D e alla ricerca condotta, per la sua pazienza, motivazione e professionalitá. La sua guida mi ha aiutato sia nel condurre la mia ricerca che nello scrivere questa tesi. Non avrei davvero potuto immaginare un miglior mentore per il mio percorso di studi. Insieme al mio tutor, vorrei ringraziare anche il resto dei componenti del mio team di ricerca: Prof. Davide Mencarelli, Prof. Andrea Di Donato e Prof. Tullio Rozzi per i loro consigli illuminanti e incoraggiamenti, ma anche per i difficili quesiti sollevati che mi hanno incentivato ad approfondire la mia ricerca.

Un sincero ringraziamento va anche ai Prof. Daniel Navarro-Urrios, Prof. Yan Penec e Prof. Bahram Djafari-Rohuani, che mi hanno dato l’opportunitá di aggregarmi ai loro gruppi di ricerca come internship, e che mi hanno dato accesso ai loro laboratori e alle loro facilities. Senza il loro prezioso contributo non sarebbe stato possibile condurre questa ricerca.

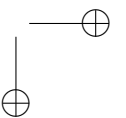
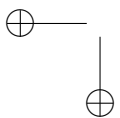
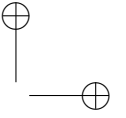
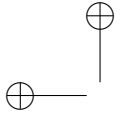
Vorrei ringraziare anche i miei compagni di laboratorio e di corso di dottorato in generale per le discussioni stimolanti, per le notti insonni passate a lavorare insieme prima delle deadline e per tutto il divertimento che, grazie a loro, ha reso questi tre anni speciali.

Un ringraziamento speciale vá a mia moglie Anna: senza il tuo supporto e la tua positivitá, dubito sarei riuscito ad arrivare alla fine di questo (per me particolarmente) tortuoso percorso. I traguardi raggiunti appartengono a te quanto a me.

L’ultimo (ma non per questo meno importante) ringraziamento va alla mia famiglia: ai miei genitori e ai miei fratelli, per avermi supportato lungo tutta la durata del corso di dottorato e lungo il corso della mia vita in generale.

Ancona, Novembre 2019

Matteo Stocchi



Abstract

Optomechanical (OM) micro-cavities are object of intense tudy, as a possible source of new functionalities, concepts, and opportunities beyond standard technology, with regard to microwave phonon propagation, generation, and processing at micro and nanoscale. In this framework, nonlinear OM interaction is being intensively investigated, with a view to advanced device modulation. The above kind of research is highly interdisciplinary, moving along the frontier of many fields, i.e. microwave Surface Acoustic Wave (SAW) filters, photonics, and electronics, and at the boundary between nanophysics and quantum optics. In particular, some recent achievements of OM ground state cooling promise coherent control of the quantum motion of mechanical resonators. A relevant example is provided by the recent coupling of a superconducting qubit to the mechanical vibrations of a piezoelectric resonator, i.e. microwave mechanical resonators operated at the quantum limit. Fundamental mechanisms of OM systems, such as the radiation pressure and the electrostrictive force exerted by electromagnetic fields on the matter, and, reversely, photoelastic modulation of electromagnetic fields, are responsible for strong interactions occurring in resonant cavities. In fact, huge pressures can act in the cavity region, owing to the high Q-factors achievable both for the optical and mechanical modes that coexist in the cavity. The above mechanism yields useful vibrational transduction and actuation at the μ - to m-watt power levels. Also it potentially leads to the development of phonon laser and detectors. Such development is likely to enable processing phonon signal at room temperature and integration of phononic elements on a silicon platform, capable of generating novel ways of information processing. The final objective is using phonons, instead of electrons, as vectors of information and building chips that work at room temperature, analogously to the operation of SAW-based devices, for filtering and sensing applications. Important advantages of this new technology are given, for example, by possible high frequency operation and low power consumption. In addition, comparing with pure nano-electromechanical actuation, the optical approach is less sensitive to capacitive and impedance mismatch issues.

Given the above, the first part of this thesis deals with the theoretical interpretation of the OM phenomenon taking place in high-Q μ -cavities, having the aim of providing a reliable and rigorous approach for maximize the performances of a coherent phonon generator. If to consider the future development and progress of the OM circuitry, having a method capable of providing both the exact phononic population generated in a given cavity and the evaluation of the optical and mechanical forces that play

their role in the interaction between the two physics, will be of fundamental importance. Together with the aforementioned numerical model, that has additionally been ported to a user-friendly application, original cavity designs exhibiting high degrees of confinement of both the optical and the mechanical resonating modes are given.

The second part of this thesis focuses on the optical excitation of the coherent phonon generator, proposing a design made of a Si-slab that is first blended and then selectively etched, so that the evanescent tail of the E-field can be enhanced and, consequently, the EM energy transfer between such slab and the OM cavity can be maximized. This solution not only guarantees better performances in respect to the standard fiber-loop approach, but it is also suitable for an on-chip integration of the phononic generator, given its improved stability and reliability.

Additionally, efforts are put in the investigation of i) the extraction of the coherent phonons generated in the OM cavity, with special focus on the balance between having the need of a high Q-factor (essential for enabling the self-pumped behavior) together with the necessity of generating some mechanical energy leak, and ii) the design of a low-loss waveguide, capable of carrying the phononic information along the chip.

The third part of the thesis introduces the SAW as a valid solution for the phonon processing. At first, the integration between a generic SAW launcher (generally made of a combination of InterDigitated Transciever (IDT), a thin piezoelectric material and a Si-sustrate) and the targeted OM cavity is investigated. A novel design in which the electrical terminals, e.g. where the SAW is generated, have been radially curved for facilitating, from a geometrical point of view, the focus of the mechanical wave towards a certain region is given. Successively, the issue of modeling such curved IDT fingers is addressed. For ensuring a correct calibration of the SAW-launcher, aimed to isolate the latter from the rest of the OM circuitry, a numerical method making use of both the Scattering Matrix (SM) representation and the TRL approach is developed and tested against its analytic counterpart.

Acronyms

MST Maxwell Stress Tensor

OM Optomechanical

EM Electromagnetics

TO Transformation Optics

USTL Lille University of Science and Technology

MI Moving Interfaces

PE Photoelastic Effect

SAW Surface Acoustic Wave

IDT InterDigitated Transciever

SM Scattering Matrix

TRL Through-Reflection-Line

PML Perfectly Matched Layer

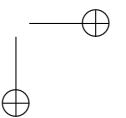
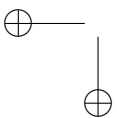
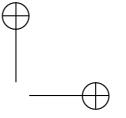
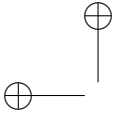
DUT Device Under Test

VNA Virtual Network Analyzer

SM Scattering Matrix

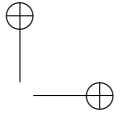
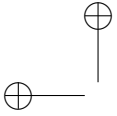
SBS Stimulated Brillouin Scattering

TRL Through-Reflect-Line



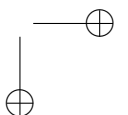
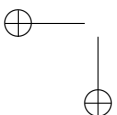
Contents

1	Introduction	1
2	The rigorously coupled model	7
2.1	Theoretical background	7
2.2	The validation of the model	10
2.3	The original OM cavity design	15
2.3.1	Single OM cavity	15
2.3.2	Double OM cavity	18
2.4	The user friendly application	23
3	Concerning coherent phonons detection and generation	29
3.1	Optical characterization of the coupling between a slab waveguide and an OM cavity	29
3.1.1	Setting up the model	30
3.1.2	The nanobeam-OM cavity modes investigation	34
3.1.3	The sensitivity analysis	38
3.1.4	The OM driven phonon resonator	42
3.2	The phononic waveguide	45
4	SAWs as a phonon processing alternative	53
4.1	Conversion between SAW and guided modes of a quasi-periodic structured nanobeam	54
4.1.1	Electromechanical coupling in the system of IDT on piezoelectric layer deposited on Silicon membrane	54
4.1.2	Efficiency of the conversion from RF electrical signal into the guided modes of a straight slab	59
4.1.3	Excitation of cavity modes in a phononic cavity	63
4.2	Through-Reflect-Line (TRL) Calibration of SAW-based devices	65
4.2.1	Preliminary considerations about SAW calibration	65
4.2.2	TRL Theory	67
4.2.3	Numerical test of SAW calibration by TRL	70
5	Conclusions	75
5.1	Numerical methods for the rigorous prediction of an OM based system	75
5.2	Design and optimization of phonon generators and phonon waveguides	76



Contents

5.3 SAW as a phonon processing alternative	77
5.4 Final conclusions	78



List of Figures

1.1	Visualization of an OM interaction	3
2.1	Spatial E-field distribution of the considered optical mode with a focus on the unit cell of the OM crystal.	10
2.2	Qualitative comparison between theoretical and experimental data, as reported in [23], for three different range of frequencies.	12
2.3	Spatial displacement field distribution and parameters of OM interest of the investigated mechanical modes.	13
2.4	Evaluation and visualization of the optical contributions related to the chosen mechanical resonating mode.	14
2.5	Displacement generated from the single components (x and y) of the three force contributions $\mathbf{F}_{ES,B}$, $\mathbf{F}_{ES,V}$ and \mathbf{F}_{RP} taken individually.	14
2.6	(a) OM cavity fabricated on a suspended Si beam; (b) optical scattering parameters through the cavity, (c) spectrum of mechanical-mode resonances around 5 GHz, and corresponding effective masses.	16
2.7	(a) electromagnetic field distribution of the probe signal, (b) magnitude of mechanical displacement \mathbf{u}	17
2.8	Source terms of the mechanical equation, assuming the parameters of Table I.	19
2.9	(a) OM cavity made of two cascaded cavities similar to the cavity simulated in section A. (b) optical scattering parameters through the cavity.	20
2.10	Maximum value of the mechanical displacement, as a function of the frequency, both for single cavity as a function of the frequency, for different values of pump power, both for single cavity and double cavity.	22
2.11	Maximum value of the mechanical displacement, as a function of the frequency, both for single cavity and double cavity.	23
2.12	Snapshot of the graphic user interface of the developed application.	25
2.13	Snapshot of the secondary window related to the <i>Displacement: Resonances</i> result button.	27
2.14	Snapshot of the secondary window related to the <i>E-field: Resonances</i> result button.	28
3.1	Experimental details of a generic OM setup.	30

List of Figures

3.2	Snapshot of the simulated optical structure, where the different excitation ports a), b), c) and d) have been indicated.	31
3.3	Geometric parameters D (nanobeam-OM cavity distance) and W (mirror longitudinal position) swept for the numerical optimization of the optical coupling.	31
3.4	Focus on the advanced mesh configuration adopted for the air gap between the nanobeam and the OM cavity.	32
3.5	(a) Localized modes of the OM cavity, (b) optical quality factor related to each mode, optical quality factor as a function of the optimization parameters (c) D and (d) W.	36
3.6	(a) Transmission curves obtained for an optical frequency of 188 THz and (b) related Electromagnetics (EM) energy density.	37
3.7	Reflection at port 1 (see Fig. 3.2) as a function of the frequency: a) different values of D are assumed while W is kept fixed at 0 nm, b) different values of W are assumed, while D is kept fixed at 230 nm.	39
3.8	Numerical results for the scattering parameters and normalized EM field distribution (zoom on the OM cavity) assuming D = 290 nm and W = 0 nm.	40
3.9	Frequency dependence of the scattering parameters, e.g. reflection (S ₁₁) and transmission (S ₂₁), for different values of D (W = 0 is assumed).	40
3.10	Maximum transmission (S ₂₁), falling at the resonant frequency, as a function of the distance D for different values of W.	41
3.11	Optomechanical coupling ratio between the five optical modes and seven phononic modes.	42
3.12	Max displacement (nm) vs. frequency (Hz) for the investigated mechanical resonating mode.	44
3.13	Scattered E-field (V/m), generated by the fully-coupled method, vs. frequency (Hz).	45
3.14	Plot of the a) displacement field (nm) and b) scattered electric field (V/m) generated by the fully-coupled method.	46
3.15	Evaluation of both the phononic and optical modes, by mean of the fully-coupled model, for the OM configuration as proposed by [28].	47
3.16	Evaluation of both the longitudinal and transverse components of the phononic wave resulting from the OM cavity ([28]) excitation.	48
3.17	Dispersion curves and geometrical parameters of the phononic shield as proposed by [28].	48
3.18	Punctual mechanical excitation aimed to evaluate the behavior of the phononic wave coming our of the OM cavity.	49
3.19	Dispersion curves and geometrical parameters of the phononic shield opportunely designed for the frequency in use.	50

List of Figures

3.20 Evaluation of both the longitudinal and transverse components of the phononic wave resulting from the OM cavity excitation. 50

4.1 Schematic representation of a prototype device for the phonon generation and detection by electrical means using IDT on a piezoelectric AlN film deposited on the Si membrane. 55

4.2 (a) Schematic presentation of the unit cell of IDT. (b) Dispersion curves corresponding to the generation of SAW for different lattice lengths. (c,d) Spatial distribution of the absolute value of the displacement field. 57

4.3 (a) Calculated real parts of the components u_x (top) and u_y (bottom) of the displacement field (in pm) at 2 GHz. (b) The power flux averaged over the nano-plate section at the right side (just before the PML). (c) Efficiency of conversion of RF signal into nanoplate modes. (d) Spatial Fourier transform for symmetric and anti-symmetric waves for a linear cross-section through a nanoplate in the direction of propagation at a frequency of 2 GHz. The resulting wave vectors coincide well with those of the Lamb modes of the 220 nm Si nanoplate at 2 GHz, as shown in panel (e). 58

4.4 The spatial distribution of the absolute value of the displacement field (in pm) for IDT terminated by a slab at 2 GHz. 59

4.5 Dispersion curves of the silicon slab of rectangular section ($a \times e$) = (500 nm \times 220 nm) 61

4.6 (a) Spatial distribution of the x -component of the Poynting vector at 2 GHz. (b) Efficiency of the conversion from the electric signal into mechanical modes of a straight slab. 63

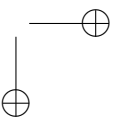
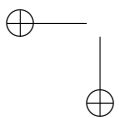
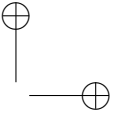
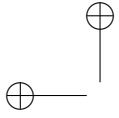
4.7 (a) Band diagram for periodically structured NB with the unit cell presented in the inset. (b) Spectrum of the SAW conversion efficiency for each NB modes and the SAW conversion into all NB modes with S' symmetry. (c) Displacement field distribution (in arbitrary units) for three $S'S$ cavity modes. 64

4.8 (a) Two port circuit, with two electromagnetic ports, plus n mechanical internal ports, (b) detail of the transition from IDT to periodic mechanical waveguide and (c) simulated and structure, with transitions from IDT fingers to periodically patterned mechanical waveguide. . . 68

4.9 Schematic design of the Thru, Reflection, and Line simulations 69

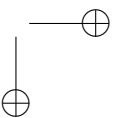
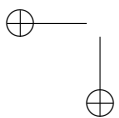
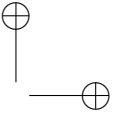
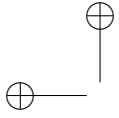
4.10 (a) Simulated $Thru_{11}$ (= $Thru_{22}$); (b) simulated $Thru_{12}$ (= $Thru_{21}$), and (c) power lost in $Thru$ configuration, as a function of the frequency and of the source impedance. 71

4.11 (a) Calibrated parameters of the embedding IDT-to-waveguide transition, (b) net power lost in case of excitation from the mechanical waveguide and from the IDT. 73



List of Tables

2.1	Parameters to which the maximum OM coupling has been observed for the single cavity configuration.	18
2.2	Parameters to which the maximum OM coupling has been observed for the double cavity configuration.	21
3.1	Optical and elastic properties used in the calculation.	35
3.2	Coupling rates related to the Moving Interfaces (MI) effect, the Photoelastic Effect (PE) and the overall OM. for the five optical modes of interest related to the phononic mode at $f_{phon} = 2.41$	43
3.3	Coupling rates related to the MI effect, the PE and the overall OM. for the five optical modes of interest related to the phononic mode at $f_{phon} = 2.0595$	43
4.1	Elastic constants (GPa) and mass density (kg/m^3) for materials used in the simulation.	55
4.2	Symmetry of the first four low frequency modes of the rectangular slab.	61



Chapter 1

Introduction

Recently, the interfacing between optical cavities and mechanical systems has given rise to a rapid development of the research branch called cavity optomechanics, which aims to confine light into small volumes, by the means of an high-Q resonant recirculation [1, 2]. The purpose of an optomechanical system is to investigate the interaction of light with a mechanical oscillator, and its highly interdisciplinary nature leads to several potential applications in various fields of research, especially in quantum processing. Although the electromagnetic radiation has historically been the primary experimental tool for controlling a quantum system and for transmitting and distributing quantum informations, a growing interest in using acoustic or mechanical waves for inspecting quantum control and on-chip quantum communication of artificial atoms has been found. In the recent past, experimental and theoretical analyses have included coherent coupling of Surface Acoustic Waves (SAWs) or mechanical vibrations to superconducting qubits [3], SAW-based universal quantum transducers [4], mechanical quantum control of electron spins in diamond [5], phononic QED [6] and phonon-mediated spin squeezing [7]. The most successful exploitation of mechanical vibrations for quantum control, however, combines both optical and mechanical interactions through phonon-assisted optical or sideband transitions, as demonstrated in trapped ions [8, 9] and, more recently, in cavity optomechanics [10, 11]. Focusing on the latter, optomechanical micro-cavities can also serve as a possible concept to provide new functionalities, applications and opportunities, beyond standard technology, owing to phonon propagation, generation, and processing [12]. Such an application would require low power consumption and, making a comparison with pure nano electromechanical actuation, the optical approach ensures less impedance mismatch issues. Additionally, phonons are an excellent interface to coherently transfer information, for instance, between microwaves and optical photons, between magnons and photons, etc.

In this thesis, which has been developed within the EU FET-OPEN project PHENOMEN, various theoretical approaches and methods have been used for both investigating their efficiency in simulating OM devices and designing novel structures aimed to push the OM-based technology towards its integration with the standard Si technology. The long term vision of PHENOMEN is to *harness the potential of combined*

Chapter 1 Introduction

phononics, photonics and radio-frequency electronic signals to lay the foundations a new information technology based on the manipulation of phonons and their coupling to photons and RF electronics. To this end, PHENOMEN will exploit cavity optomechanics to prove the concept of GHz- frequency phononic circuits in a silicon chip working at room temperature and consuming lowpower.

To this aim, a main action plan has been created for what concerns the theoretical branch of the project working plan, which can be summarized in three main points:

- *to investigate the efficiency of the OM coupling taking place in a Si-based resonant cavity by mean of advanced numerical methods.* Since the ultimate goal of the research is to deliver a phonon-based Si-chip, a phononic laser, e.g. a generator capable of pumping coherent phonon at the desired frequency, is a device of fundamental importance. That said, OM cavities are know to be the best candidates for coherent phonon generation, and even though extensive efforts have been put in order to maximize their efficiency [12,13], much remains to be done to pump phononic devices in any extended circuits.
- *to extract the phononic signal from the OM cavity, by developing a proper phononic waveguide in which the wave is able to propagate in the millimeter scale range.* For efficiently extracting coherent phonons from an OM cavity, a compromise between the level of confinement of the mechanical signal inside the cavity (e.g. its Q-factor) and the outgoing flow of coherent phonons must be found. Successively, a phononic waveguide in which the generated coherent phonons (at a given frequency) can propagate by suffering acceptable losses must be designed.
- *to process the generated phononic information in order to enable a fully phononic driven circuit.* Another fundamental aspect of creating a technology that relies completely on mechanical waves in matters for transferring information is the possibility of *processing* such information. To this aim, novel techniques for manipulating the coherent phononic signal must be found that are, at the same time, integrate with the micro-environment of a Si-chip.

The same logic applied to the three following chapters of this thesis:

- In chapter II, a fully-coupled numerical approach which, combining the two exerted physics of mechanics and optics, accurately predicts the optomechanical dynamics in micro-structured resonant cavities is presented [13]. The rigorosness of such analysis is ensured by considering all the four main energy-transduction contributions [15]. Referring to the two inserts of *Fig. 1*, the radiation pressure and the electrostriction constitutes the forces wielded by the E-field on the matter, whereas the photoelasticity describes the perturbation of the electromagnetic radiation caused by the presence of the mechanical wave.

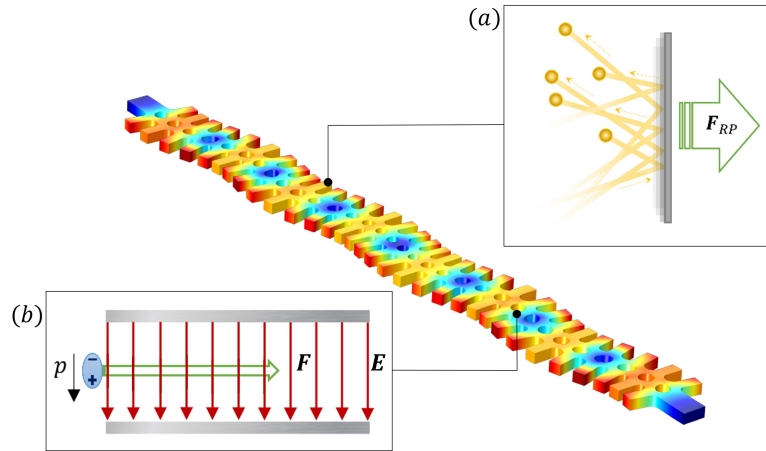


Figure 1.1: Visualization of an OM interaction: the incident electromagnetic radiation generates the two force-like optic contributions of (a) radiation pressure and (b) electrostriction, here presented as the force exerted by the E-field on a molecule [27].

Special considerations are then required for what concerns the so called *moving boundary* effect, i.e. the boundary deformation caused by the space-time-varying pressure field that perturbs the electromagnetic boundary conditions. Specifically, the Eulerian coordinates in which the Maxwell equations are solved are not able to take into account for the mechanical displacement, defined, in turn, in Lagrangian coordinates. As a matter of fact, the just reported limitation can be numerically significant in case of nano-scale cavities. The Transformation Optics (TO) [14, 17] method represents an elegant and efficient solution to the addressed problem. According to its original concept, TO is an analytical tool that facilitates the design of a variety of optical devices (lenses, phase shifters, deflectors, etc.) by deforming the coordinate system, warping space to control the trajectories of the electromagnetic radiation. Such alteration then turns into a change of the electromagnetic material parameters such as the permittivity ϵ and the permeability μ . For the special case of optomechanics, TO is used to take into account for the time-varying boundaries of the domain under investigation [16], making then possible to consider the moving boundary effect by means of a modified version of the standard Helmholtz equation. After having verified the proposed numerical method with experimental results, novel high-Q OM cavity designs will be discussed. In addition to that, the numerical method has been embedded in a user-friendly application, enabling a much simplified investigation of the OM phenomenon.

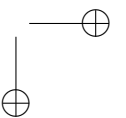
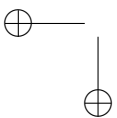
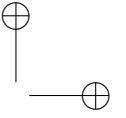
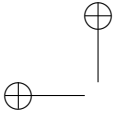
- In the first section of chapter III, the focus is still put on the coherent phonon generator, yet shifted from the evaluation of the OM interaction taking place

Chapter 1 Introduction

in the Si-crystal to the design of a novel way for optically excite the resonant cavity. For overcoming the limitations imposed by the optical fiber loop excitation, where the resulting evanescent field tail (caused by the fiber deformation) couples with the nearly placed cavity, a rigid Si-slab, that exploits the same energy-transfer principle, is preferred. In this way, a more stable structure is made, and apart from an higher generated coupling between the slab and the OM cavity, the designed device can now be easily integrated on a Si-based chip. The optimization of the combined system slab-cavity has been carried out by exciting such structure by mean of multiple numeric ports (one for every terminals), and the mesh has been optimized (by keeping constant the number of mesh elements in between the slab and the cavity) in order to minimize the inevitable numerical errors. For what concerns the optimization variables, it has been chosen to vary i) the slab-cavity distance and ii) the position of the Bragg mirror that has been implemented on the slab for enhancing the EM energy transfer. The second section of chapter III researches on the coherent phonon extraction from the OM cavity, evaluating the efficiency of the proposed cavity design by looking at the Pointing vector of the outgoing mechanical field. Basing upon the work developed in [28], where a phononic waveguide has been build by combining a Si-slab with acoustic-shielding blocks (opportunely tuned to the phononic frequency of interest), a design for a waveguide based upon the proposed OM cavity is presented and tested. It has been found that, thanks to the not excessive Q-factor of the cavity, the leaking of mechanical energy guarantee a good level of coherent phonon generation, that can then be further used as the information-carrying signal in the phononic-based device.

- The first section of chapter IV tackles the issue of processing the state variable of an OM circuit, e.g. the coherent phonon signal, by introducing SAWs in the system. In other words, this work aims to investigate the efficiency of inserting a SAW in an OM cavity. For maximizing the coupling between the mechanical modes of a cavity and the electrically excited SAW, a curved fingers solution for the IDT has been found so that the generated wave could be geometrically focused towards the cavity. The SAW-generator consists on a multilayer structure composed of a Si-substrate, a thin piezoelectric AlN layer and the aforementioned IDT fingers. Apart from representing a valid solution for phonon processing (as demonstrated by [35, 36, 37], where SAW were used for manipulating a 2.4 GHz phononic mode), SAW can serve also as a phonon generator: as first demonstrated by [34], the RF modes of a two-dimensional quasi-periodic phononic cavity made of GaAs have been experimentally excited by mean of SAWs. This additional benefit introduced by the SAW could help considerably in overcoming situation in which the optical excitation of a OM cavity is inconvenient, extending the range of applicability of an OM-based system. The second section of chapter IV focuses on the IDT and on their char-

acterization. A rigorous modeling of the IDTs may be achieved by recurring to numerous analytic methods: circuit models [38, 39] and hybrid electrical and mechanical impedance representation [40] are just two of the many models that can be found in the literature. On the other hand, when the needed level of detail is particularly high, or even when it comes to consider non-conventional IDT geometries, the usefulness of the aforementioned analytic methods may be lacking. For example, one may need to take into account for the metal roughness in miniaturized devices, or, as in our case, the IDT geometry has been engineered for achieving maximum performances in the SAW-OM modes energy transfer. Such issue can be exceeded by mean of a full-wave numerical simulation, and in the present section a calibration of the IDT, based on both the SM representation and the TRL method will be discussed. The importance of developing such procedure lies in the necessity of isolating and de-embedding the acoustic components of SAW-based devices, which in our case are OM cavities, waveguides, and so on.



Chapter 2

The rigorously coupled model

2.1 Theoretical background

From an analytical point of view, optomechanics is described by the combination between the continuum mechanical physics and the classic electrodynamics. The foundations of such a phenomenon rely on the relation [18]

$$\omega_1 = \omega_2 \pm \Omega, \quad (2.1)$$

where Ω is the mechanical frequency and $\omega_{1,2}$ are the optical ones, respectively of the pumped and of the scattered light. Such relation states the exchange of energy between the provided electromagnetic radiation and the mechanical motion, also defining the matching condition for the time-dependent source terms that, as we shall see shortly, enter in the ruling equations of the physics of interest.

A general mechanical wave, whether is it confined in a mechanical cavity or free to propagate, is efficiently described in terms of the displacement \mathbf{u} , i.e. the deformation of a considered elementary cell of the medium under investigation in respect of the relaxation point. The displacement \mathbf{u} satisfies the conservation law of the linear momentum [19]

$$\rho_0 \Omega^2 \mathbf{u} + \nabla_{\mathbf{X}} \cdot (\overline{\overline{FS}}) = -\mathbf{F}_{RP} - \mathbf{F}_{ES,V} - \mathbf{F}_{ES,B}, \quad (2.2)$$

where ρ_0 the mass density of the undeformed configuration, $\overline{\overline{F}}$ the deformation gradient tensor, $\overline{\overline{S}}$ the second Piola-Kirchhoff tensor and $\nabla_{\mathbf{X}}$ indicates the nabla operator expressed in Lagrangian coordinates. The right-side of eq. (2) introduces two of the four aforementioned coupling parameters of an optomechanical phenomenon, i.e. the radiation pressure \mathbf{F}_{RP} and the electrostrictive forces $\mathbf{F}_{ES,V}$, $\mathbf{F}_{ES,B}$, splitted for numerical purpose in their volumetric and perimetric contributions [20]

$$\mathbf{F}_{ES,V} = f_x^{ES,V} \hat{x} + f_y^{ES,V} \hat{y} + f_z^{ES,V} \hat{z}, \quad (2.3)$$

Chapter 2 The rigorously coupled model

$$\mathbf{F}_{ES,B} = (\sigma_{1ij} - \sigma_{2ij})\mathbf{n}_j, \quad (2.4)$$

$$\begin{aligned} \mathbf{F}_{RP} = & -\frac{1}{2}\epsilon_0 E_{t,1} E_{t,2}^* (\epsilon_2 - \epsilon_1)\mathbf{n} + \\ & + \frac{1}{2}\epsilon_0^{-1} D_{n,1} D_{n,2}^* (\epsilon_2^{-1} - \epsilon_1^{-1})\mathbf{n}, \end{aligned} \quad (2.5)$$

where $E_{t,i}$ is the tangential E-field, $D_{n,i}$ the electrical displacement field, ϵ_0 the relative permittivity on vacuum and the individual force components appearing in eq. (3) are given by

$$f_x^{ES,V} = -\partial_x \sigma_{xx} - \partial_y \sigma_{xy} - \partial_z \sigma_{xz}, \quad (2.6)$$

$$f_y^{ES,V} = -\partial_x \sigma_{xy} - \partial_y \sigma_{yy} - \partial_z \sigma_{yz}, \quad (2.7)$$

$$f_z^{ES,V} = -\partial_x \sigma_{xz} - \partial_y \sigma_{yz} - \partial_z \sigma_{zz}, \quad (2.8)$$

and the components of the so called electrostrictive tensor $\overline{\overline{\sigma}}$ are defined as

$$\sigma_{ij} = -\frac{1}{2}\epsilon^2 p_{ijkl} E_k E_l, \quad (2.9)$$

in which we find the strain-optic tensor p_{ijkl} .

Two additional mechanical quantities must be taken into account: the effective mass m_{eff} (so that is possible to study the non-ideal oscillating system as a simple harmonic oscillator) and the thermally-caused initial displacement u_0 . For any considered resonating mode, a numerical estimation of the effective mass is given by [21]

$$m_{eff} = \int \rho_0 |\mathbf{u}|^2 dV, \quad (2.10)$$

where the displacement \mathbf{u} is made dimensionless by normalizing it over its maximum value. At a given temperature T the phonon occupation related to a particular resonant mechanical mode can be estimated, in terms of an initial displacement u_0 , as [22]

$$u_0 = \sqrt{\frac{4k_B T}{m_{eff} \Omega^2}}. \quad (2.11)$$

The effective mass m_{eff} and the resonant mode frequency Ω clearly define the entity of the initial displacement u_0 : The lower they are, the larger is the thermal displacement.

For the general case of an anisotropic and inhomogeneous medium, the electromagnetic field can be efficiently described, as usual, by means of the Helmholtz equation

2.1 Theoretical background

$$\nabla^2 \mathbf{E}_1 = -\mu_0 \omega_1^2 \mathbf{P}_1 = \frac{\mu \omega_1^2}{2} \sum_{kl} \epsilon_{ij}^2 p_{ijkl} \epsilon_{kl} \mathbf{E}_2, \quad (2.12)$$

$$\nabla^2 \mathbf{E}_2 = -\mu_0 \omega_2^2 \mathbf{P}_2 = \frac{\mu \omega_2^2}{2} \sum_{kl} \epsilon_{ij}^2 p_{ijkl}^* \epsilon_{kl}^* \mathbf{E}_1, \quad (2.13)$$

opportunately splitted in the two harmonic components of interest $\omega_{1,2}$ and in which we find the relative permeability μ_0 . The term on the right-hand side of Eq.s (13,14) introduces the mechanical perturbation of the dielectric permittivity due to the photoelastic effect, represented by the strain tensor ϵ_{kl} .

As aforesated, further considerations are needed in order to take into account for the moving boundary effect since Maxwell equations, solved by the full-wave simulator in Eulerian coordinates, are not automatically able to account of the effect of the displacement on the boundaries.

Transmission Optics (TO) [14] offers a valid solution to overcome such a problem. In fact, by considering the general formulation of the TO method where the Jacobian related to the desired coordinate transformation is replaced with the previously introduced deformation gradient $\overline{\overline{F}}$, we have

$$\overline{\overline{\epsilon}}' = \frac{\overline{\overline{F F}}}{\det \overline{\overline{F}}} \overline{\overline{\epsilon}} = \overline{\overline{g \epsilon}}, \quad \overline{\overline{\mu}}' = \frac{\overline{\overline{F F}}}{\det \overline{\overline{F}}} \overline{\overline{\mu}} = \overline{\overline{g \mu}}, \quad (2.14)$$

where we defined $\overline{\overline{g}}$ as the metric tensor, which is composed by six terms of different harmonics

$$\overline{\overline{g}} = \sum_{n=-3}^3 \overline{\overline{g}}_n e^{in\Omega t}. \quad (2.15)$$

By the mean of eq. (15) and eq. (16), it is possible to take into account for both the photoelasticity and the moving boundary effects in the Maxwell equations

$$-\nabla \times \tilde{\mathbf{E}} = \frac{\partial}{\partial t} (\overline{\overline{g \mu}} \tilde{\mathbf{H}}), \quad \nabla \times \tilde{\mathbf{H}} = \frac{\partial}{\partial t} [\overline{\overline{g}} (\overline{\overline{\epsilon}} + \epsilon_0 \Delta \epsilon) \tilde{\mathbf{E}}], \quad (2.16)$$

then, it is straightforward to derive the corresponding modified version of the Helmholtz equations for the considered harmonics

$$\begin{aligned} & \nabla \times \overline{\overline{A}}^{-1} \nabla \times \mathbf{E}_1 - \omega_1^2 \overline{\overline{C}} \mathbf{E}_1 = \\ & = \omega_1^2 [\overline{\overline{K}} \mathbf{E}_1 + (\overline{\overline{D}} + \overline{\overline{L}}) \mathbf{E}_2] - i\omega_1 \nabla \times (\overline{\overline{A}}^{-1} \overline{\overline{B}} \mathbf{H}_2). \end{aligned} \quad (2.17)$$

$$\nabla \times \overline{\overline{A}}^{-1} \nabla \times \mathbf{E}_2 - \omega_2^2 \overline{\overline{C}} \mathbf{E}_2 =$$

Chapter 2 The rigorously coupled model

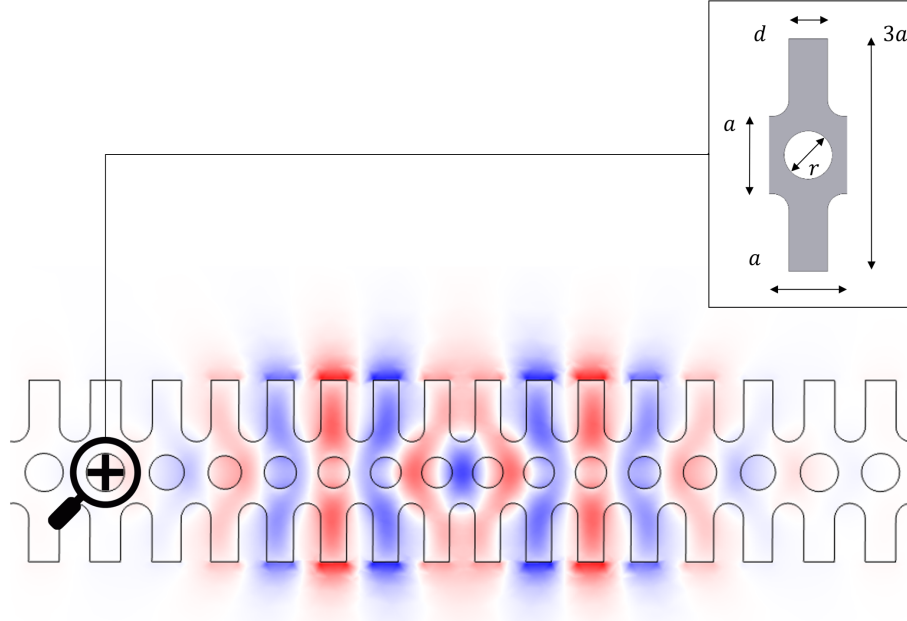


Figure 2.1: Spatial E-field distribution of the considered optical mode with a focus (see the insert) on the unit cell of the OM crystal. The nominal geometrical values of the latter are $a = 500 \text{ nm}$, $r = 150 \text{ nm}$ and $d = 250 \text{ nm}$, with a thickness of 220 nm [27].

$$= \omega_2^2 [\bar{\bar{K}} \mathbf{E}_2 + (\bar{\bar{D}}^* + \bar{\bar{L}}) \mathbf{E}_1] - i\omega_2 \nabla \times (\bar{\bar{A}}^{-1} \bar{\bar{B}}^* \mathbf{H}_1). \quad (2.18)$$

In order to derive a more compact form of the equation, we introduced in the Eq.s (21,22) the following second rank tensors:

$$\begin{aligned} \bar{\bar{A}} &= \bar{g}_0 \mu, & \bar{\bar{B}} &= \bar{g}_1 \mu, & \bar{\bar{C}} &= \bar{g}_0 \epsilon, & \bar{\bar{D}} &= \bar{g}_1 \epsilon, \\ \bar{\bar{K}} &= \frac{\epsilon_0}{2} (\bar{g}_1 \bar{\Delta} \epsilon^* + \bar{g}_1^* \bar{\Delta} \epsilon), & \bar{\bar{L}} &= \frac{\epsilon_0}{2} (\bar{g}_2 \bar{\Delta} \epsilon^* + \bar{g}_2^* \bar{\Delta} \epsilon). \end{aligned}$$

2.2 The validation of the model

In what follows, a validation of the proposed predictive model, pursued by qualitatively regaining and expanding the experimental results obtained in [23] concerning the observation of a breathing mechanical mode at 5.5 GHz in a 1D corrugated Si-based nanobeam, will be given.

Such mechanical mode optomechanically interacts with the optical resonance, of

2.2 The validation of the model

which the E-field norm is shown in Fig. 2.1, through a strong dynamical back-action effect at a room temperature. The unit cell of the OM crystal is a Si parallelogram which presents a cylindrical hole in the center and two symmetric stubs on the side. Such a structure exhibits a full phononic band gap around 4 GHz, as verified in [24]. The geometry of the OM cavity is composed of two mirror regions on the right and on the left sides of the structure which enclose a section where the pitches, the radius and the stubs length of the unit cells have been scaled in a quadratic way towards the center, with a maximum geometrical reduction with respect to the mirror cells of 17%. Both doping and resistivity ρ of the crystalline silicon layer of which the cavity is made (respectively of $\sim 1 - 10 \Omega\text{cm}^{-1}$ and $\sim 10^{15} \text{ cm}^{-3}$) have been incorporated into the conductivity σ , while the anisotropy is modelled by mean of a non-diagonal elasticity matrix. In addition, as aforesaid, an isotropic loss factor of $\xi = 0.001$ has been considered.

A first remarkable difference between the experimental observations and our predictive model is the frequency in which the chosen optical resonance falls: according to the measurements taken by [23], the latter happens to be at $f_{opt,measured} \sim 190 \text{ THz}$, whereas, according to our calculations, $f_{opt,calculated} = 149.17 \text{ THz}$. Such a difference is due to the 2D-environment in which our simulations are carried out, since the loss of the electromagnetic fields confinement in the missing third dimension causes a shift in all the optical resonance frequencies. As we shall see in what follows, such frequency-mode shifting also happens when it comes to consider the mechanical resonances, although not as marked as in the optical case.

The reason why the validation of the coupled OM model was carried out in a 2D-environment must be sought on the computationally convenient cost of the latter. According to the limitations in terms of the mesh maximum element size (which becomes particularly stringent when it comes to resonating phenomena), together with the lack of data comparable in quantitative terms coming from the measurements, it has been chosen to base the qualitative validation on the coupling strength between the mechanical and the EM resonating modes by regaining, for them both, the same field configurations observed experimentally. In other words, the focus of the analysis has been put on the evaluation of the coupling effectiveness between the two selected modes in respect to the others, which may give a practical indication when it comes to chose the working frequencies for both the mechanical and the EM domains. That said, since there are no strict requirements for matching the resonating frequencies in play, in this case the 2D-environment has been preferred.

From the experimental point of view, as a result of the excitation of the considered optical mode, a strong RF transduced signal is observed corresponding to mechanical modes distributions over a spectral range between 10 MHz and 9 GHz [23]. The numerical analysis gives, in turn, the effective enhancement of the displacement associated to the considered mechanical resonances. Although the extrapolated data are not comparable in absolute terms, the juxtaposition of their trends on three different

Chapter 2 The rigorously coupled model

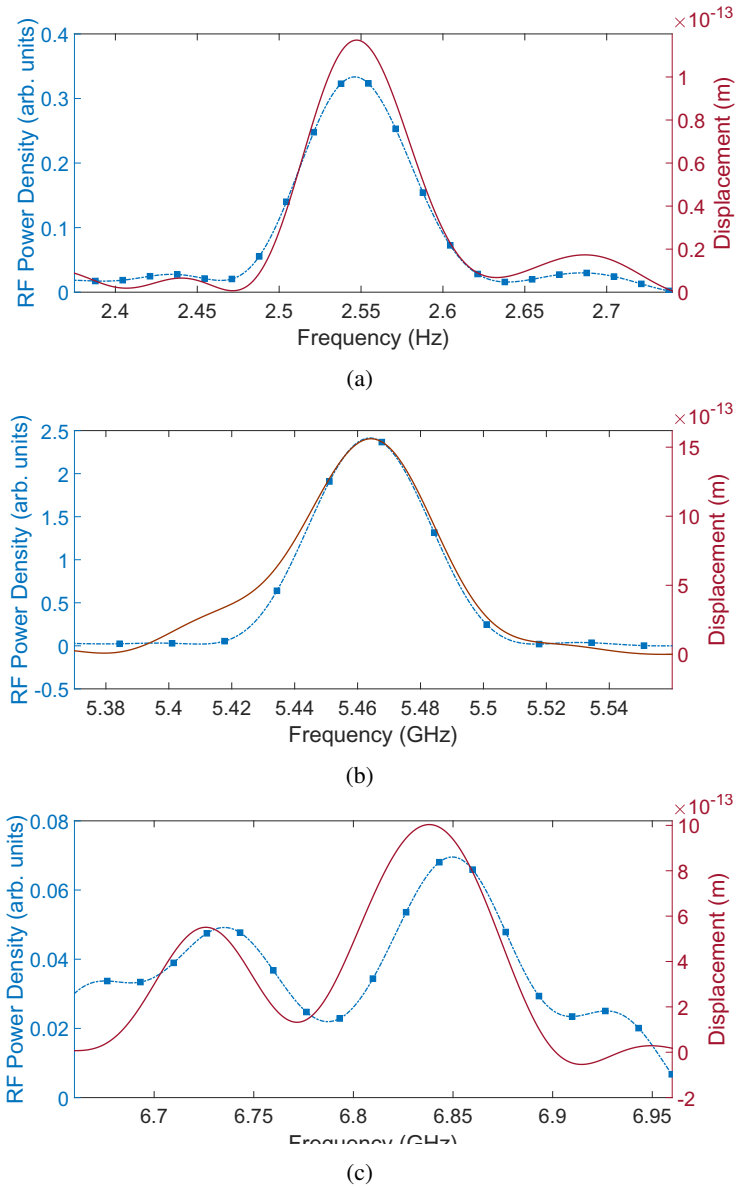


Figure 2.2: Qualitative comparison between theoretical (red dots, m) and experimental (blue triangles, *arb. units*) data, as reported in [23], for three different range of frequencies: (a) 2.35 – 2.7 GHz, (b) 5.36 – 5.56 GHz and (c) 6.65 – 6.95 GHz [27].

2.2 The validation of the model

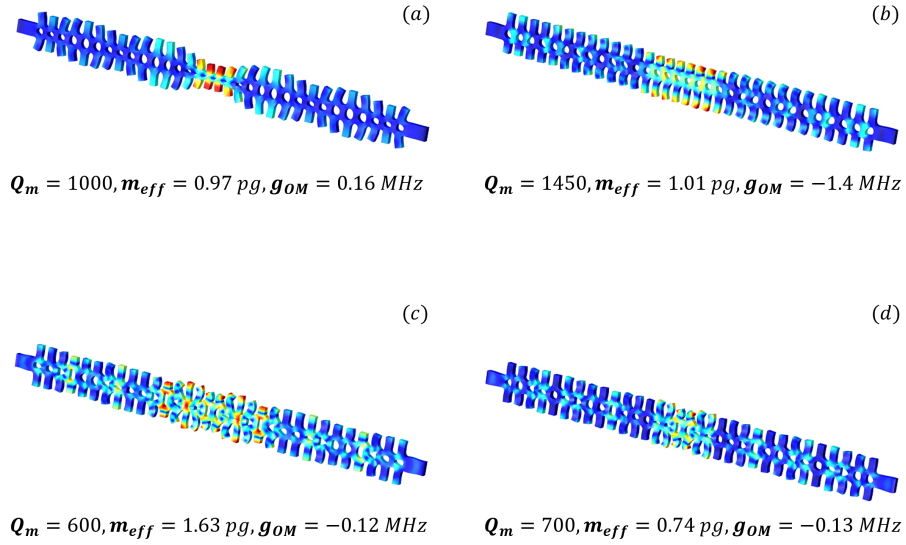


Figure 2.3: Spatial displacement field distribution and parameters of OM interest (effective mass m_{eff} , quality factor Q_m and OM coupling rate g_{OM}) of the mechanical modes resonating at (a) 2.08 GHz, (b) 5.02 GHz, (c) 6.07 GHz and (d) 6.17 GHz related to the peaks shown in Fig. 2.2a, Fig. 2.2a and Fig. 2.2c [27].

intervals of the frequency spectrum of the mechanical modes, as reported in Fig. 2.2, clearly shows a good resemblance. In particular, the four measured peaks in the RF power density spectrum [23] falling at the frequencies of $f_{m,1} \sim 2.5$ GHz, $f_{m,2} \sim 5.5$ GHz, $f_{m,3} \sim 6.65$ GHz and $f_{m,4} \sim 6.75$ GHz are acceptably matched by the ones numerically computed. As afore stated, also in this case a frequency compensation of $\Delta f = 0.5$ GHz has been considered in order to get rid of the limiting bidimensional environment in which the calculations have been conducted.

Focusing on the mechanical mode under investigation, if we consider the thermal displacement $u_0 = 3.21 \cdot 10^{-13}$ m ($T = 300$ K) and an exciting optical power of $P_{opt} = 20$ mW, the OM interaction carried out by means of our numerical simulations leads to a final displacement of $u = 1.55 \cdot 10^{-12}$ m, as shown in Fig. 2.2b.

For the sake of completeness, the spatial displacement field distribution associated to the four mechanical modes taken into consideration is plotted in Fig. 2.3, which also indicates the related parameters of the quality factor Q_m , the effective mass m_{eff} and the OM coupling rate g_{OM} , derived from the classical perturbative approach [25].

Fig. 2.4 shows the modulus of two forces, exerted by the electromagnetic field, of electrostriction (considered both on the boundaries and on the whole volume of the cavity) and radiation pressure and also the displacement u , generated from the OM interaction. It is evident that the highest optically exerted forces occur in correspondence of abrupt discontinuities, which is actually where the displacement field of the

Chapter 2 The rigorously coupled model

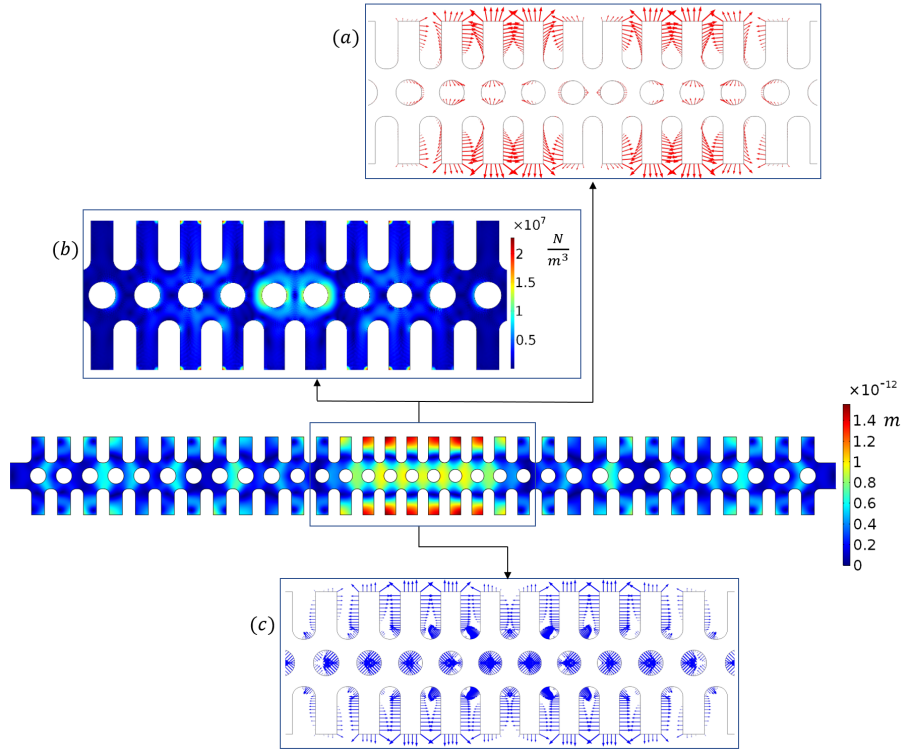


Figure 2.4: Evaluation and visualization of the optical contributions related to the chosen mechanical resonating mode ($f_m = 5.02$ GHz): the electrostrictive force acting on both (a) the boundaries and (b) the volume of the OM cavity and (c) the radiation pressure [27].

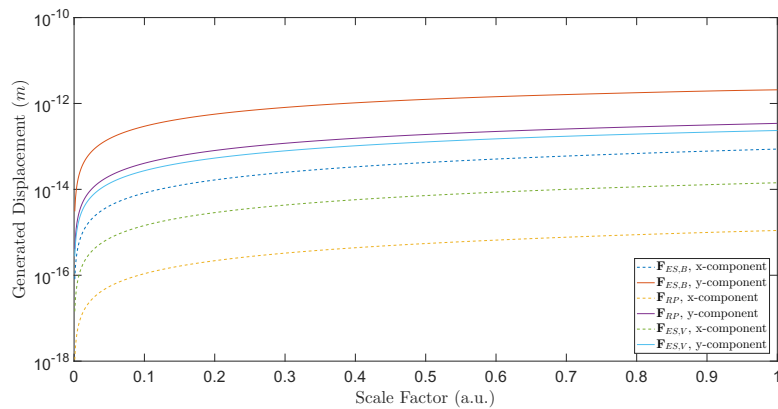


Figure 2.5: Displacement generated from the single components (x and y) of the three force contributions $\mathbf{F}_{ES,B}$, $\mathbf{F}_{ES,V}$ and \mathbf{F}_{RP} taken individually [27].

2.3 The original OM cavity design

mechanical mode under analysis reaches its maximum values. Such congruency constitutes the main reason why the OM coupling between the the two resonating modes, i.e. the optical and the mechanical one, is particularly high.

Further considerations can be made on the effective contribution exerted by the three aforementioned forces by simply taking them individually, as done in Fig. 2.5. By evaluating the single effects of the various force components F_{ES,B^x} , F_{ES,B^y} , F_{ES,V^x} , F_{ES,V^y} , F_{RP^x} and F_{RP^y} weighed by a scale factor, i.e. a multiplier coefficient going from 0 to 1, it is in the first instance possible to notice that the transversal polarization of the optical mode makes the y -contributions much more effective than the x - ones. Secondly, given the field configuration of the mechanical resonance under analysis, the boundary forces generate higher values of the displacement u in respect to the volume ones. According to our calculations, the electrostrictive boundary force results to be considerably higher than the radiation pressure one: the peak values are found to be of, respectively, 7.22 and 2.78 Pa.

Additionally, by observing the values of the maximum displacement $Max(u)$ resulting from the application of the aforelisted individual contributions (especially the one coming from the y -component of the electrostrictive boundary force F_{ES,B^y} ; $Max(u) = 2.08 \cdot 10^{-12}$ m) and the one coming from the fully-coupled OM approach ($Max(u) = 1.55 \cdot 10^{-12}$ m), It turns out that there is no visible cumulative effect, but rather that the electrostrictive and the radiation pressure forces seem to compensate for the effects of each other [26].

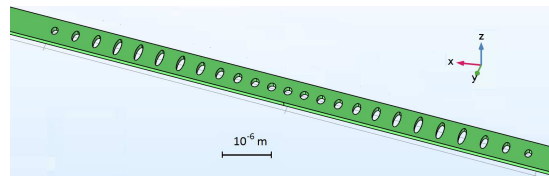
2.3 The original OM cavity design

In what follows, an original design foran OM cavity will be presented. In the first part of this section, the results obtained in [28] concerning the observation of an optomechanical breathing mode localized in the ~ 5 GHz range will be first regained and then expanded by a slight modification of the original cavity design, aimed to reduce the insertion loss of the EM pumped into the OM system [13]. For what concerns the second part of this section, a brand-new design for an highly-efficient OM cavity will be presented.

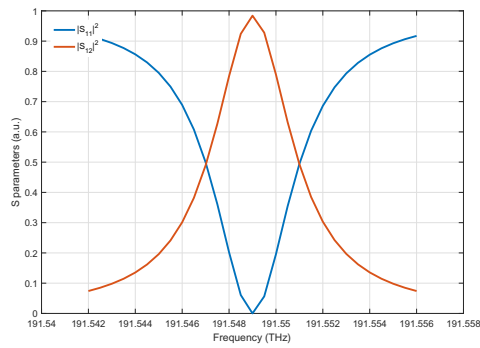
2.3.1 Single OM cavity

By following the same line of the previous section, the consistence of the numerical approach here adopted will be further proven by providing simulated results having direct link to the experiment. More specifically, basing on the design proposed in [28], the following example presents the results obtained by evaluating the OM coupling of an optical/phononic cavity where the resonating modes exhibit both an high-confinement and an high Q-factor (as proven by the dispersion curves shown in [28]).

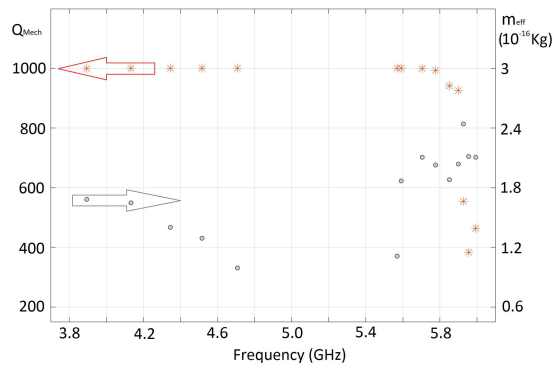
Chapter 2 The rigorously coupled model



(a)



(b)



(c)

Figure 2.6: (a) OM cavity fabricated on a suspended Si beam; (b) optical scattering parameters through the cavity, (c) spectrum of mechanical-mode resonances around 5 GHz, and corresponding effective masses [13].

2.3 The original OM cavity design

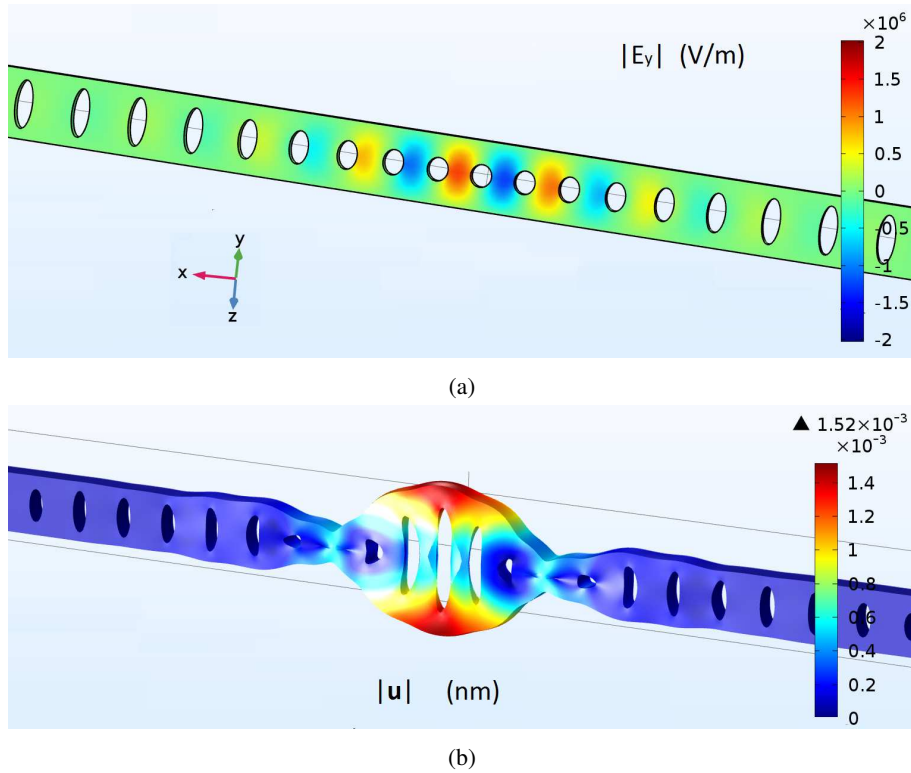


Figure 2.7: (a) electromagnetic field distribution of the probe signal, (b) magnitude of mechanical displacement \mathbf{u} . Pump and probe input powers are assumed as in Table I [13].

The original design of [28] has been slightly modified by applying a tapering on both sides of the cavity: moving towards the outer regions of the structure, the hole diameter of the unit cell have been gradually reduced (see Fig. 2.6), so that the optic signal can penetrate easily through the cavity since there's not an abrupt discontinuity anymore, and so make its way to the inner region.

A first marked difference between the simulations and the experiments comes from the nature of the excitation. If in the experiments the light is pumped at one frequency, in our case two signals (having different frequencies) are launched in both sides of the cavity. The double excitation constitutes a first, marked difference in respect to the study presented in the previous section, where the probe signal (to which we referred as *scattered*) is not effectively pumped in the OM cavity, but rather spontaneously generated by the interaction between the EM pump and the thermally excited phonons oscillating at Ω . The OM phenomenon is simulated by assigning to the probe signal a frequency f_{Opt} which corresponds to the exact resonating frequency of the cavity and to the pump a frequency $f_{Opt} + f_{Mech}$, where f_{Mech} is the frequency of the chosen

Chapter 2 The rigorously coupled model

Table 2.1: Parameters to which the maximum OM coupling has been observed for the single cavity configuration.

f_{Mech}	f_{Opt}	I_{Pump}	I_{Probe}	Q_{Mech}	Q_{Opt}
$5.67 \cdot 10^9$ Hz	$191.549 \cdot 10^{12}$ Hz	$30 \mu\text{W}$	$1 \mu\text{W}$	10^3	$\sim 0.5 \cdot 10^5$

mechanical mode.

All the main parameters of the OM cavity here investigated, namely the optical transfer function and the mechanical spectrum of resonances around a f_{Mech} of 5 GHz (together with their related parameters of interest as the Q-factor and the effective masses) are reported in Fig. 2.6b and Fig. 2.6c.

The parameters to which the maximum OM coupling has been observed are listed in Table 4.1, e.g. both the input pump and probe powers I_{Pump} and I_{Probe} , the exact resonant frequencies (coming from the effective excitation of the cavity) and both the optical and mechanical quality factors Q_{Opt} and Q_{Mech} . It is worth to mention that the maximum coupling has been numerically achieved by keeping the same experimental setup, e.g. by using the given optical and mechanical modes.

The outcomes of the numeric simulations are presented in Fig. 2.7, where both the probe signal and the mechanical displacement (*optically generated*) for the maximum coupling settings are shown. In this case the pump signal has not been plotted since its spatial distribution of the E-field resembles the one related to the probe signal, and furthermore, given the higher pump input power, the OM effect is rather weak.

Also the OM-generated forces are shown in Fig 2.8. The electrostriction bulk force density $\mathbf{F}_{ES,V}$ (which, as expected, reaches its maximum in proximity of the dielectric discontinuities), associated to the TE y-polarized mode resonating in the cavity, is reported in Fig. 2.8a, while the boundary forces $\mathbf{F}_{ES,B}$ and \mathbf{F}_{RP} in Fig. 2.8b and Fig. 2.8c.

Given the high values of the generated displacement \mathbf{u} , one may conclude that the applied tapering doesn't considerably affect the overall coupling strength, which means that both the optical and mechanical fields remain well confined in the inner region of the cavity. On the other hand, the gradual growing of the circular discontinuities has caused a significant reduction in the insertion loss.

2.3.2 Double OM cavity

In what follows, by extending the results obtained in the last section, two optically coupled cavities will be considered. The main goal of putting together two OM cavities may be resumed in creating the right conditions for controlling the coupling rate, and this is done by geometrically tuning the region in which the two cavities have been connected.

The degeneracy of the optical resonance of the individual cavities is broken by the

2.3 The original OM cavity design

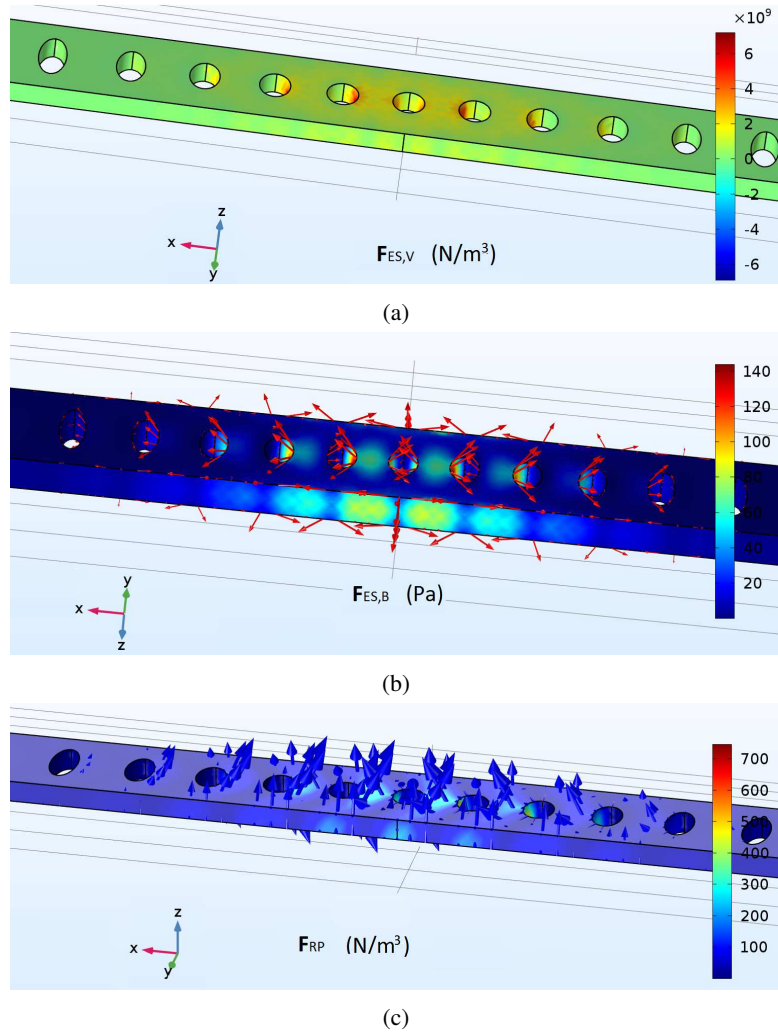
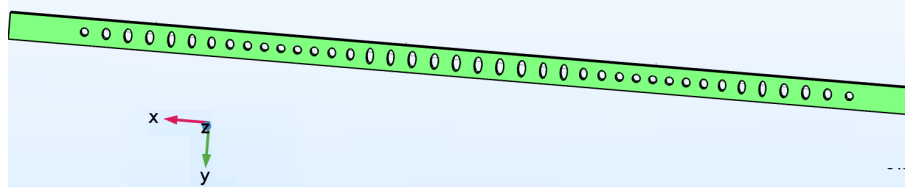
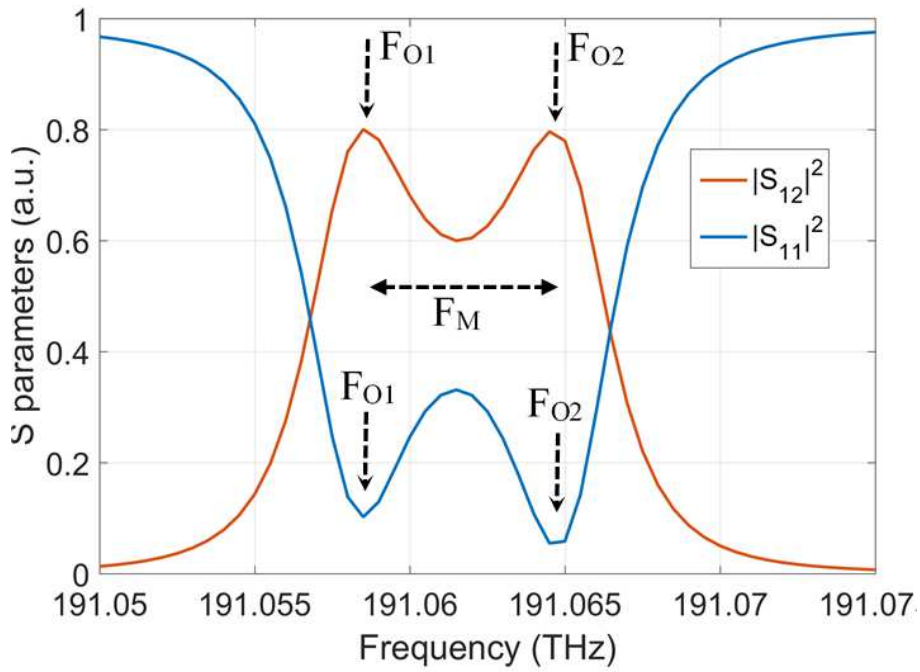


Figure 2.8: Source terms of the mechanical equation, assuming the parameters of Table I: (a) electrostriction contributes in the surface boundaries $F_{ES,V,B}$ (Pa), (b) radiation pressure F_{RP} (Pa), (c) electrostriction contributes in the volume $F_{ES,V}$ (N/m^3) [13].

Chapter 2 The rigorously coupled model



(a)



(b)

Figure 2.9: (a) OM cavity made of two cascaded cavities similar to the cavity simulated in section A. (b) optical scattering parameters through the cavity [13].

2.3 The original OM cavity design

Table 2.2: Parameters to which the maximum OM coupling has been observed for the double cavity configuration.

f_{Mech}	$f_{Opt,1}$	$f_{Opt,2}$	Q_{Mech}	$Q_{Opt,1} = Q_{Opt,2}$
$5.686 \cdot 10^9 \text{ Hz}$	$191.645 \cdot 10^{12} \text{ Hz}$	$191.585 \cdot 10^{12} \text{ Hz}$	10^3	$\sim 0.5 \cdot 10^5$

mutual coupling when the spatial distance between the cavities is reduced: two distinct optical resonances are obtained, corresponding to the two frequencies of the un-degenerate resonances. For numerical purposes, different resonance separations are set by changing the distance between cavities. The proper distance is set by matching the optical frequency separation with the resonant frequency of a specific mechanical mode, as stated in Eq. (6). In a backward SBS configuration, the higher of the two un-degenerate frequencies is populated by the pump field, and the lower frequency gets populated as long as the stimulated scattering is effectively mediated by the phonon amplification. The above effectiveness depends on several factors, namely, the mechanical effective mass, the spatial overlap between the optical beating signal and the mechanical field, as well as their cumulative coupling over the cavity, which generalizes the relation (10) of plane waves [13].

The principal parameters of the double-cavity configuration are listed in Table 4.2, including both the mechanical and the optical frequencies/Q-factors in play.

Fig. 2.9 shows both the geometry and the optical transfer function, in the frequency spectrum of interest, of the investigated OM cavity. Focusing on Fig. 2.9a, it is immediately clear that the two optic resonances are significantly overlapping each other, and that in respect to the peak observed in the single cavity case (see Fig. 2.6b), there has been a downshift in the frequencies at which the resonances fall. The reason for that must be sought in the slight modification of the geometry, which has been reshaped a little bit in order to ensure the same Q-factor as the one of the single cavity. The latter is indeed a key point for correctly evaluating the performances of the proposed double-cavity: the main goal of this analysis was to observe an increase in the overall coupling effect due to the maximization of the optical field intensity of both the pump and the probe signals, made possible by engineering two different resonance peaks at both $f_{Opt,1}$ and $f_{Opt,2}$.

Fig. 2.10 and 2.11 represent the main outcomes of this section, e.g. the comparison between the results obtained with the single OM cavity configuration (in which only the probe signal falls exactly at the resonating frequency of the cavity) and the results obtained with the double OM cavity configuration (in which both the pump and the probe signals are centered at the resonance).

Fig. 2.10 compares the $|S_{11}|^2$ of the probe in the two cases. It is clearly shown that, for regaining the same OM coupling efficiency, the needed input power considerably decreases when passing from the single to the double cavity design.

Together with the reflection, also the generated mechanical displacement is evalu-

Chapter 2 The rigorously coupled model

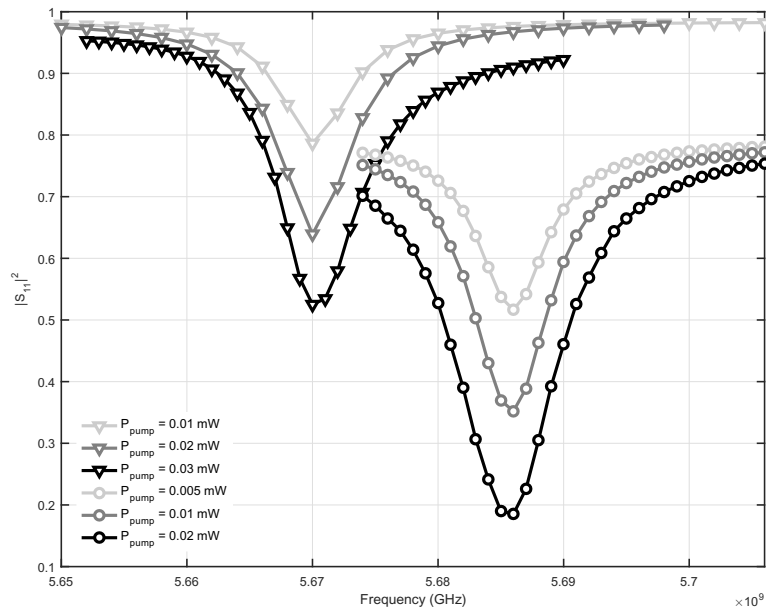


Figure 2.10: Maximum value of the mechanical displacement, as a function of the frequency, both for single cavity (Probe signal reflection ($|S_{11}|^2$) as a function of the frequency, for different values of pump power, both for single cavity (triangles, pump power: [0.01, 0.02, 0.03] mW) and double cavity (circles, pump power: [0.005, 0.01, 0.02] mW) [13].

2.4 The user friendly application

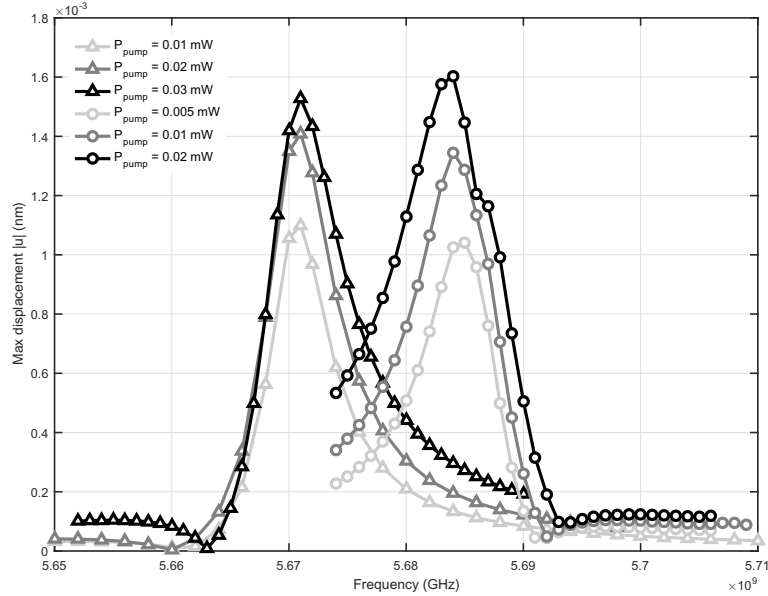


Figure 2.11: Maximum value of the mechanical displacement, as a function of the frequency, both for single cavity (triangles, pump power: [0.01, 0.02, 0.03] *mW*) and double cavity (circles, pump power: [0.005, 0.01, 0.02] *mW*) [13].

ated, and once again the difference between the two configurations is quite marked. The phononic mode intensity is significantly higher when the double cavity design is considered, and this confirms that, if to fulfill the *selection rule* $f_{Opt,1} - f_{Opt,2} \sim f_{mech}$ by making so that both the optical frequencies fall in a resonance peak, the OM amplification is maximized.

As a conclusive note, it must be underlined that although the trends of both Fig. 2.10 and 2.11 are clear (meaning that the main concept of the conducted analysis has been numerically proven), serious convergence issues have been faced when the OM coupling gets too strong. As a consequence, it was not possible to give an optical excitation of more than 0.02 *mW* for the double cavity configuration.

2.4 The user friendly application

In order to facilitate the usage of the herein-above model, capable of rigorously simulate the interlacing physics of mechanics and EM for a generic dielectric structure, the latter has been transferred to a user-friendly application. Such application is intended

Chapter 2 The rigorously coupled model

to serve as an interface between the "lab-reality" and the theoretical investigation, thus allowing researchers having different backgrounds the access to an objectively challenging design tool.

Given the completely customizable geometry, the user can achieve the maximum coupling between the mechanical and EM resonating modes by tuning the most characteristic geometrical parameters of a generic OM cavity such as its length, width, etc.

It must be underlined that, since the application has been completely realized in COMSOL Multiphysics®, an active license of such full-wave simulator is indeed needed.

As shown in Fig. 2.12, the developed application has been organized in four different sections: i) Material Properties, ii) Input Parameters, iii) Geometrical Properties and iv) Computation and Results.

- **Material Properties:** in this section, all the electromagnetic (relative permeability ε_r , relative permittivity μ_r and electrical conductivity σ_e), mechanical (Young's modulus E , mass density of the not-deformed configuration ρ_0 and Poisson's ratio U) and purely OM (photoelastic tensor p_{ijkl}) parameters of the material cavity are incorporated.
- **Geometrical Properties:** this section guides the user in designing and optimizing the desired OM cavity. It is possible to engineer both the fundamental (cavity length, cavity width, cavity height, wing width etc.) and the advanced geometrical parameters. Focusing on the latter, for both the discontinuities and wing height curvature coefficients is possible to define a number between 0 and 1 that will model the growth gradient between the first and the last elements of the array.
- **Input Parameters:** In this section, the mechanical and the electromagnetic frequencies (obtained by running a preliminary eigen-analysis for both the physics), together with the electromagnetic input power, can be defined in order to simulate the OM-coupling in the designed resonant cavity. It must be underlined that only the electromagnetic signal needs to be pumped in the OM-cavity since the application, for a given mechanical eigen-frequency Ω , automatically evaluates its effective mass for then computing (at the given temperature of 273 K) the phonon occupation in terms of an initial displacement u_0 .
- **Computation and Results:** this section presents a list of sixteen buttons in total, conceptually divided into three categories: the geometry visualization buttons, the evaluation buttons and the result buttons. The geometry visualization buttons shows the geometrical entities which are relevant from a computational point of view, as the boundaries in which the surface forces (i.e. the radiation pressure and the boundary electrostrictive forces) are defined and the volume in

2.4 The user friendly application

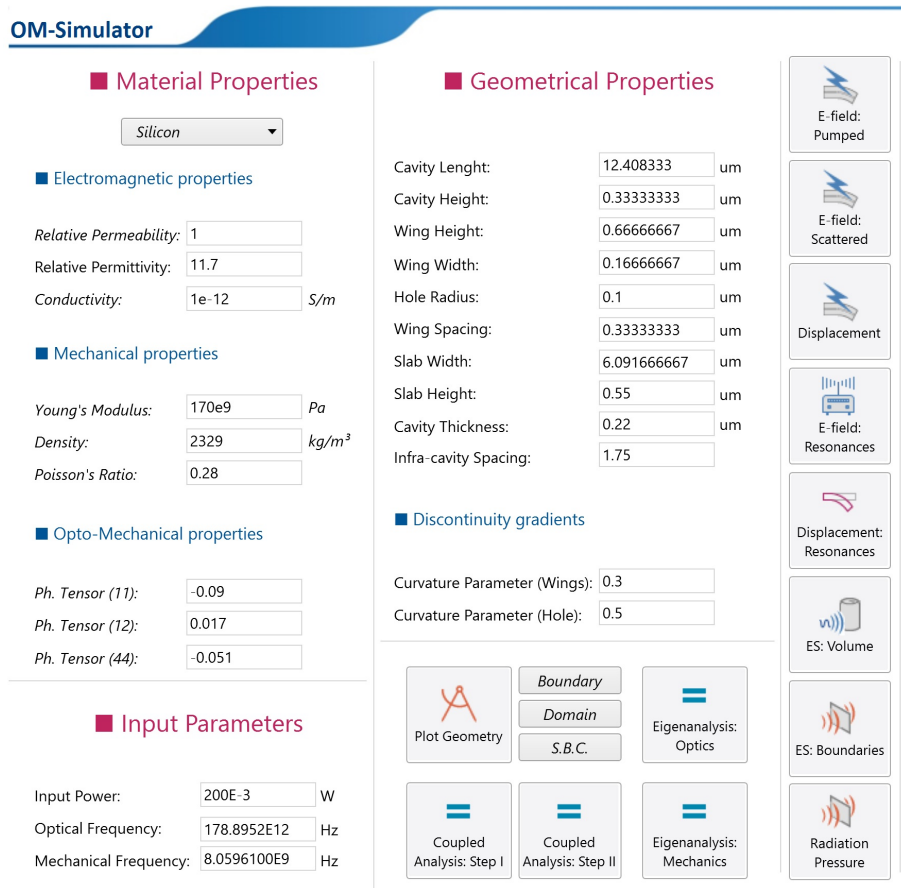


Figure 2.12: Snapshot of the graphic user interface of the developed application. Four sections can be easily distinguished: The Material Properties section, in which it is possible to specify the physical characteristics of the sample taken into examination, the Geometrical Properties section, the Input Parameters section, in which frequencies (both optic and mechanical) and the laser input power are defined and the Computation and Results section [29].

Chapter 2 *The rigorously coupled model*

which the OM coupling takes place. The evaluation buttons allow the user to choose between three different studies: two eigenfrequency studies defined for both the electromagnetic and the mechanical modules, so that is possible to identify the various resonances of the resonant cavity under investigation, and one study which solves for the actual fully-coupled OM phenomenon. The result buttons display the previously computed quantities of interest such as the fields distributions and the OM coupling forces. Focusing on the latter, two different sub-categories of result buttons can be distinguished.

- The *E-field: Pumped*, *E-field: Scattered*, *Displacement*, *ES: Volume*, *ES: Boundaries* and *Radiation Pressure* result buttons plot, in a secondary window, the fields computed by the fully-coupled OM phenomenon, so that is possible to evaluate their entities.
- o The *E-field: Resonances* and *Displacement: Resonances* result buttons plot, in a secondary window, the resonating modes founded by the two eigen-frequency studies defined for both the EM and the mechanical modules, as shown in Fig. 2.13 and Fig. 2.14. The quality factor corresponding to each resonating mode can also be evaluated for both the electromagnetic and mechanical modules, while the effective mass can only be computed for the mechanical one.

2.4 The user friendly application

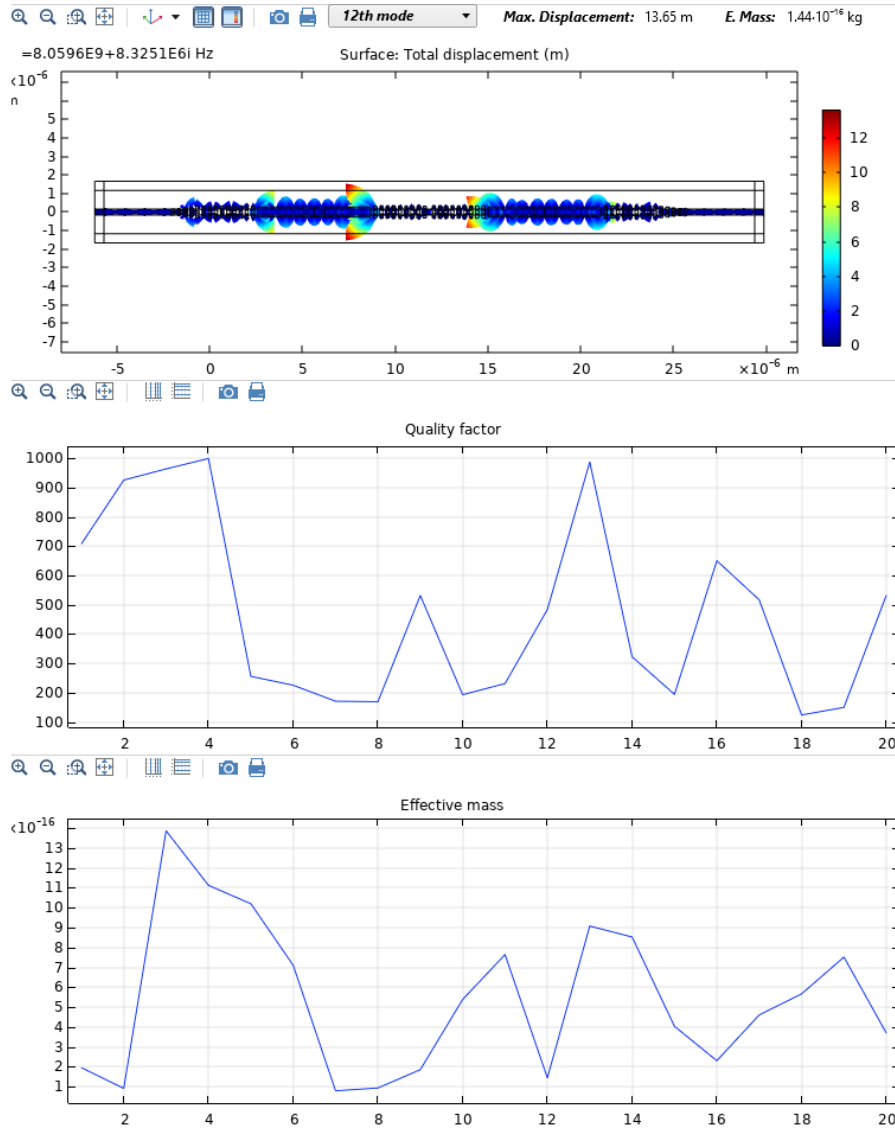


Figure 2.13: Snapshot of the secondary window related to the *Displacement: Resonances* result button, where for each mechanical resonating mode, it is possible to evaluate its corresponding i) field distribution (selectable from the drop-down menu positioned above the field plot), ii) quality factor and iii) effective mass [29].

Chapter 2 The rigorously coupled model

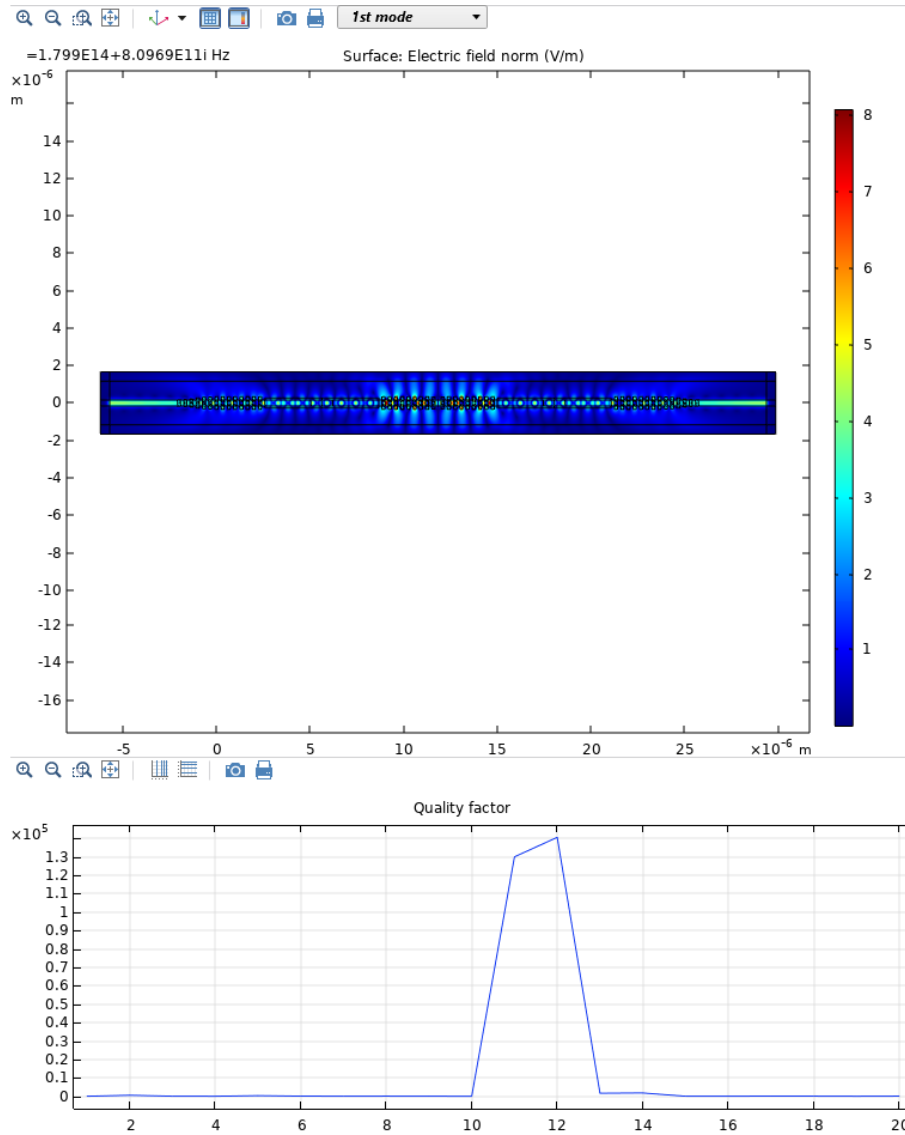


Figure 2.14: Snapshot of the secondary window related to the *E-field: Resonances* result button, where for each electromagnetic resonating mode, it is possible to evaluate its corresponding i) field distribution (selectable from the drop-down menu positioned above the field plot) and ii) quality factor [29].

Chapter 3

Concerning coherent phonons detection and generation

3.1 Optical characterization of the coupling between a slab waveguide and an OM cavity

After having presented, in the herein-above chapter, the fully coupled numerical model capable of rigorously simulate the OM phenomenon in resonant μ -cavities, in what follows foundations will be laid for what concerns the optical excitation of an OM cavity and the generation, as well as the detection, of coherent phonons.

Typically, an OM cavity is excited by mean of evanescent light coming from a tapered optical fiber [23] (which works, in our particular context, at room temperature and at atmospheric pressure): a μ -loop is formed by manually twisting the fiber, giving rise to an evanescent tail of the E-field in close proximity to the section in which the curvature of the loop reaches its minimum, as shown in Fig. 3.1. Although such method has been tested numerous times in multiple environments and excels for simplicity and pragmatism, if to consider a context in which the OM cavity should serve as an integrated component capable of both generating and detecting coherent phonons, an alternative solution must be found. The precarious balance of the fiber loop would constitute a serious limitation when transferring a general OM apparatus from a lab-environment to an industrial reality, in terms of both mechanical stability of the thin optical fiber itself and strong variability the one would have in the entity of the EM coupling between the fiber and the OM cavity.

A possible solution for overcoming such issues is to create an embedded device in which a slab waveguide is placed alongside the OM cavity, as shown in Fig. 3.2. In the proposed configuration, the light would still be injected by mean of an optical fiber, but rather than being the evanescent light source itself, the latter would be connected to the aforementioned slab waveguide. The EM energy transfer now occurs between the OM cavity and the slab, and thanks to the mechanical stability of the latter (which totally cancel the manual tuning of the fiber μ -loop position), the variability of the EM coupling between two different samples considerably drops. Furthermore, having

Chapter 3 Concerning coherent phonons detection and generation

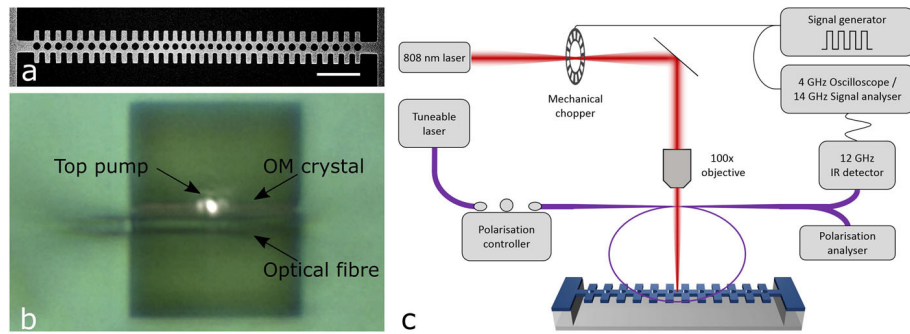


Figure 3.1: Experimental details of a generic OM setup. (a) SEM image of an OM crystal, here in shape of a suspended Si nanobeam. Scale bar is $2 \mu\text{m}$. (b) Optical image showing a top view of the OM crystal with the fiber below and the pump laser spot. (c) Schematic of the evanescent fiber coupling measurement system [23].

the aim of maximizing the EM energy transfer, the slab waveguide has been tapered at the same height as the center of the OM cavity (e.g., where the chosen optical resonating mode is supposed to be trapped), so that a quasi-static wave arises. This causes a consistent drop of the overall slab transmission (S_{21}) in the region of interest, meaning that, if to neglect the radiation losses, the slab-OM cavity coupling will be maximized when the reflection (S_{11}) will be minimized.

3.1.1 Setting up the model

This section provides hints on how the model for performing a rigorous analysis of the optical coupling between a suspended Si nanobeam optical waveguide and a suspended Si resonant cavity, defined by a quasi-periodic structure consisting on repeated holes and *wings*, with proper taper in its central region. Such taper is needed to provide a considerable optical confinement with high resonant quality. The objective of the present simulation run is to maximize the strength and the efficiency of the optical coupling between the OM cavity and the slab waveguide, also referred to as nanobeam given the presence of numerous discontinuities. To this aim, two main parameters are being considered for optimization, namely the distance D between the nanobeam and the OM cavity and the position of the mirror (measured from the center of its smaller hole) with respect to the center of the OM, indicated by W . It is worth to mention that the width of the nanobeam has been chosen to be identical to the one of the OM cavity, so that the fundamental propagating mode has the same degree of confinement. Both the herein-above introduced optimization parameters are shown in Fig. 3.3.

In the following, a qualitative view of the general numerical trend of the optical coupling is reported as a function of D and W , with a view to the quality factor and the resonance frequency. In order to provide an estimation of the coupling, it is important

3.1 Optical characterization of the coupling between a slab waveguide and an OM cavity

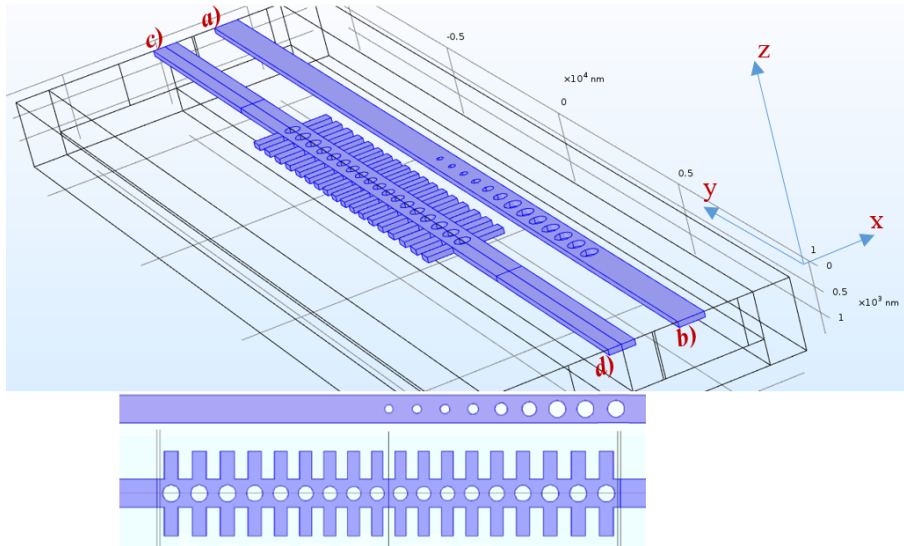


Figure 3.2: Snapshot of the simulated optical structure, where the different excitation ports a), b), c) and d) have been indicated.

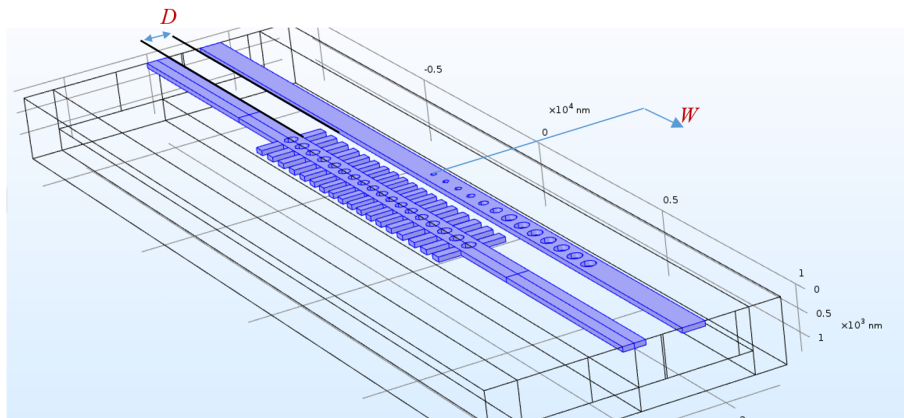


Figure 3.3: Geometric parameters D (nanobeam-OM cavity distance) and W (mirror longitudinal position) swept for the numerical optimization of the optical coupling.

Chapter 3 Concerning coherent phonons detection and generation

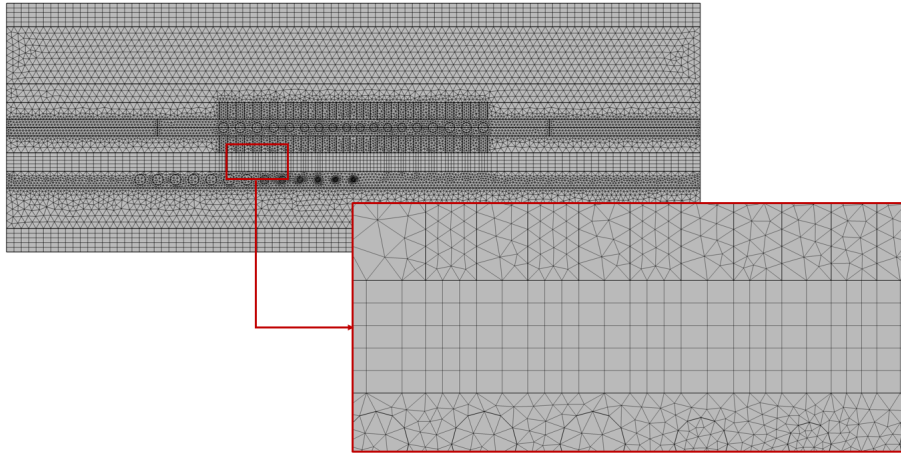


Figure 3.4: Focus on the advanced mesh configuration adopted for the air gap between the nanobeam and the OM cavity.

to check the maximum strength of the electromagnetic field of the resonant mode in the cavity. The higher the field, the larger the expected OM coefficient calculated from the field overlap with the mechanical modes resonating in the cavity. Importantly, it should be noted that experimental conditions can slightly differ from ideal simulations, and this is due to mechanical tolerances, fabrication limits, statistical fluctuations of the electromagnetic parameters, material roughness, dielectric discontinuities.

Moreover, the above simulations are quite challenging as they present at least three different but concurring problems, which we are strongly amplified (numerically) by the high Q resonance of the cavity:

- The mesh: the geometrical sweep, aimed to maximize the coupling strength, necessarily passes from creating a different mesh configuration for every optimization step, and this may cause, in the worst case, a change in the output variables that may overcome the one caused by the behavior of the E-field itself. As mentioned above, such undesired effect is generally amplified when it comes to analyze structures in which the gradient of the optical field is sufficiently high.

In order to overcome such issue, advanced mesh considerations must be given to the air gap existing between the nanobeam and the OM cavity (which clearly is the most delicate region, in terms of field distribution, in the entire model), and each performed geometrical sweep should be addressed singularly.

The W sweep, e.g. the longitudinal sweep of the nanobeam discontinuities, is not expected to create considerable problems in terms of mesh. If to apply a fine, standard mesh composed of tetrahedrons, the holes shift shouldn't affect too much the overall mesh configuration in the critical region of the air gap.

The same argument does not apply when treating the D sweep, e.g. the sweep of

3.1 Optical characterization of the coupling between a slab waveguide and an OM cavity

the distance between the nanobeam and the OM cavity. In this case, the reduction (as well as the increment) of the mesh elements in the air gap may lead to misleading configurations for the optical fields, and such a change is definitely not easy to control since it directly comes from the mesh optimization algorithm implemented in any EM-simulator. If, for example, the distance between the wings of the OM cavity and the holes of the nanobeam (which are known to be regions where the mesh element size is squeezed down to its minimum limit) is reduced, the tetrahedrons placed in the air gap will be relatively small because of the maximum element grow rate setting, making the region of interest densely populated in terms of mesh elements.

The opposite result would be achieved when the two optical devices are set at a larger distance from each other. In this case, the mesh optimization algorithm will let the tetrahedrons to grow as much as both the maximum element grow rate setting and the effective distance D allow, resulting in a scarcely populated region.

Clearly enough, the E-field may be considerably affected by these changes because, in the unfortunate case in which the gradient of the field is high, different mesh configuration will provide different description of the optical evolution along the region of interest, and some of them may simply not provide enough elements to properly describe such evolution.

A possible solution to overcome such critical issue is shown in Fig. 3.4. Basically, the gap region is demarcated from the overall air domain, and only here, instead of meshing freely with the standard tetrahedral option, a sweep of the boundary mesh from the upper OM cavity region down to the lower nanobeam one is performed. In such way, the number of mesh element in the gap can be easily managed, and most importantly, even if the distance D changes, this only results in a stretching of the elements themselves, which keeps their overall density constant.

- The excitation ports: when exciting a structure such as an optical waveguide, a waveport (also referred to as numeric port in COMSOL) is by far the best choice. While a lumped port only considers an area in which the E-field is assumed to be constant, a waveport automatically runs an eigen-analysis for identifying the allowed modes for a certain geometrical configuration at a certain frequency, and excites only the desired ones. Another remarkable difference between the two kind of ports is that the lumped one cannot detect higher-order modes (both in transmission and in reflection), which leads to a wrong interpretation of the overall reflection caused by both the nanobeam and the OM cavity mirrors, while the waveport does it naturally.

That said, the waveport comes with few downsides, and among them, the most critical for the present analysis is that the area on which the port is defined

Chapter 3 Concerning coherent phonons detection and generation

should be big enough to correctly catch the slab guided mode. Although such obligation does not particularly affect most of the optical modeling, in our particular case, given the presence of two nearby ports, the issue becomes rather significant. Additionally, the distance D is to be swept, which further restricts the potential extension of each port side.

That said, it is noted that there is no guarantee that a good compromise for the port size is possible, but in the worst case scenario, different approaches are possible. For example, one may think to extend the computational domain to allow a proper calibration of the EM field excitation coming from the waveports.

- radiating boundary: even a small reflection from the radiating boundary (let say, even 1% or less) could strongly impact the final results due the high Q of the cavity, so PML thickness and distance can become critical parameters. In order to overcome this issue, several tests have been made varying PML thickness and position, until consistent and repeatable results have been obtained.

3.1.2 The nanobeam-OM cavity modes investigation

Before going deep in the optical optimization of the coupled configuration nanobeam-OM cavity, it is mandatory to perform a preliminary analysis aimed to identify the high- Q optical modes such structure can support. Even though the OM cavity has been extensively characterized in multiple occasions from both a theoretical and an experimental point of view, the resonant frequency of the targeted mode may be slightly shifted due to the presence of the nanobeam, which is capable of perturbing the EM characteristics of the isolated OM cavity system.

In this section, a systematic study of the optical response of several resonating modes related to the structure under investigation will be done. Such study has been carried out in collaboration with the phononic research team of Prof. Yan Pennec, from Lille University of Science and Technology (USTL). Most of the calculations have been voluntarily performed in a totally independent manner, so that their outcomes could be directly compared. In general, a good accordance has been found: small numerical differences (for instance, $< 1\%$ for the resonant frequency) are due to different mesh strategies and different boundary settings, that can vary from study by study but do not void the main results of the analysis.

With reference to Fig. 3.2 and Fig. 3.3, the optical device that has been considered in this analysis consists of the OM cavity and of the slab waveguide, also referred to as nanobeam, with the latter used to excite the resonant eigenmodes. The previously introduced optimization parameters D and W , which refer, respectively, to the distance between the nanobeam and the OM cavity and to the distance between the first hole of the Bragg mirror and the center of the nanobeam, will be considered in the following analysis. The optical and elastic properties used in the calculation are exactly the same as the one used in the fully-coupled analysis presented in the previous chapter, and are

3.1 Optical characterization of the coupling between a slab waveguide and an OM cavity

Table 3.1: Optical and elastic properties used in the calculation.

	$C_i(m/s)$	$C_t(m/s)$	$\rho_0(kg/m^3)$	p_{11}	p_{12}	p_{44}	n
<i>Si</i>	5845	8440	2330	-0.1	0.01	-0.051	3.48

also shown in Table 3.1 for convenience. In this study, the USTL research team calculated the following quantities: the optical quality factor, the optical transmission and the OM coupling by using the standard first-order perturbation method.

Fig. 3.5a presents the electric field modulus associated to the eigenmodes of the cavity, which are symmetric with respect to the xy plane. In this case, the following geometrical parameters have been considered: $D = 450$ nm and $w = 0$ nm. Clearly, the mode 5, which resonates at a frequency ~ 188 THz, represents the best choice when aiming to maximize the OM coupling because of both its significantly high Q-value (as shown in Fig. 3.5b) and the field configuration, which remains confined in the inner region of the resonating cavity.

By sweeping the optimization parameters, it has been noted that as the distance D between the OM cavity and the nanobeam increases, the values of the quality factor and the frequency of the photonic modes increase as well, as shown in Fig. 3.5c. This may be caused by the simple fact that by putting the nanobeam as far as possible from the OM cavity the perturbation effect gets negligible, which results in an increase of the overall performances of the cavity since the latter may now be assumed as ideally isolated. Nevertheless, although an increase of the D -parameter is beneficial in terms of Q-factor, one must not forget that such parameters also plays a fundamental role when it comes to effectively excite the OM cavity: if the distance between the latter and the nanobeam gets too large, it is expected that the evanescent tail of the E-field would become too weak for properly transfer the EM energy from one configuration to the other.

Concerning the effect related to the sweep of the parameter W (Fig. 3.5 (d)), it has been noticed that the frequency of the optical modes remains almost constant while the quality factor presents a non-linear variation (Note: the calculation of the effect of w on the quality factor and the frequency was performed with $D = 550$ nm).

Fig. 3.6 shows the optical transmission/reflection (Fig. 3.6a) and the energy density (Fig. 3.6b) related to the mode 5 in respect to a sweep of the optimization parameter D . A first difference between the analysis conducted above and the one of which the results are shown in Fig. 3.6 lies in the nature of the numerical simulations itself: while in the first case an eigen-analysis has been carried out, in the second case waveports defined at the edges of the computational domain have been effectively excited. In this case, the reflection is related to the port 1 (e.g. the excited port) and the transmission to the port 4, so that is possible to evaluate the efficiency of the coupling. Fig. 3.6a shows both the transmission and reflection for different values of the D -parameter, while the red numbers related to each step of the sweep represents the overall radiation losses.

Chapter 3 Concerning coherent phonons detection and generation

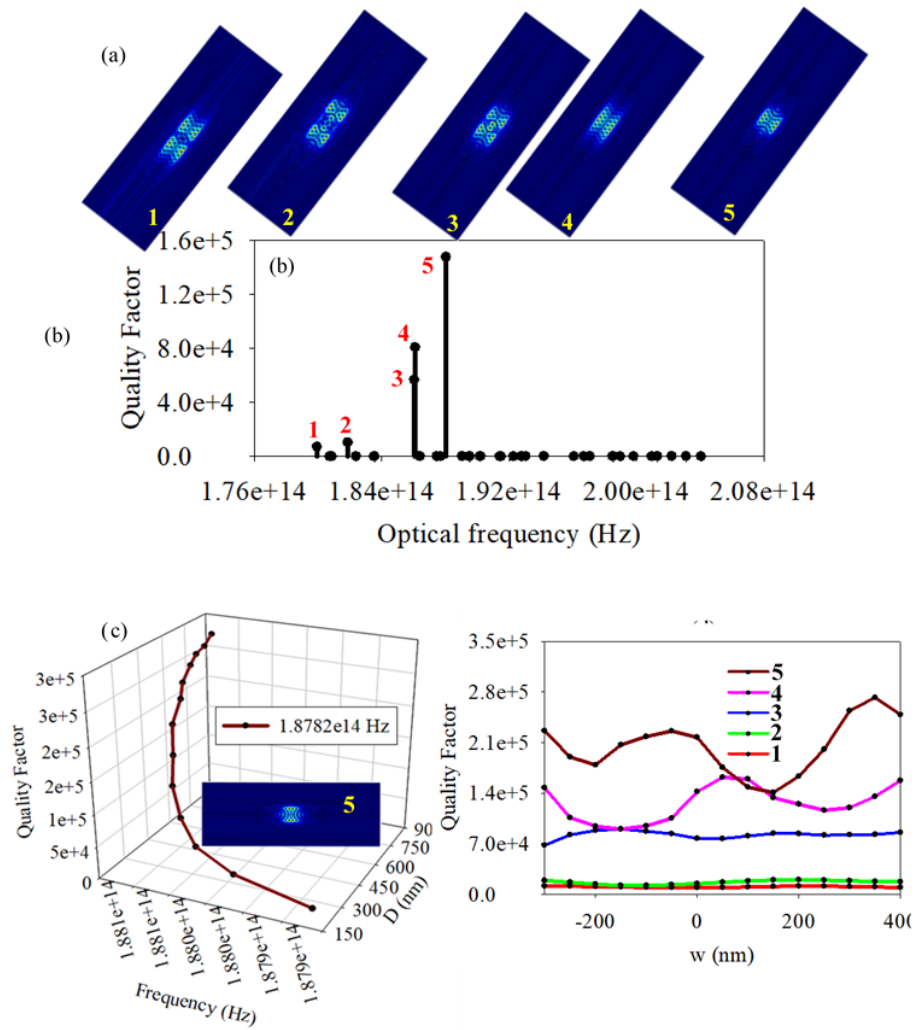


Figure 3.5: (a) Localized modes of the OM cavity, (b) optical quality factor related to each mode, optical quality factor as a function of the optimization parameters (c) D and (d) W.

3.1 Optical characterization of the coupling between a slab waveguide and an OM cavity

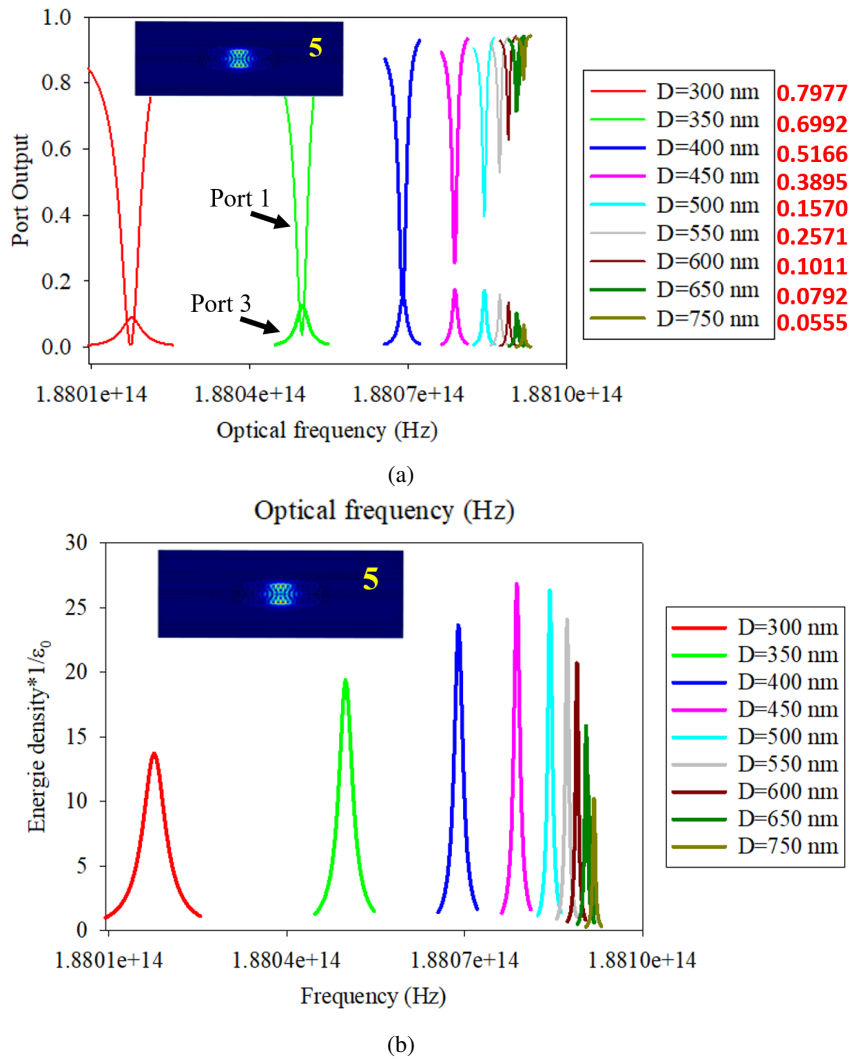


Figure 3.6: (a) Transmission curves obtained for an optical frequency of 188 THz and (b) related EM energy density. The colors indicate the distance between the photonic crystal and the optical waveguide.

Chapter 3 Concerning coherent phonons detection and generation

As aforesaid, even though large values for the distance between the nanobeam and the OM cavity ensures an high-Q mode, there's a specific D-parameter range in which the coupling is maximized, and such a range is observed to fall around the value of 450 nm (e.g. where the transmission is maximized). A further confirmations comes from the evaluation of the EM energy density stored into the OM cavity (see Fig 3.6b): also in this case, the peak is reached when $D = 450$ nm.

3.1.3 The sensitivity analysis

In what follows, a sensitivity analysis on the optical performances of the coupled system OM cavity/nanobeam will be performed, and the results gained above concerning the mode 5 will be extended and deepened.

By keeping the same simulation setup that generated the outcomes shown in Fig. 3.6, the input reflection only is reported in 3.7, and in this case both the D- and the W-parameters are swept. Fig. 3.7a extends the results of 3.6a by reducing further the D-parameter, while Fig. 3.7b focuses on the reflection variation in respect to a sweep of the W-parameter. One can think that, in general, is preferable to keep the longitudinal shift of the Bragg mirror to 0: it actually seems that if to slightly vary the W-parameter, either in the positive or in the negative values of the x -axis, the reflection gets dramatically worst. However, as it will be shown in what follows, the evaluation of the reflection alone is not enough for having a clear understanding of the overall coupling phenomenon.

For completeness, Fig. 3.8 shows the EM-field distribution in the whole computational domain, in correspondence of the resonant frequency, for the particular case where $D = 230$ nm and $W = 0$ nm. The pedices of the scattering parameters S_{ij} are set in accordance to the port definition of Fig. 3.2.

A more complete overview of the trend of the optical response of the system with respect to the optimization parameters is provided in Fig. 3.9, where both reflection and transmission peaks, for different values of the D-parameter, are reported together for having a better comparison.

In order to estimate the best conditions for the optical coupling we need to take into account two main effects: 1) the lower the distance D the better the coupling, but, consequently, 2) the lower the quality factor Q of the cavity, due to optical leak from the OM cavity to the nanobeam. In general, an optimum distance D can be found, as reported in Fig. 3.10. As also shown in the latter figure, the optimum distance changes for different values of W. As a matter of fact, a higher transmission (S_{12}) corresponds to a higher resonant field inside the optical cavity. In conclusion, for the considered cavity, and for the considered resonant mode, the best condition in terms of field strength in the cavity is given by W in the range 200 – 300 nm, $D \sim 550$ nm.

3.1 Optical characterization of the coupling between a slab waveguide and an OM cavity

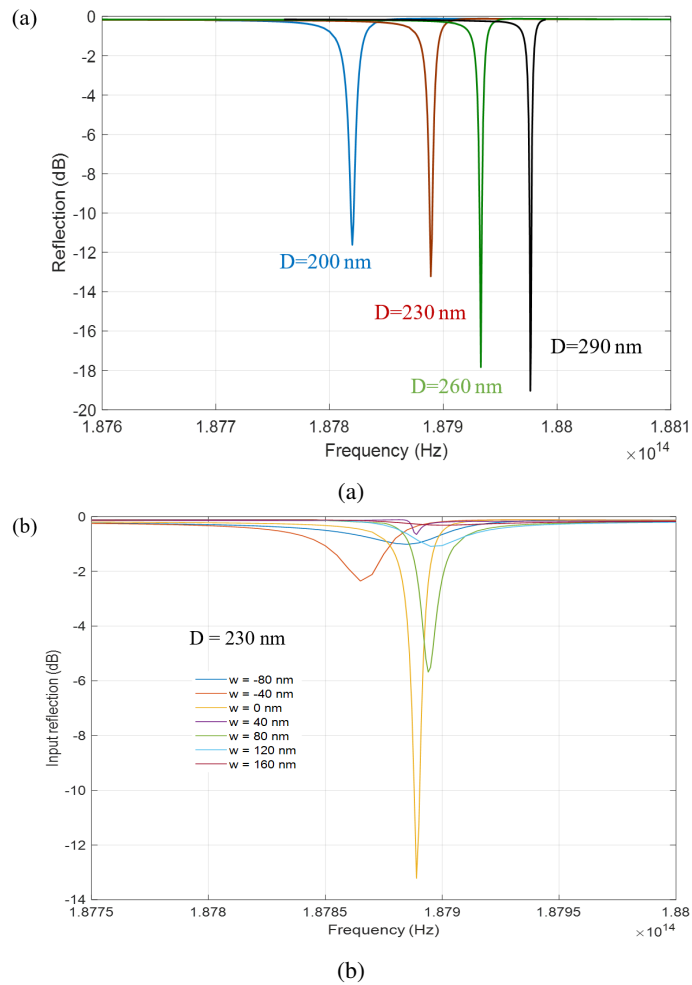


Figure 3.7: Reflection at port 1 (see Fig. 3.2) as a function of the frequency: a) different values of D are assumed while W is kept fixed at 0 nm, b) different values of W are assumed, while D is kept fixed at 230 nm.

Chapter 3 Concerning coherent phonons detection and generation

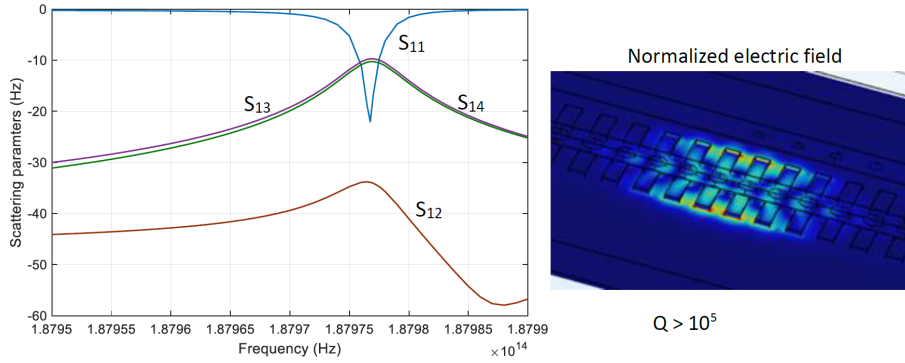


Figure 3.8: Numerical results for the scattering parameters and normalized EM field distribution (zoom on the OM cavity) assuming $D = 290$ nm and $W = 0$ nm.

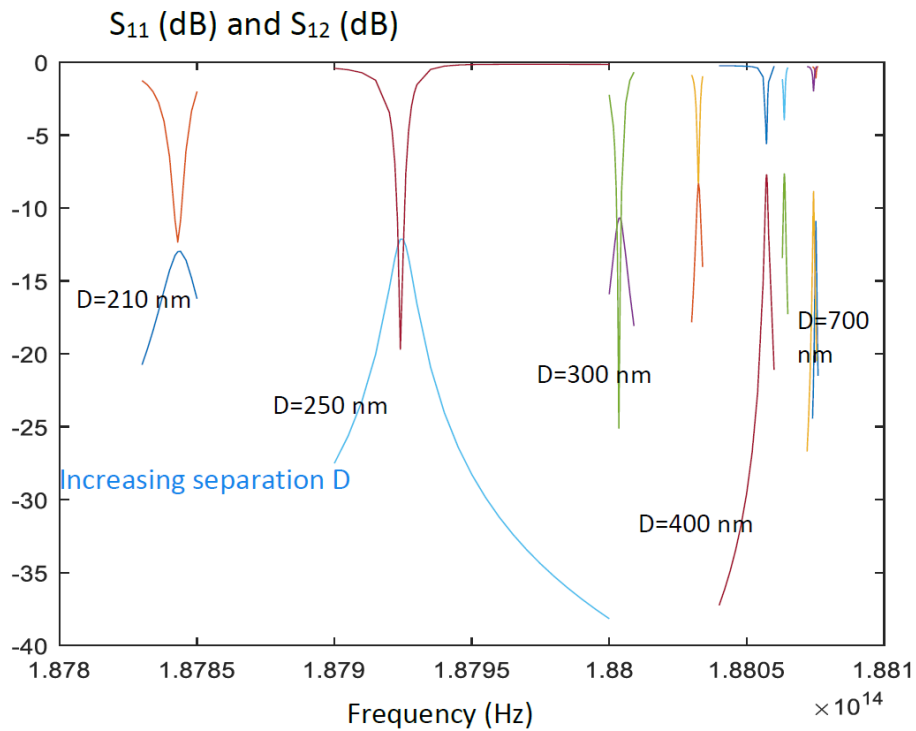


Figure 3.9: Frequency dependence of the scattering parameters, e.g. reflection (S_{11}) and transmission (S_{21}), for different values of D ($W = 0$ is assumed).

3.1 Optical characterization of the coupling between a slab waveguide and an OM cavity

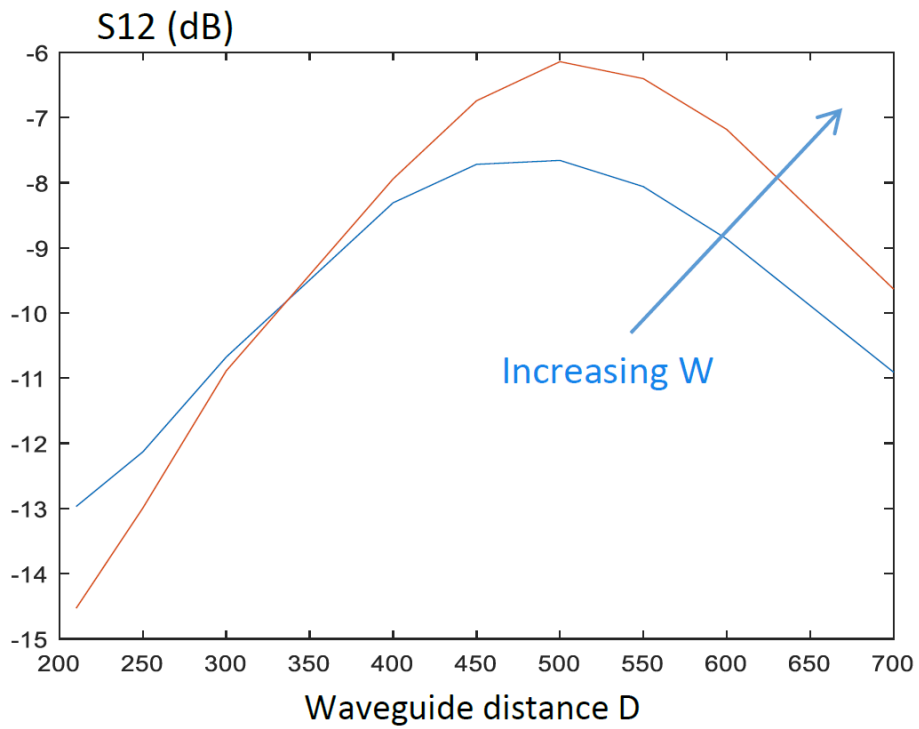


Figure 3.10: Maximum transmission (S_{21}), falling at the resonant frequency, as a function of the distance D for different values of W , namely $W = 0$ nm (blue) and $W = 40$ nm (red). It is evident that a higher effect (e.g. maximum transmission) is obtained as W increases.

Chapter 3 Concerning coherent phonons detection and generation

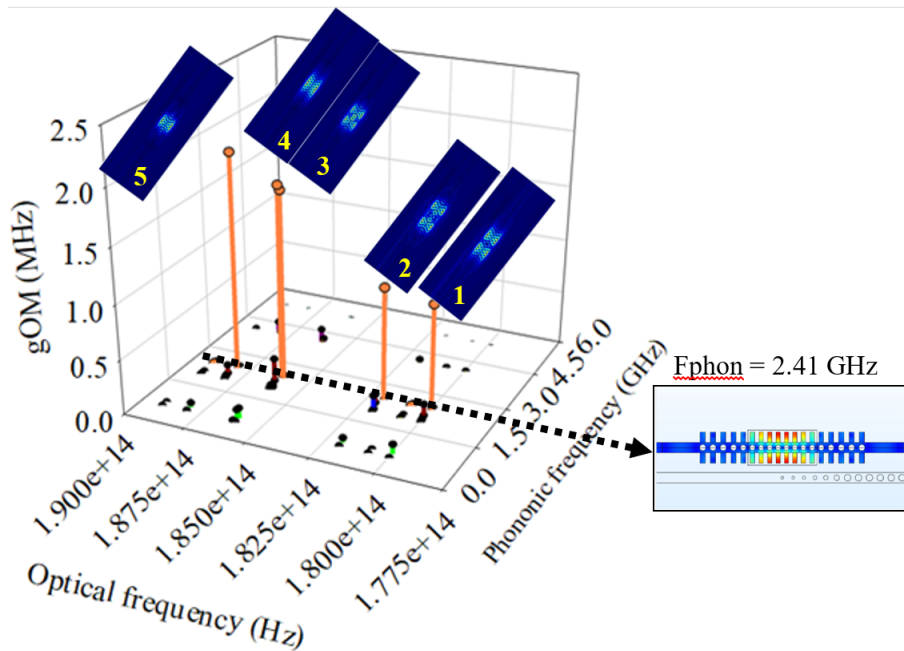


Figure 3.11: Optomechanical coupling ratio between the five optical modes and seven phononic modes.

3.1.4 The OM driven phonon resonator

Basing on the results that have been given in the previous section, where a deep understanding of the optical behavior of the system composed by an OM cavity coupled to a nanobeam (e.g. a slab waveguide in which a Bragg mirror has been applied) has been pursued, in what follows the proper OM phenomenon will be investigated for both the chosen optical mode and the optimized geometrical configuration. By considering both Fig. 3.10 and Fig 3.6b), which refer, respectively, to the overall transmission evaluated on the port 2 and to the EM energy density confined into the resonating cavity, it is observed that an eligible geometrical configuration for the analysis of the effective OM coupling is the one where the $D = 450$ nm and $W = 0$ nm. Even though it was numerically proven that by slightly increasing the W -parameter the presence of the E-field in the cavity is accentuated, it is preferable, from a merely technological point of view (e.g. for not developing an additional mask for the lithography), to select the $W = 0$ nm configuration.

The OM phenomenon will be addressed by mean of two different method: i) the standard first-order perturbation method and ii) the fully-coupled method already discussed in the previous chapter. As a first step, the standard perturbative approach has been used for identifying the mechanical modes having an acceptable coupling factor with the chosen optical mode, e.g. the previously discussed mode 5. As shown in Fig.

3.1 Optical characterization of the coupling between a slab waveguide and an OM cavity

Table 3.2: Coupling rates related to the MI effect, the PE and the overall OM. for the five optical modes of interest related to the phononic mode at $f_{phon} = 2.41$

Opticalmode	MI(MHz)	PE(MHz)	OM(MHz)
1	0.3611	0.6164	0.9760
2	0.4240	0.6173	1.0403
3	0.6589	1.0752	1.7342
4	0.6454	1.1340	1.7766
5	0.7082	1.2914	1.9941

Table 3.3: Coupling rates related to the MI effect, the PE and the overall OM. for the five optical modes of interest related to the phononic mode at $f_{phon} = 2.0595$.

Opticalmode	MI(MHz)	PE(MHz)	OM(MHz)
1	-0.0139	-0.1252	-0.1391
2	0.2016	-0.0638	0.1378
3	-0.2471	-0.0174	0.2645
4	-0.0467	0.0387	-0.0081
5	0.0584	0.0507	0.1091

3.11, the OM coupling rates between the phononic mode located at $f_{mech} = 2.41$ GHz and the optical modes found in the usable range are significantly high, and as expected, given the fact that both the mechanical and the optical field are strongly confined in the inner region of the cavity, the coupling rate peak is reached by considering the mode 5.

For the sake of clarity, the coupling rates related to the MI effect, the PE and the overall OM one are displayed in the Tables 3.2 and 3.3 for the five optical modes of interest and for two different phononic modes at, respectively, $f_{phon} = 2.41$ and $f_{phon} = 2.0595$ GHz.

After having identified, for the given system, the two modes that guarantees the strongest OM coupling by computing the various coupling rates, the effective entity of such interaction can be quantified by adopting the fully-coupled model. The importance of such analysis is not limited to the acknowledgment of the real entity of the mechanical deformation, which can indeed be a fundamental information in order to design an adequate phononic communication system, but also to step closer to the experiments in respect to the perturbative approach. While the latter only relies on eigen-analysis for evaluating the efficiency of the OM coupling in a given configuration, the coupled approach effectively excites (both in the optical and in the mechanical senses) the structure, meaning that the constitutive equation of the two physics involved are rigorously solved in their coupling and so that the two kind of fields are condition each other.

A first example of what has just been said may be found in Fig. 3.12. Here, only the phononic excitation is considered (meaning that only the mechanical physics is solved, while the EM one has been switched off), and the maximum displacement detected in the inner region of the cavity is plotted against the excitation frequency,

Chapter 3 Concerning coherent phonons detection and generation

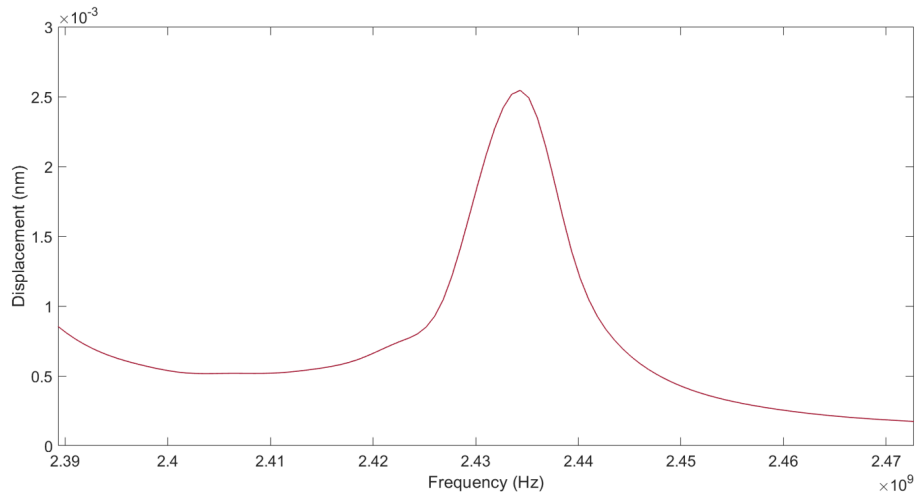


Figure 3.12: Max displacement (nm) vs. frequency (Hz) for the investigated mechanical resonating mode.

performed by mean of a boundary load. It is observed that the selected phononic mode ($f_{phon} = 2.41$ GHz) is, in truth, slightly shifted (~ 25 MHz) with respect to what the eigen-analysis has shown in the previous studies. As we shall see in the next section of the present chapter, such shift may constitutes a serious problem when it comes to design additional phononic structures as, for example, a phononic waveguide aimed to carry out from the cavity the OM-generated phononic signal.

Fig. 3.13 evaluates the maximum value of the norm of the scattered component of the E-field (generated from a fully-coupled analysis) in respect to the optical frequency. Although, in principle, the model setup is the same as the one discussed in section 1.2, where an optical pump and a mechanical excitation have been set up having as objective the observation of the optomechanically generated scattered signal, it is worth to mention that in this case the optical waveport that has been switched on is the number 1 (having the input power of 20 mW), e.g. the one related to the nanobeam. The mechanical excitation, on the other hand, has been kept as a boundary load on the edge of the cavity, and it has been opportunely tuned for matching the thermal phononic population at the given frequency. For generating the trend of Fig. 3.13, the mechanical frequency f_{phon} has been varied so that the maximum OM coupling could be observed in the peak of the intensity of the scattered E-field. Interestingly enough, such peak doesn't fall at 2.434 GHz, e.g. the phononic resonant frequency observed in Fig. 3.12, but rather at 2.426 GHz. The reason for this lies in the coupled nature of the phenomenon itself: if in Fig. 3.12 the phononic mode was left unperturbed, when also the optical pump is turned on both the electrostriction force and the radiation pressure play their role in deforming the geometry of the resonant cavity. This means that the domain in which the phononic mode resonates is slightly modified

3.2 The phononic waveguide

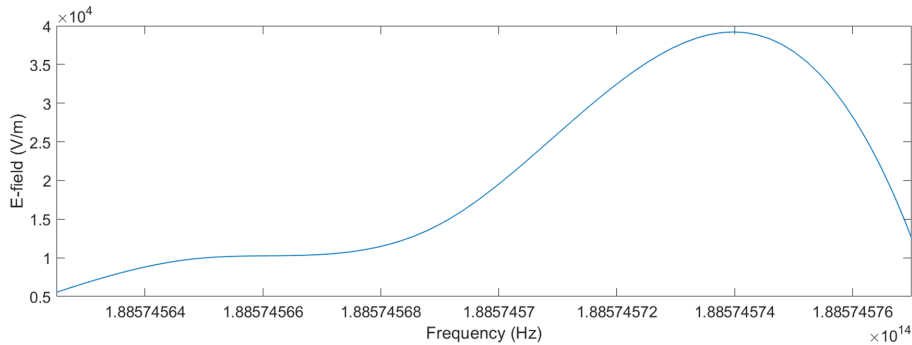


Figure 3.13: Scattered E-field (V/m), generated by the fully-coupled method, vs. frequency (Hz). The resonance peak falls here at 2.426 GHz, which is slightly shifted from the resonating frequency of the mechanical mode observed in Fig. 3.12 of 2.434 GHz. Such difference is due to the optical forces (e.g. electrostriction and radiation pressure) acting on the cavity.

in respect to the case in which there are no optical forces exerted, and this causes a shift of the mechanical resonating frequency.

For the sake of completeness, the distribution of both the phononic (Fig. 3.14a) and EM fields are shown in Fig. 3.14.

3.2 The phononic waveguide

After having extensively talked about the phonon-light interaction that has been induced in a resonating cavity by an external optical source (either by a blended optical fiber or by a slab waveguide in which a Bragg’s mirror has been designed), and also about how such interaction can be treated from a theoretical point of view (either by an approximate, perturbative approach or by a rigorous one, capable of effectively couple the two fields involved), in what follows a brief introduction on the extraction of the phononic signal will be given.

This section, from the perspective of the main action plan, is placed at the second main point, e.g. *to extract the phononic signal from the OM cavity, by developing a proper phononic waveguide in which the wave is able to propagate in the millimeter scale range.*

Although there are a large variety of aspects involved when it comes to structure and optimize a generic wave-like propagation on a solid medium, going from the strictly theoretical point of view of engineering the shape of the mode in propagation, to technologically-oriented issues like fabricating a mostly-suspended Si-device in order to get rid of the mechanical losses related to the bulky-waves, because of severe non-disclosure restrictions related to the still on-going European project this work is developed in, only a rather general overview of the state of art will be given here.

Chapter 3 Concerning coherent phonons detection and generation

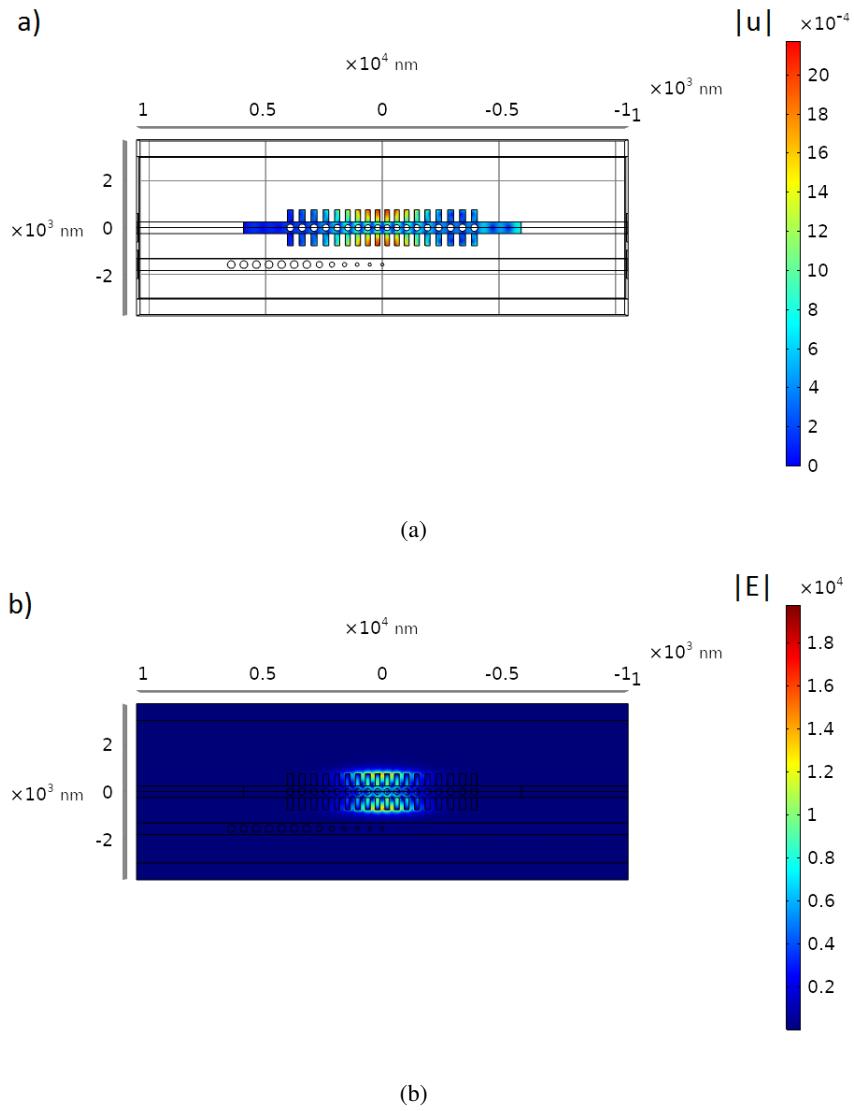


Figure 3.14: Plot of the a) displacement field (nm) and b) scattered electric field (V/m) generated by the fully-coupled method.

3.2 The phononic waveguide

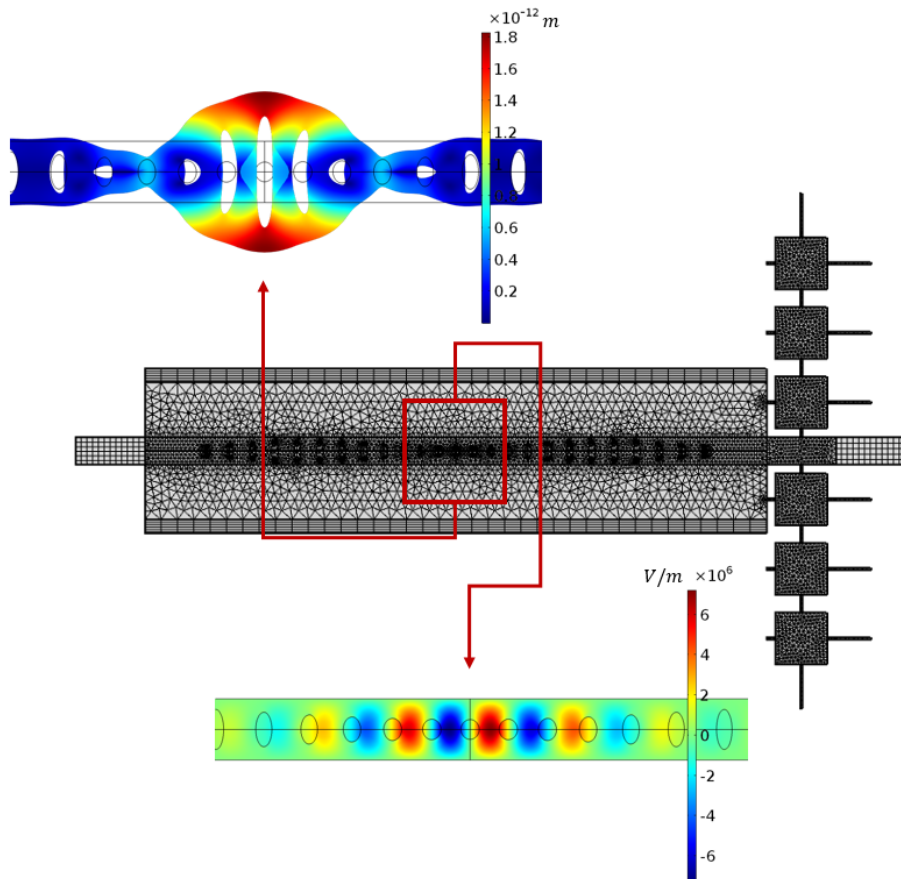


Figure 3.15: Evaluation of both the phononic and optical modes, by mean of the fully-coupled model, for the OM configuration as proposed by [28]. A phononic waveguide composed of a standard slab joined by a phononic shielding is connected, for detection/generation purposes, to one of the two terminals of the OM cavity.

Chapter 3 Concerning coherent phonons detection and generation

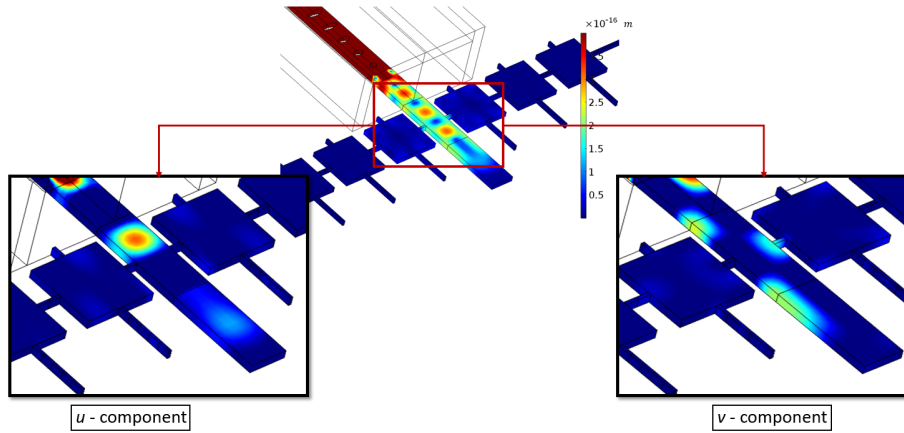


Figure 3.16: Evaluation of both the longitudinal and transverse components of the phononic wave resulting from the OM cavity ([28]) excitation.

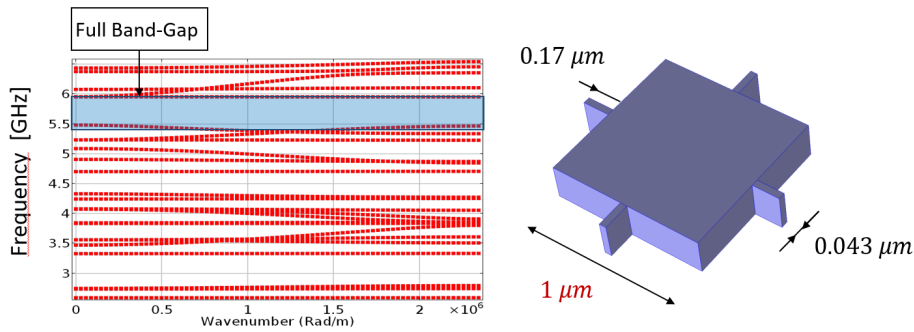


Figure 3.17: Dispersion curves and geometrical parameters of the phononic shield as proposed by [28].

Firstly, the outcomes of [28], where an OM crystal (designed for exhibiting a coupling phenomenon at 5.1 GHz) has been integrated to what has been defined as an acoustic shield, will be regained and extended, and further evaluation on the efficiency of the phonon extraction and on the magnitude of the phononic wave itself will be given.

Secondly, the same acoustic shield design concept will be applied to the OM cavity that has been largely investigated in the previous chapters, and its highest operating frequency will be exploited.

Fig. 3.15 shows the model setup (with a focus on the meshing) and both the optical and mechanical resonating modes computed, rigorously, by mean of the fully-coupled approach. The significantly high quality factors of the modes related to this particular cavity design ($Q_{opt} \sim 1 \cdot 10^6$ and $Q_{phon} \sim 6 \cdot 10^5$, both experimentally observed), although beneficial for the overall coupling process, has several downsides from both

3.2 The phononic waveguide

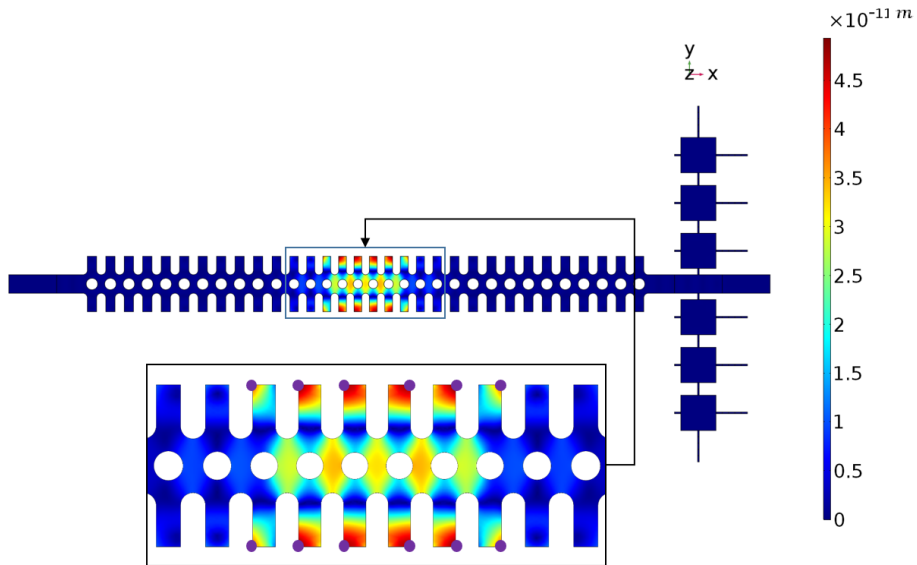


Figure 3.18: Punctual mechanical excitation aimed to evaluate the behavior of the phononic wave coming out of the OM cavity.

theoretical and practical points of view. An high quality factor means high values of the resonating fields in play, so the mesh setting and, primarily, the criticality of the OM coupling represent great challenges for the numerical simulation.

The meshing issue, in principle, may be solved by simply adopting a finer mesh strategy, but such an increase of the element density may lead to an unmanageable model from the computational cost point of view. Additionally, the mesh element population should be denser only in particular region of the cavity, e.g. the ones in which the resonating field reaches its maximum values, and this requires preliminary studies aimed to deeply understand the mode configuration.

A second theoretical issue one must consider is the one related to the well known convergence problems that arise when dealing with particularly strong couplings. The non-linear nature of the equations analyzed in the previous chapter, together with the several *bridges* existing between the two physics in play (e.g. the electrostriction and the radiation pressure forces, the photoelasticity and the moving boundary effect), make the convergence process extremely difficult. As a proof of that, for limiting the magnitudes of the resonating fields, the optical pump excitation has been kept to $20 \mu\text{W}$, which still generates considerably high values of the scattered E-field.

The practical downside of having such an high quality factor is related to the mode confinement itself: while, as aforesaid, having a good mode confinement is preferable in terms of coupling efficiency because of the magnitudes in play, when it comes to carry the signal (the phononic one, in this case) out of the resonating structure, severe limitations must be taken into account. As shown in Fig. 3.17, the magnitude of

Chapter 3 Concerning coherent phonons detection and generation

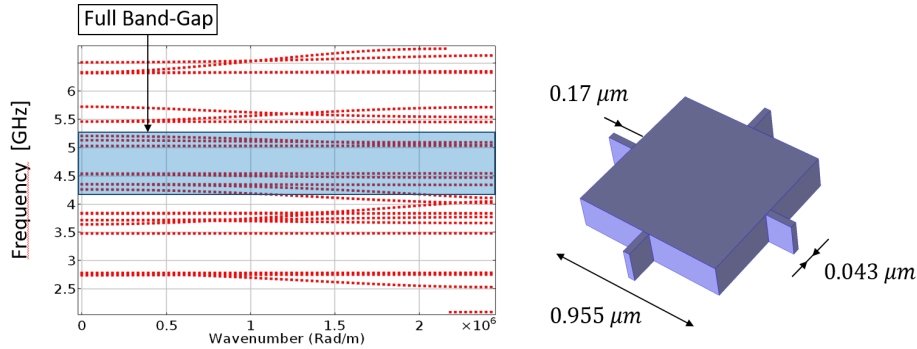


Figure 3.19: Dispersion curves and geometrical parameters of the phononic shield opportunely designed for the frequency in use.

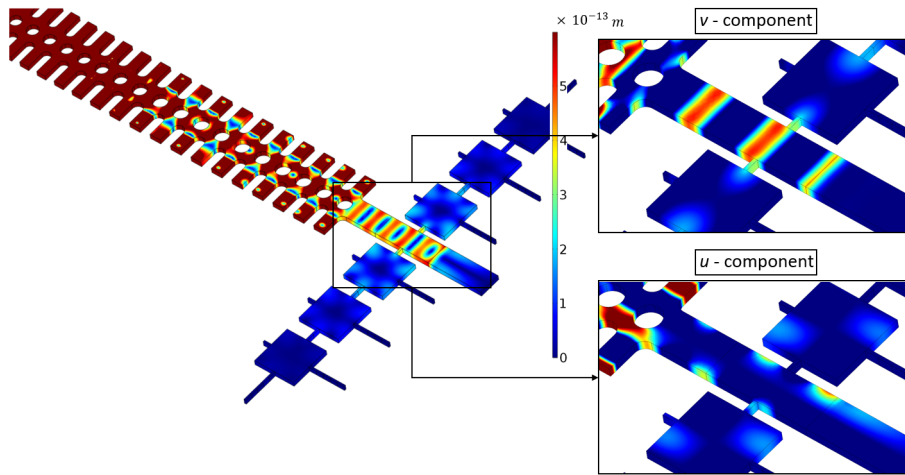


Figure 3.20: Evaluation of both the longitudinal and transverse components of the phononic wave resulting from the OM cavity excitation.

the displacement-wave extracted from the cavity is attenuated, with respect to the one resonating in the inner region of the cavity, by several orders of magnitude ($\sim 4.5 \cdot 10^3$). Although such analysis cannot be declared as a quantitative one since the excitation of $20 \mu\text{W}$ provides down-scaled values of the fields, has been given as a pump signal, the ratio between the magnitudes of the two considered waves is not expected to change in a real-case scenario.

Fig. 3.16 focuses on both the geometrical parameters (taken directly from [28]) and the dispersion curves of the acoustic shielding that has been used for confining the phononic wave. A total band-gap is observed between 5 and 6 GHz, which also defines the working range of the waveguide. In general, it has been observed that three repetitions of the acoustic shielding unit cell are enough for providing an acceptable level of phononic confinement. This means that the complete design for a phononic

3.2 The phononic waveguide

waveguide must consider a slab (having the same size of the OM cavity in which the signal is generated/detected) and three repetitions of the acoustic shield unit cell for each side, which leads to an overall width of the suspended Si-domain of, approximately, $6.5 \mu\text{m}$.

By modulating the side of the shielding unit cell, e.g. by passing from a value of $1 \mu\text{m}$ to a value of $0.955 \mu\text{m}$, one can shift the band-gap to lower frequencies, and so target the maximum working frequency of the cavity design here treated ($\sim 4.7\text{GHz}$), as shown in Fig. 3.19.

The re-designed acoustic shield has then to be integrated with the OM cavity, as shown in Fig. 3.18, allowing for the phonon extraction. In this case, a versatile mechanical-only simulation has been preferred to the fully-coupled approach since the target of the study is the phononic behavior alone, which permits to get rid of useless computational efforts. The phononic mode has in this case been excited by means of a punctual application of harmonic loads (oscillating at the same frequency of the mechanical mode), which has been opportunely tuned in their magnitude to generate the same maximum mode displacement as the one that would be found by performing a rigorous OM simulation.

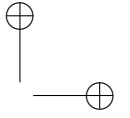
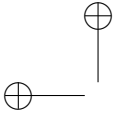
By comparing the maximum of the phononic mode resonating in the inner region of the cavity to the maximum of the extracted displacement-wave of Fig. 3.20, one may notice a considerably lower difference in magnitude in respect to the one related to the previous design [28]. In fact, if before such ratio reached a value of $\sim 4.5 \cdot 10^3$, in this case, because of the lower values of the quality factors in play, the ratio drops down to $\sim 10^2$. Having such an improvement in the generated phononic wave magnitude is extremely beneficial in terms of signal propagation, pushing the design scale of the phononic waveguide up to the millimeter-range. Additionally, by recurring to the definition of the mechanical energy flux, also the mechanical losses due to the non-ideal efficiency of the phononic shielding have been taken into account. The mechanical energy flux is a vector formed by the multiplication of the stress tensor and the velocity vector

$$I_i = -\sigma_{ij}v_j. \quad (3.1)$$

The reason to have the minus sign in the definition is that if to put a pressure on an external boundary for then moving it in the direction of the load, then a positive power input in the direction of the load is obtained. When it comes to perform an analysis in the frequency domain, then we have

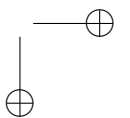
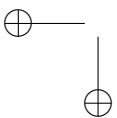
$$I_i = \frac{1}{2} \text{Re}(-\sigma_{ij}v_j^*). \quad (3.2)$$

In the case under investigation, the mechanical energy flux associated to a phononic wave shoot in an ideal suspended slab (where the only mechanical losses are the one related to the non-ideal material the slab is made from) is $6.78 \cdot 10^{-11} \text{W/m}^2$, whereas the one related to the real case, in which the acoustic shielding has been applied, is



Chapter 3 Concerning coherent phonons detection and generation

$6.39 \cdot 10^{-11} \text{ W/m}^2$, confirming the efficiency of the developed phononic waveguide.



Chapter 4

SAWs as a phonon processing alternative

In the last two chapters, various solutions for addressing issues such as i) the generation of coherent phonons at various frequencies and ii) the wave-confinement in efficient waveguides capable of carrying the phononic information for hundreds of μ have been given.

In particular, in chapter 2 the focus has been put on the introduction of a model enabling the rigorous simulation of the OM interaction, and several examples of original resonating phononic cavities have been given.

Chapter 3 unfolded the relevant problematics of optically exciting an OM cavity without recurring to the unstable optical fiber loop, and also studying a convenient way for extracting the phononic information out of the resonating element. It has been proposed, respectively, a design in which a nanobeam (e.g. a slab waveguide optically terminated by a Bragg's mirror) is put close to the OM cavity, and a waveguide completed by an acoustic shielding capable of confining the phononic signal at the targeted frequency.

In what follows, SAW will be used in order to pave the road for the third, final point of the main action plan, e.g. *to process the generated phononic information in order to enable a fully phononic driven circuit.*

In the first part of this chapter, a theoretical study on how to efficiently convert a SAW, generated on a substrate by means of an electric signal, into the acoustic modes of a phononic waveguide/cavity will be presented. Such analysis has the double outcome of i) providing an alternative way of exciting a phononic cavity instead of recurring to an optical fiber and ii) testing the way a SAW launched towards a breathing OM cavity affects the pre-existing phononic population. At first, the possibility of converting a SAW (generated on a Si-based medium that also considers a thin piezoelectric AlN layer) into the guided mechanical modes allowed in a phononic waveguide will be studied, and to this aim an original configuration, enabling the maximization of the mechanical energy transfer, has been developed. Furthermore, the nature of the modes created inside the phononic waveguide by means of the SAW-based excitation will be analyzed. In addition, as mentioned herein-above, the SAW-based approach

Chapter 4 SAWs as a phonon processing alternative

will also be used for exciting an OM cavity, and the related transmission properties, together with the induced-modes analysis, will be discussed.

In the second part of this chapter, the more practical issue of calibrating a SAW-based device is tackled: a rigorous numerical calibration is proposed in order to characterize the excitation of propagating mechanical waves by IDT, where the transition from such integrated transducers terminals to phonon waveguides is modeled, for convenience, by means of a general circuit representation that makes use of the SM formalism. The calibration approach that has been chosen for carrying out such analysis is the well-established TRL, which is proven to be capable of extract/de-embed general acoustic components from the terminals (e.g. the IDT), regardless of complexity and size of the latter. For ensuring the solidity of the numerical approach, the latter has been validated by mean of an independent analytic calculations.

4.1 Conversion between SAW and guided modes of a quasi-periodic structured nanobeam

4.1.1 Electromechanical coupling in the system of IDT on piezoelectric layer deposited on Silicon membrane

A SAW excited by mean of several IDT placed on top of a piezoelectric material (layered on a Si-substrate, as shown in Fig. 4.1) is here used for transmitting/detecting mechanical waves to/from a Si-membrane. For accomplishing the task of evaluating both the transmission and the reflection of the mechanical wave, two sets of IDT are opposing one another, and a Si-membrane is placed in the middle. For alternative investigations, the latter could be opportunely engineered in order to become a proper phononic cavity.

Starting from the top of the structure, the investigated multilayer is composed of i) an array of Al IDT's placed on top of a ii) piezoelectric material (AlN), iii) a Si-membrane that goes all the way through the sample, iv) a SiO₂ layer and v) the Si-substrate.

For avoiding any mechanical reflection coming from the bottom limit of the substrate (which, in the measured device is much thicker than the simulated one), mechanical PML have been inserted. It is worth to mention that all the numerical simulations have been carried out by mean of COMSOL, where both the mechanical and the electrical modules have been used in order to investigate the piezoelectric phenomenon.

As a first step of our analysis, the generation of SAW having high transfer rate from the multilayer structure (e.g. where they have been generated by mean of the IDTs) to the Si-membrane must be achieved. To this aim, the unit cell (meaning that periodic conditions have been applied to the sides of the considered domain) shown in Fig. 4.2a has been considered, whereas Fig. 4.2b shows the related dispersion curves for

4.1 Conversion between SAW and guided modes of a quasi-periodic structured nanobeam

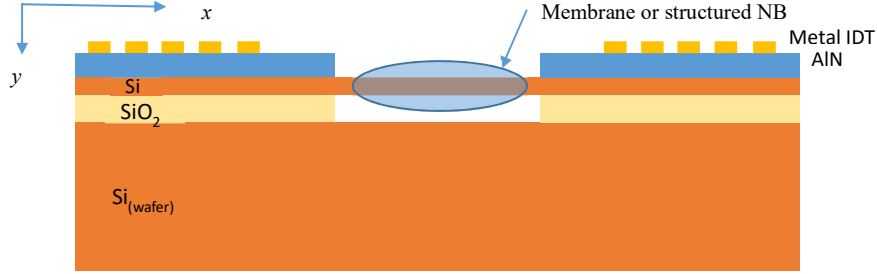


Figure 4.1: Schematic representation of a prototype device for the phonon generation and detection by electrical means using IDT on a piezoelectric AlN film deposited on the Si membrane. The surface acoustic wave generated by the IDT propagates through the Si-membrane (or through the nanobeam, where optomechanical effects can occur) and can be detected by another IDT system [30].

Table 4.1: Elastic constants (GPa) and mass density (kg/m^3) for materials used in the simulation.

	ρ	c_{11}	c_{12}	c_{13}	c_{33}	c_{44}	c_{66}
Si	2330	166	64	-	-	79.6	-
Al	2695	111.84	60.08	-	-	25.88	-
SiO ₂	2200	78.3	15.7	-	-	31.3	-
AlN	3260	345	125	120	389	118	110

few values of the lattice parameters L_{IDT} . The chosen geometrical parameters are:

- $h_{\text{Al}} = 100 \text{ nm}$, $w_{\text{Al}} = L_{\text{IDT}}/4$: thickness and width of Al-electrodes,
- $h_{\text{AlN}} = 0.5 \mu\text{m}$: thickness of the piezoelectric layer,
- $h_{\text{Si}} = 220 \text{ nm}$: Si-membrane thickness,
- $h_{\text{SiO}_2} = 560 \text{ nm}$: thickness of the Si-dioxide
- $h_{\text{Si(wafer)}} = 7 \mu\text{m}$: wafer thickness bounded by a PML layer from bottom,

while the excitation has been kept constant at 1 V. For what concerns the material properties of the considered materials, only the AlN has been considered as anisotropic (Al, Si and SiO₂ have been, instead, considered as cubic materials), and all the used values are reported in Tab. 4.1:

The electric physics also consider the presence of air, that surrounds the investigated SAW-based device and allows the E-field to propagate unperturbed.

In the dispersion curves shown in 4.2b, only the modes which are strongly confined in the piezoelectric region are shown. For evaluating such degree of localization, the

Chapter 4 SAWs as a phonon processing alternative

ratio between the integrals of the square modulus of the displacement field have been calculated: the integral at the numerator has been evaluated on the top region, e.g. in the AlN/Si-membrane domains, while the one at the denominator over the whole domain (including the PML region). In this way, both bulky and artificial PML modes can be canceled from the analysis.

For comparison purposes, also the sound velocity (more specifically, its longitudinal component) of Si and SiO₂ are reported in the dispersion curves of Fig. 4.2b. Given the fact that the investigated configuration is placed on a Si-substrate, the dispersion curves related to the SAW are found below the sound lines belonging to both the transverse and longitudinal waves in Si (the transverse component is not shown in Fig. 4.2b since it overlaps with the SiO₂ longitudinal component). At the Brillouin zone boundaries, we can notice that the dispersion curves are folded into the radiative frequency region.

Fig. 4.2c and Fig. 4.2d show the spatial distribution of the displacement field (e.g. its absolute value) for the case of intersection of two dispersion curves localized at 2 GHz. One can notice that the two identified modes are well confined in the AlN/Si-membrane region of the SAW-based device.

After having optimized the structure so that a well confined acoustic mode can be used at 2 GHz, the transmission/reflection over a semi-infinite Si-membrane can be evaluated. From the physical point of view, the SAW generated by mean of the structure investigated above should now be turned into lamb waves in the Si-membrane. Such Si-membrane is connected to the SAW-generating region *naturally*, e.g. without any geometrical optimization and/or tapering for helping the SAW conversion into the lamb wave: the Si-layer placed under the AlN is kept while all the others (apart from the Si-substrate) are etched away. Additional PML domains are added both on the left and on the right sides for absorbing the incoming mechanical waves. Fig. 4.3a shows the generated displacement at 2 GHz.

As expected (see Fig. 4.3b), the maximum achievable values for the mechanical energy flux evaluated at the right-end of the Si-membrane, falls for a wavevector ~ 0 , meaning that a stationary, resonating mechanical mode is established in the Si-membrane. It has also been observed that the optimized lattice parameter for the unit cell width is $2.21 \mu\text{m}$, whereas for what concerns the optimized thicknesses of the various layers in play: $h_{\text{AlN}} = 580 \text{ nm}$, $h_{\text{SiO}_2} = 560 \text{ nm}$ (assuming the Si slab thickness to be fixed at 220 nm).

Along with the evaluation of the mechanical energy flux, also the SAW-lamb wave conversion efficiency has been considered, and according to what's shown in Fig. 4.3b, the peak value of -21 dB falls at 2 GHz (e.g. the targeted frequency). For computing the conversion efficiency, the ratio between i) the time-averaged Pointing vector integrated over the section of the nanoplate and ii) the apparent electric power consumption calculated as an integral of a product of the normal component of the current density of the anode and the applied voltage over the lines of the IDT anode

4.1 Conversion between SAW and guided modes of a quasi-periodic structured nanobeam

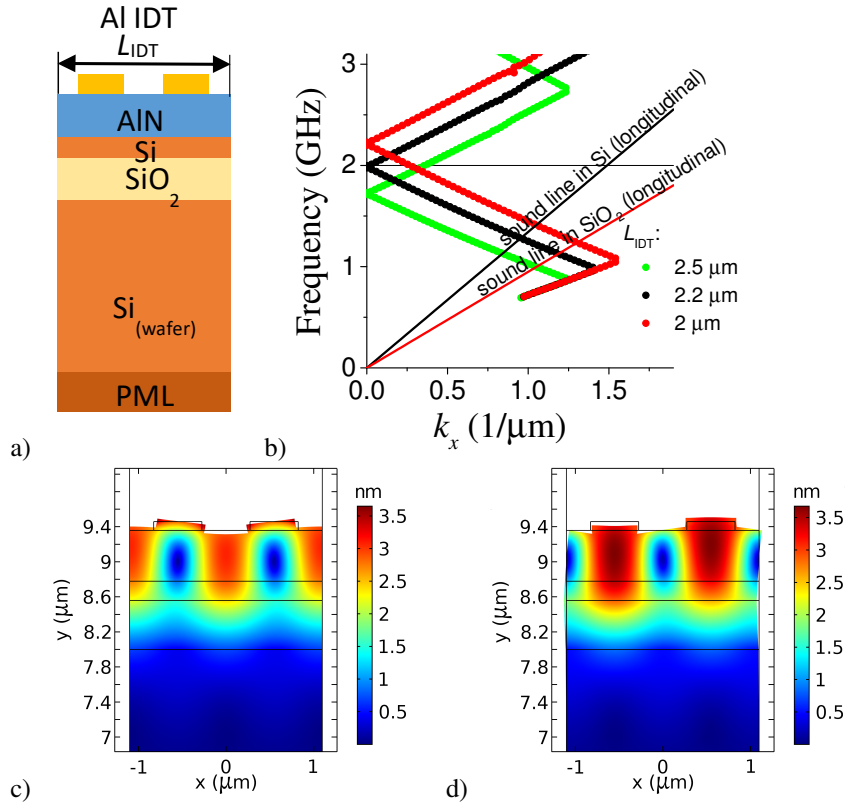


Figure 4.2: (a) Schematic presentation of the unit cell of IDT. (b) Dispersion curves corresponding to the generation of SAW for different lattice lengths: $L_{IDT} = 2; 2.2$ and $2.5 \mu\text{m}$. Other geometrical parameters are $h_{Al} = 100$ nm and $w_{Al} = L_{IDT}/4$; $h_{AlN} = 500$ nm; $h_{Si} = 220 \mu\text{m}$; $h_{SiO_2} = 560$ nm; $h_{Si(wafer)} = 7 \mu\text{m}$ (see text for description of geometrical parameters). (c,d) Spatial distribution of the absolute value of the displacement field (in nm) at 1.977 GHz (c) and 1.997 GHz (d) for a lattice length of $2.2 \mu\text{m}$ [30]

Chapter 4 SAWs as a phonon processing alternative

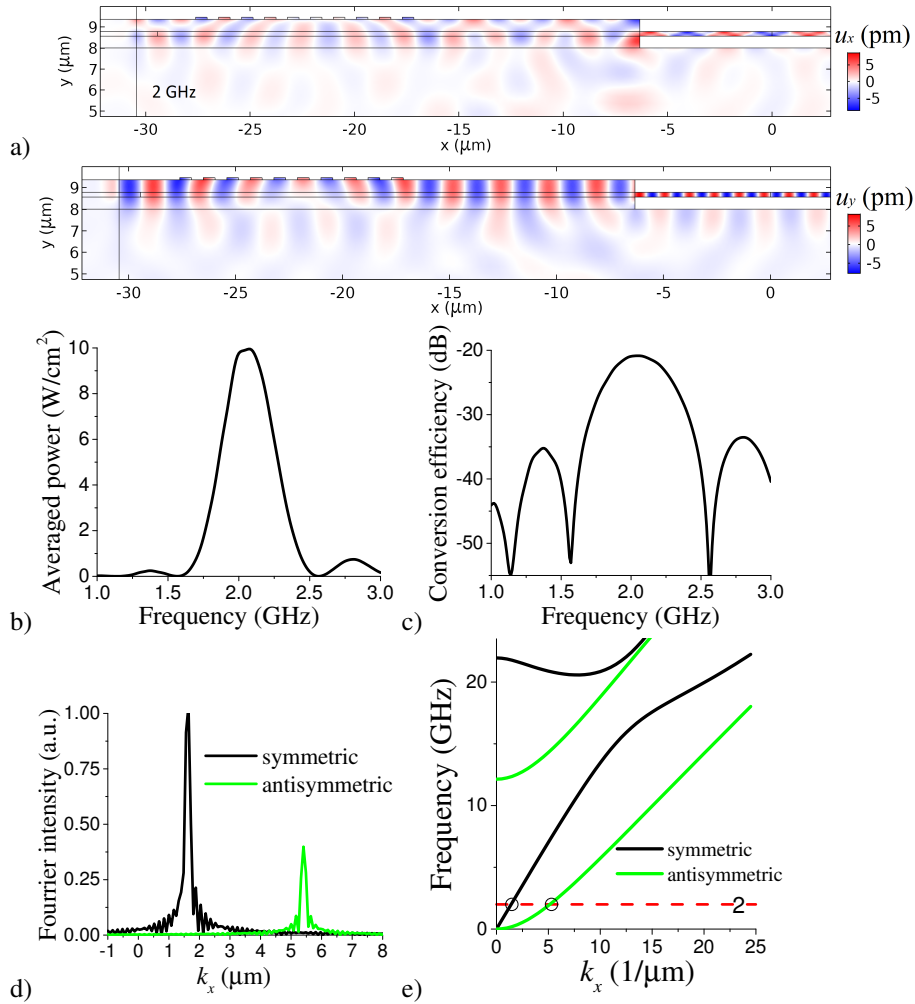


Figure 4.3: (a) Calculated real parts of the components u_x (top) and u_y (bottom) of the displacement field (in pm) at 2 GHz. (b) The power flux averaged over the nano-plate section at the right side (just before the PML). (c) Efficiency of conversion of RF signal into nanoplate modes. (d) Spatial Fourier transform for symmetric and anti-symmetric waves for a linear cross-section through a nanoplate in the direction of propagation at a frequency of 2 GHz. The resulting wave vectors coincide well with those of the Lamb modes of the 220 nm Si nanoplate at 2 GHz, as shown in panel (e) [30].

4.1 Conversion between SAW and guided modes of a quasi-periodic structured nanobeam

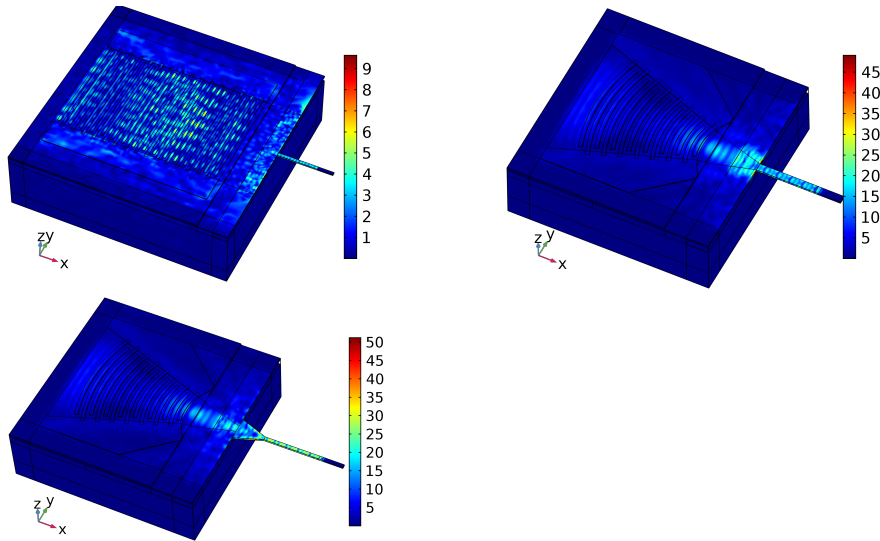


Figure 4.4: The spatial distribution of the absolute value of the displacement field (in pm) for IDT terminated by a slab at 2 GHz. Three different IDT structures (in pm) have been tested. The same scale of the displacement field is used for these cases.

contacts [30].

For a deep understanding of the nature of the waves in play, the Fourier spatial transform of the x-component of the displacement field inside the Si-membrane is evaluated in Fig. 4.3d (for both the symmetric and antisymmetric lamb curves).

Fig. 4.3e shows the dispersion curves of the allowed modes in the 220 nm Si-membrane. If to consider a frequency of 2 GHz, the two peaks of Fig. 4.3d (e.g. $q = 1.6 \mu\text{m}^{-1}$ for symmetric and $q = 5.4 \mu\text{m}^{-1}$ for antisymmetric cases) agree acceptably with the values observed in the dispersion curves of Fig. 4.3e.

4.1.2 Efficiency of the conversion from RF electrical signal into the guided modes of a straight slab

After having investigated both the maximization of the SAW excitation efficiency in an heterogeneous multilayer structure and the conversion of the SAW to a lamb wave confined in a thin Si-membrane, in what follows the possibility of inserting a SAW into a slab will be examined. To this aim, the herein-above studied Si-membrane will be replaced by a straight slab, meaning that the allowed modes changes from the ones related to an infinite thin membrane to the ones of a thin/narrow structure. It is also clear that the geometry of the problem requires a full-3D simulation: as it will be shortly shown, both the SAW-generating structure and the slab present configurations that cannot be described by a 2D environment any longer.

Chapter 4 SAWs as a phonon processing alternative

As a first step, Fig. 4.4 shows the investigated structures for what concerns the excitation of a slab by mean of an IDT array. In particular, the spatial distribution of the absolute value of the displacement field in the transition region is shown. Concerning the IDT, three different configuration have been numerically tested, namely i) standard parallel fingers, ii) radially curved fingers with a straight slab roughly connected to the SAW-generating multilayer and iii) radially curved fingers with a tapered slab (which should allow the SAW to be more efficiently converted to the propagating modes of the slab). In this case, the chosen geometrical parameters are:

- $h_{Al} = 100$ nm and $w_{Al} = 550$ nm (chosen according to fabrication-related impositions)
- $h_{AIN} = 250$ nm (chosen according to fabrication-related impositions)
- $h_{Si} = 220$ nm
- $h_{SiO_2} = 1$ μ m
- $h_{Si(wafer)} = 4$ μ m.

The two configurations of IDT have been designed by considering 31 fingers with an aperture of 20 μ m for what concerns the standard parallel setup, while the radially curved ones has 15 fingers with an aperture angle of 40 degrees, having the center point of the circles as the middle-point of the base of the taper. As for the investigations presented before, the electric excitation of the IDTs has been kept at 1 V, while the considered Si-slab has the same thickness of the Si-membrane (e.g. 200 nm) and a width of 500 nm.

Fig. 4.4 clearly shows that the parallel IDT (e.g. what has been defined as the standard configuration) doesn't provide a sufficiently good SAW-slab modes conversion: due to the wide wavefront of the generated SAW, only a fraction of it commutes to a confined mode of the slab, while the remaining portion is located at the edges of the SAW-generating multilayer. The structures presenting the radially curved fingers provide a much more efficient mechanical energy transfer, and this is due to the SAW-focusing of the region where the slab is connected. Between Fig. 4.4b and Fig. 4.4c, a small improvement of the SAW-slab modes conversion is observed when the additional taper on the slab is considered. In fact, the latter has the ability of adiabatically pulling the right edge of the Si-layer into the slab [30]. The taper is 4 μ m long and its base width (e.g. the one opposite to the slab) is 3.41 μ m.

Fig. 4.5 shows the dispersion curves related to the slab under investigation, so that a deep understanding of the very nature of the SAW-slab modes conversion may be pursued. Considering that the slab doesn't present any discontinuity, a rectangular unit cell of section 500 \times 200 nm has been studied. Four propagative branches, having different phase velocities, can be clearly recognized in the dispersion curves for low

4.1 Conversion between SAW and guided modes of a quasi-periodic structured nanobeam

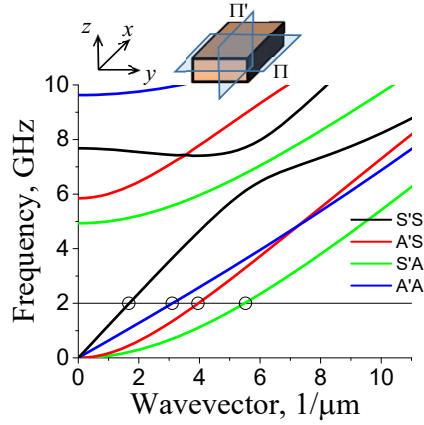


Figure 4.5: Dispersion curves of the silicon slab of rectangular section ($a \times e$) = (500 nm \times 220 nm). The branches are labelled as symmetric (S' and S) or antisymmetric (A' and A) with respect to the two symmetry planes Π' and Π .

Table 4.2: Symmetry of the first four low frequency modes of the rectangular slab. The parity even (e) and odd (o) are defined with respect to the plane Π' and Π respectively (see Fig. 4.5). Spatial distribution of the displacement field for the first four low-frequency modes at a frequency of 2 GHz (only non-zero real and imaginary parts of components are presented) [30]

mode	Π'	Π	Parity (Symmetry)	Spatial dist. of the norm. disp. field		
				$\Re(u_x)$	$\Im(u_y)$	$\Im(u_z)$
1	even	even	ee (S'S)			
2	odd	odd	oo (A'A)			
3	odd	even	oe (A'S)			
4	even	odd	eo (S'A)			

Chapter 4 SAWs as a phonon processing alternative

frequency values, and the relative parity of such modes with respect to the symmetry planes Π and Π' (shown in the inset of Fig. 4.5) can be found in Table 4.2.

The latter lists both the nature of the mode and their mechanical field spatial configuration, considering all its spatial components u_x , u_y , and u_z , coming from the form $\tilde{u}_n(x, y, z, t) = u_n(y, z)e^{-ik_{\text{mode}}x+i\omega t}$, where k_{mode} is the wave vector of the considered mode. No coupling between the modes is possible since they are all orthogonal to each other.

By considering the herein-above discussed field distribution of the four modes, the wave excited in the slab by mean of the SAW can be seen as a linear superposition

$$\mathbf{u} = \sum_{n=1}^N c_n \mathbf{u}_n, \quad (4.1)$$

where \mathbf{u}_n is the mechanical displacement of each mode, c_n is the weighting factor and N the mode number ($N = 4$ for the frequency region under investigation).

According to the orthogonal nature of the modes, the coefficients c_n can be easily found by integrating over the slab section

$$c_n = \frac{\iint_{S_{\text{Slab}}} \mathbf{u}_n^\dagger \mathbf{u} dS}{\iint_{S_{\text{Slab}}} \mathbf{u}_n^\dagger \mathbf{u}_n dS}, \quad (4.2)$$

where " \dagger " refers to the complex conjugate of transposed vector.

Additionally, to analyze the conversion efficiency of the electric energy into mechanical energy of slab modes we use the ratio between the time-averaged Poynting vector integrated over the section of slab and the apparent electric power consumption in the following form

$$\text{CE} = \frac{\iint_{S_{\text{Slab}}} P_{\text{avx}} dS}{\iint_{S_{\text{anode}}} |J_n^* V| dS}, \quad (4.3)$$

where " $*$ " is the complex conjugate, P_{avx} is the time-averaged x -component of the Poynting vector that is normal to the slab section with the area, S_{Slab} , J_n is the normal component of the current density of the anode (or ground), V is the applied voltage (assumed to be 1 Volt), S_{anode} is the surface of the IDT anode contacts [30].

By making use of (4.3), the SAW-slab modes conversion efficiency has been evaluated for each of the four targeted modes and plotted in Fig. 4.6. Such evaluation is calculated for the time-averaged x -component of the Poynting vector in the T-section of slab (see Fig. 4.6a) taking into account the decomposition coefficients (4.2) of the displacement field $[\]$. A maximum of -22.6 dB is achieved for the mechanical energy conversion by considering a frequency of 2 GHz. It is also worth to mention that, due to symmetry reasons, in the investigated system only modes with in-plane symmetry

4.1 Conversion between SAW and guided modes of a quasi-periodic structured nanobeam

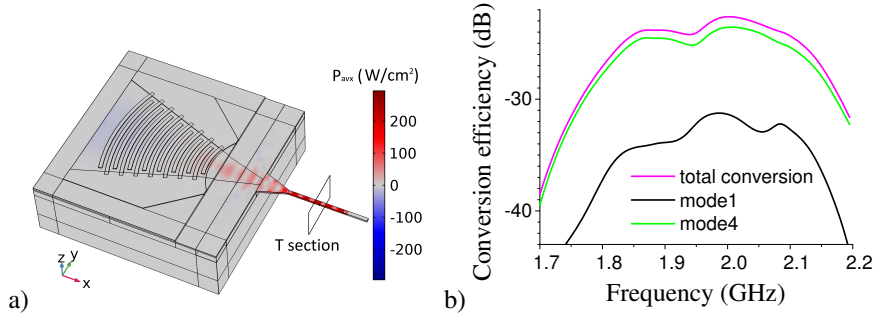


Figure 4.6: (a) Spatial distribution of the x -component of the Poynting vector at 2 GHz. (b) Efficiency of the conversion from the electric signal into mechanical modes of a straight slab [30].

can be effectively excited.

4.1.3 Excitation of cavity modes in a phononic cavity

By extending the work done in the previous sections, in what follows the investigated slab, placed after the SAW-generating structure, will be replaced by the phononic cavity introduced in the previous chapter. The aim of this work is to evaluate the outcomes, in terms of the entity of the resonating modes inside the cavity, of exciting the latter by mean of a SAW. As stated before, the tuned geometrical parameters of the phononic cavity (e.g. the hole diameters and the stubs width) ensure an high Q-factor for both the optical and the mechanical modes, and an efficient OM coupling for GHz phonons has also been proven.

Fig. 4.7a shows the band diagram of the unit cell of the outer regions of the phononic cavity: the following analysis will be limited to the two modes which are symmetrical (referred to as S') with respect to the xOz -plane (Π' plane in Fig. 4.5). These two types of modes are respectively symmetrical and anti-symmetrical with respect to the Π plane in Fig. 4.5 and for this reason we refer to them as $S'S$ and $S'A$. One can observe in Fig. 4.7a the existence of a full band gap in the range of 1.8-2.0 GHz for these two types of modes, since there is a band gap of 1.8-2.2 GHz for the $S'S$ mode and a band gap of 1.6-2 GHz for the $S'A$ mode [30].

The conversion efficiency between the electric energy given to the IDT terminals and the mechanical modes effectively excited in the phononic cavity has been presented for each of the two modes in Fig. 4.7b. For the sake of completeness, also the conversion efficiency related to the previously investigated straight slab (dashed line) and the total conversion of the two modes together are shown. The simulation was carried out in two steps. The first step includes the generation of SAW until their insertion into the straight slab as explained in Fig. 4.5. The second step considers the scattering of the modes generated in the straight slab and discussed in the previous

Chapter 4 SAWs as a phonon processing alternative

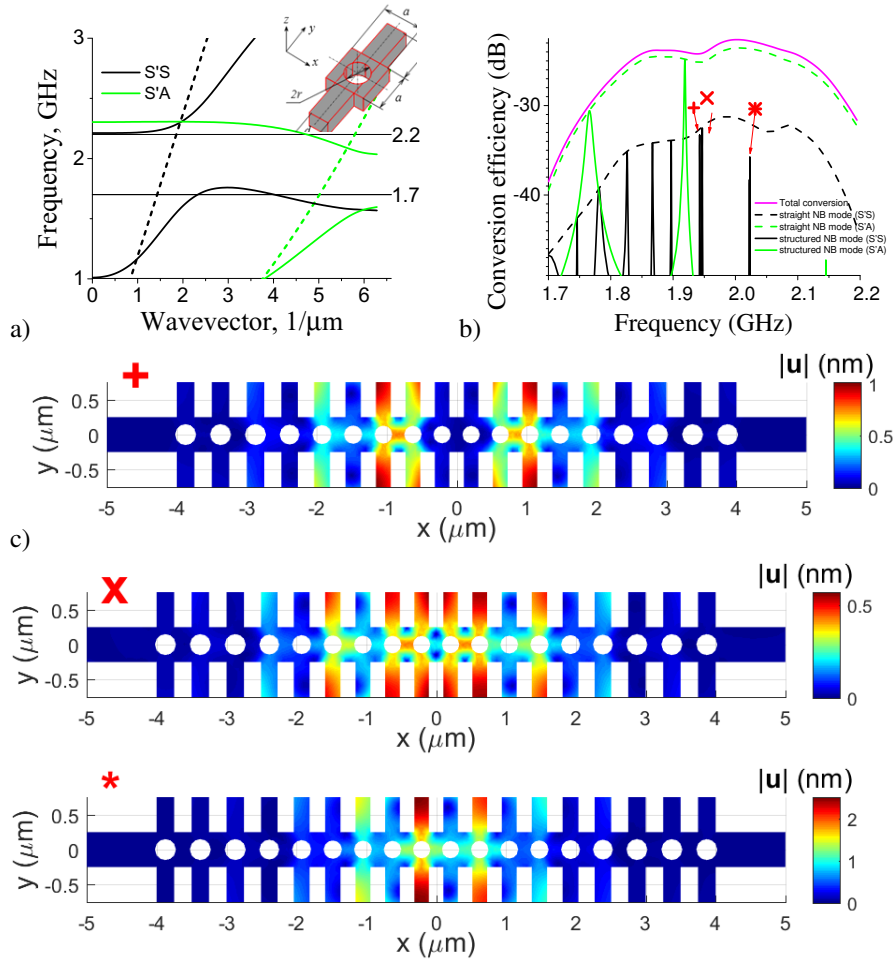


Figure 4.7: (a) Band diagram for periodically structured NB with the unit cell represented in the inset. Parameters of the structured NB: $a = 500$ nm is the lattice parameter of a quasi-periodic structuration of NB, $e = 0.44a$ is the thickness of the NB, $r = 0.3a$ is the radius of the holes, and $d = 0.5a$ and $l = a$ are the width and the length of one rectangular stub, respectively. (b) Spectrum of the SAW conversion efficiency for each NB modes and the SAW conversion into all NB modes with S' symmetry. (c) Displacement field distribution (in arbitrary units) for three $S'S$ cavity modes at frequencies of 1.943 GHz ("+"), 1.947 GHz ("x") and 2.023 GHz ("*") [30].

4.2 TRL Calibration of SAW-based devices

section with the structured 1D phononic crystal and its cavity. In Fig. 4.7b, we can observe the formation of the band gap for the slab modes with the xOz -plane symmetry with extremely sharp peaks corresponding to the cavity modes of the structured slab inside the bandgap. The spatial distributions of the absolute value of the dimensionless displacement fields are presented in Fig. 4.7c for three S/S cavity modes near 2 GHz [30].

4.2 TRL Calibration of SAW-based devices

4.2.1 Preliminary considerations about SAW calibration

In what follows, a new calibration approach, for the emulation of experimental conditions related to SAWs propagating in mechanical circuits that are not directly accessible will be presented. In this framework, the transition from electromagnetic source to mechanical waves, propagating in periodic crystal structures, is rigorously simulated by means of a general circuit representation, that makes use of the SM formalism. Forward and backward waves are defined at the transmitting and receiving IDTs of a SAW-based device (see Fig. 4.8).

Our de-embedding of acoustic components of SAW-based devices can include not only passive and linear elements like filters, phononic crystals/metamaterials, but also non-linear and active devices such as OM cavities, and could be extended, in principle, to multimodal (mechanical) elements, and to non-reciprocal devices (phonon amplification). The computational domain is restricted to the minimum required by rigorous multiphysics simulation, i.e. it is large enough to include the metal fingers of the IDT. In order to further reduce space, Perfectly Matched Layer (PML) are used where appropriate. From the side of the numerical simulation, the present contribution provides a procedure for the characterization of mechanical circuits excited by IDT. The de-embedding procedure also reduces the need of direct mechanical excitation. The latter usually implies preliminary *eigenmode* or *boundary mode* analysis in order to correctly define mechanical input and output *ports*, in general multimodal, and to implement port transparency, which means no back reflection. A rigorous analysis requires numerical description of mechanical displacement and stress at port sections, even in fully anisotropic materials, to define forward and backward waves, and to ensure their ortho-normality, in the sense of the mechanical power. This task becomes even more demanding in case of periodic mechanical waveguides, when super-modes are to be calculated by unit cell analysis. On the contrary, a de-embedding procedure makes possible to define only electromagnetic ports, notably the IDT terminals, typically easy to handle, and commonly available or pre-implemented in multiphysics tools. Our method does not exclude the use of unit cell analysis, circuit parametrization, couple mode theory, or perturbative techniques, but could be integrated with them in a modular approach where single simulation blocks can be cascaded or prop-

Chapter 4 SAWs as a phonon processing alternative

erly combined.

Some typical situations, e.g. transition from periodic to uniform waveguide, and transition from IDT to periodic waveguide (including abrupt substrate discontinuity), are investigated and characterized by TRL calibration, without limiting the generality of the study. Interestingly, frequency dependence of the scattering parameters, mechanical losses, directionality of the discontinuity, have been commented and discussed. This approach provides alternative point of view and way of thinking about mechanical-electrical systems, with potential fallout in the experimental domain, where calibration and de-embedding are usually key steps. Concerning the simulation of evanescent/higher order modes, with the reference is to SAW diffraction problems where wave profiles can be decomposed into their angular spectra, the proposed approach is automatically including modes on any diffraction order, in correspondence of the IDT terminals and of all the discontinuities (transition to the periodic membrane, edge boundaries, etc.). Indeed, evanescent reflected modes, as well as stray mechanical modes or substrate modes, are absorbed by virtual transparent ports, which are made, in our case, by PML, properly set in terms of mesh and thickness. From the electromagnetic point of view, the IDT terminals, being very small as compared to the wavelength, are clearly supporting only their TEM mode.

The reason why circuit representations are so attractive is twofold: on one hand, for the fact that the physics of mechanical waves can strongly benefit from a well-established and mature technique, as circuit theory clearly is, and from tools/models already developed for Maxwell’s equations and e.m. fields in frequency regime. On the other hand, for the possibility to make use of a unified formalism able to describe simultaneously, in a hybrid formulation, both electrical and mechanical physics.

A variety of concepts involved in circuit representations can be applied to SAWs, such as calibration, de-embedding of 2-port and n-port RF circuits, algebraic invariants, etc. We believe that our effort to take advantage of the high potential of the above techniques is the added value of the present report. For instance, up to our knowledge, SM representation combined with TRL calibration has never been reported so far in the literature. Standard methods for IDT analysis, like equivalent circuit models and P matrix models, start from proper parametrization of the equivalent circuit of IDT fingers. Analogously, the Coupled Mode Theory, which is a powerful approach largely used to model optical and microwave devices, needs the knowledge of coupling parameters, which include all the underlying physics and propagation/reflection effects. All models need appropriate parametrization and it is generally difficult to include all physical effects with sufficient accuracy.

Moreover, the above methods are certainly useful but could be not easily applied - or at least they get more complicated after proper generalization - for fine description of general or arbitrarily shaped IDT geometries, abrupt discontinuities and boundary finite terminations, real electrode shape, surface roughness (random deformation of the surface mesh), multilayer complex structures, multimodal conditions with many

4.2 TRL Calibration of SAW-based devices

propagating/attenuating surface waves, rigorous diffraction analysis of the coupling to substrate modes (and related acoustic *radiation pattern* towards the substrate).

Nonetheless, the above issues can be rigorously addressed by means of numerical simulators. Multiphysic FEM are capable of including all above effects, with the possible cost of meshing and computer time and memory. However, it should be remarked that presently available full-wave FEM simulators can provide accurate results even in case of complex computational domains, as they usually feature highly effective sub-gridding, iterative/adaptive mesh refinement, smart domain decomposition, and iterative numerical solving tools. In the end, relatively low computational load and memory occupation are typically required. In addition, as we point out in the manuscript, TRL is intrinsically robust against systematic and repeatable numerical errors, as a consequence of the fact that calibration involves simulations which differ from each other only in a limited region (in our case, part of the suspended membrane), and the IDT and its underlying regions are not changed when passing from one calibration step to another.

Fig. 4.8 shows that a global (2×2) S-matrix includes the effects of three cascaded blocks (Fig. 4.8a): the left transition IDT-to-mechanical waveguide, an internal SAW component, e.g. an acoustic resonator, and the right transition from mechanical waveguide-to-IDT. The first and third blocks can be characterized by using a number $n+1$ of ports: one external port is the electric terminal, the other n internal ports model mechanical excited waves, and depend on the size of their waveguide. Another set of ports can be virtually associated to the mechanical modes radiated into the substrate and surrounding regions (Fig. 4.8b), but they just are terminated to their matched loads, and accounted in the simulation by PML.

4.2.2 TRL Theory

The TRL procedure is a well-established and well known technique for experimental calibration of 2-port microwave devices. The approach can be extended to multi-port circuits, characterized by many physical ports and/or by ports with many accessible modes. The aim of the standard TRL calibration is to extract information, namely the scattering matrix S over the frequency band of interest, about a Device Under Test (DUT), which is not directly accessible by the available measurement tool, typically a Virtual Network Analyzer (VNA). In fact, a linear error box is usually interposed between the VNA and the DUT, due to the presence of connectors, adapters etc. The S-matrix of this linear error box must be removed, as it causes undesired distortion of the DUT response. In the context of the present work, we refer to the error box as *embedding* circuit, and to the DUT as *embedded* circuit. In particular, looking at Fig. 4.8b, the embedding is clearly given by the transition from the electrical terminal to the suspended membrane, and the embedded circuit is given by a possible patterned mechanical circuit. The latter may consist of resonators, filters, metamateri-

Chapter 4 SAWs as a phonon processing alternative

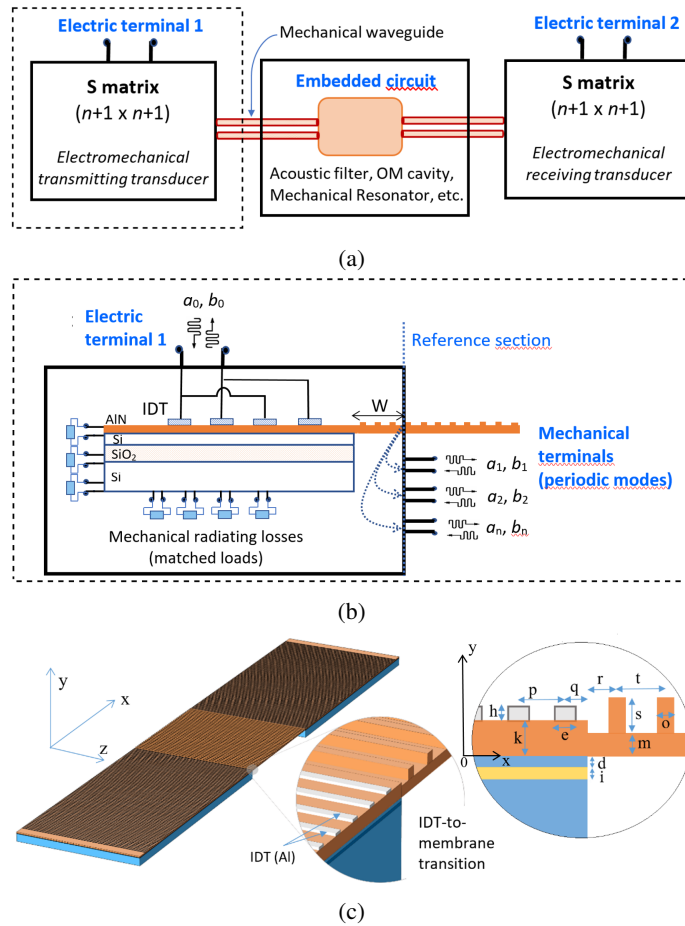


Figure 4.8: (a) Two port circuit, with two electromagnetic ports, plus n mechanical internal ports, (b) detail of the transition from IDT to periodic mechanical waveguide and (c) simulated and structure, with transitions from IDT fingers to periodically patterned mechanical waveguide (central suspended membrane); geometric parameters: $h= 0.2 \mu\text{m}$; $k= 1 \mu\text{m}$; $p= 2.35 \mu\text{m}$; $q=p/2$; $W= 16p$; $e= 0.65 \mu\text{m}$; $t= 2.65 \mu\text{m}$; $r=t/2$; $s= 0.75 \mu\text{m}$; $d= 0.22 \mu\text{m}$; $i= 0.24 \mu\text{m}$; $m= 0.77 \mu\text{m}$; $o= 0.72 \mu\text{m}$ [31]

4.2 TRL Calibration of SAW-based devices

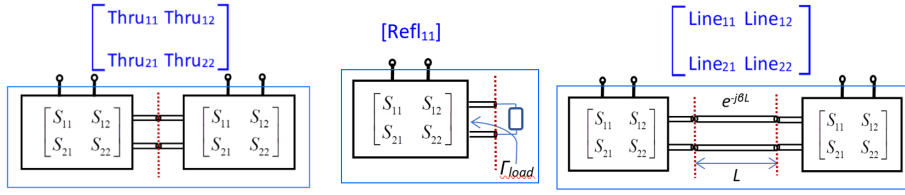


Figure 4.9: Schematic design of the Thru, Reflection, and Line simulations [31].

als, phononic crystals, OM cavities (in this case, active elements also), and mechanical sensors. Filtering out the embedding circuit means removing the effect of whole IDT structure together with its piezoelectric action, as well as the complicated effects of parasitic mechanical waves, mechanical radiation losses, and absorption by the substrate, by the underline layers, and by any region physically connected to the IDT. Thus, the TRL calibration provides a direct way to de-embed an acoustic/mechanical circuit (DUT) by making use only of electrical measurements from the input/output IDT terminals. There is no need to access the internal mechanical waveguide connecting the DUT, or to know other parameters than the geometry and size of the simulated structure. Clearly, this could be of great help in the design and synthesis of acoustic devices, and/or in the physical characterization of the material forming the mechanical waveguide.

In detail, the TRL calibration consists of three independent measurements (here simulations), under known (but different) conditions, namely *Thru*, *Reflection*, and *Line*, as shown in Fig. 4.9. The embedding circuit is assumed to be reciprocal, which implies that $S_{21} = S_{12}$. The final goal is to find the following five circuit parameters: the scattering coefficients of the embedding circuit (S_{11} , S_{12} , S_{22}), the propagation constant of the mechanical transmission line (β) of the *Line* simulation, and the mechanical reflection from the unknown load (Γ -load) in the *Reflect* simulation. The following assumptions are made: i) mono-modal mechanical waveguide, ii) knowledge of all geometrical parameters, in particular the transmission line length L in the *Line* simulation, and iii) perfect symmetry of the whole computational domain, which is guaranteed by proper *mirroring* of the computational mesh. Basing on these assumptions, TRL simulations provide the five equations needed to solve for the five unknown complex parameters in terms of known ones (Thru_{11} , Thru_{12} , Ref_{11} , Line_{11} ,

Chapter 4 SAWs as a phonon processing alternative

Line₁₂):

$$Thru_{11} = S_{11} + \frac{S_{22}S_{12}^2}{1 - S_{22}^2} = Thru_{22}, \quad (4.4)$$

$$Thru_{12} = S_{11} + \frac{S_{12}^2}{1 - S_{22}^2} = Thru_{21}, \quad (4.5)$$

$$Ref_{12} = S_{11} + \frac{S_{12}^2\Gamma_{Load}}{1 - S_{22}^2\Gamma_{Load}} = Ref_{21}, \quad (4.6)$$

$$Line_{11} = S_{11} + \frac{S_{22}S_{12}^2e^{-2\beta L}}{1 - S_{22}^2e^{-2\beta L}} = Line_{22}, \quad (4.7)$$

$$Thru_{12} = S_{11} + \frac{S_{12}^2e^{-2\beta L}}{1 - S_{22}^2e^{-2\beta L}} = Thru_{21}. \quad (4.8)$$

Of course, if one, or more, among the five targeted parameters, is actually known in advance, the above system of equations can be simplified accordingly. For instance, if the propagation constant β is known Eq. (3) can be solved separately from the others. In close analogy with the electromagnetic theory of periodic structures, the propagation constant β of the mechanical transmission line is simply provided by the usual Floquet periodic condition for the unit cell.

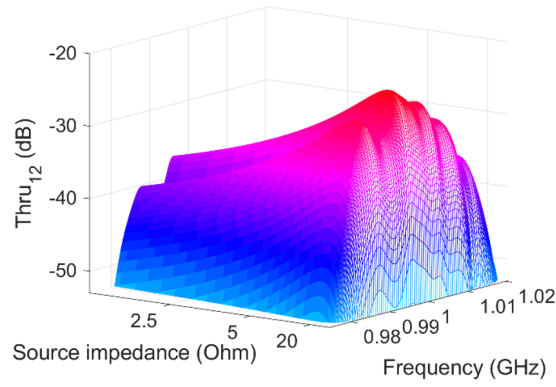
In the present work, we considered periodically patterned suspended membrane as mechanical waveguide, namely the waveguide considered in Fig. 4.8c. This may seem to complicate the analysis, but it actually makes the calibration possible in the form of equations (7-9), since the periodic waveguide is designed to support only one propagating mode. Otherwise, with two or more propagating modes, an extended calibration procedure is needed, to combine more than three independent simulations, in order to find an increased number of unknown parameters. The assumption of a periodic structure also allows to better fit practical situations where the mechanical waveguides are constituted by phononic crystals/metamaterials and nano/micro patterned beams or layers.

4.2.3 Numerical test of SAW calibration by TRL

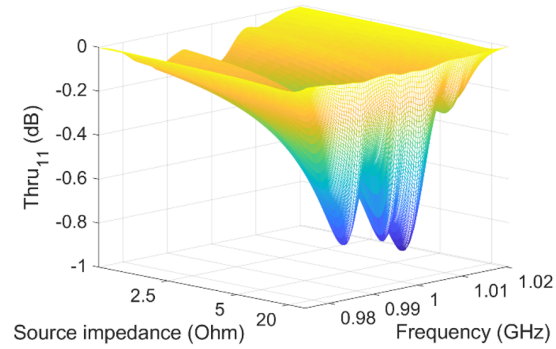
In the following simulations, a length L (see Fig. 4.9), equal to about the length of the unit cell of the periodic membrane, is assumed for calibration: by this choice, the corresponding induced phase delay of the mechanical mode is about a quarter of its wavelength, which is the best numerical condition for calibration purpose.

In Fig. 4.10, the resulting scattering parameters of the *Thru* simulation are plotted as a function of frequency and source impedance. The source impedance, which is assumed to be the same at the two electric terminals, is set to 17.5Ω to minimize the back electromagnetic reflection at the IDT terminals. Accordingly, this choice provides a maximum for the transmittance $Thru_{12}$ (Fig. 4.10a), which means having the highest coupling between the two IDT terminals in terms of electrical power. Apply-

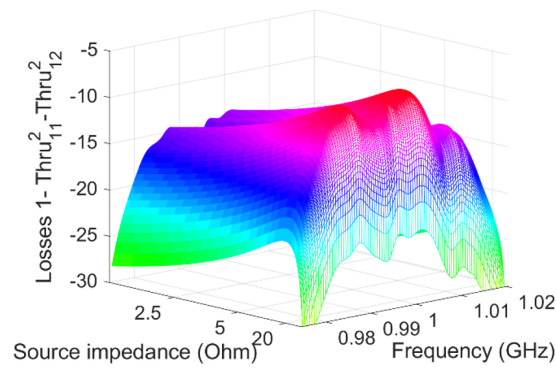
4.2 TRL Calibration of SAW-based devices



(a)



(b)



(c)

Figure 4.10: (a) Simulated Thru_{11} ($= \text{Thru}_{22}$); (b) simulated Thru_{12} ($= \text{Thru}_{21}$), and (c) power lost in *Thru* configuration, as a function of the frequency and of the source impedance [31].

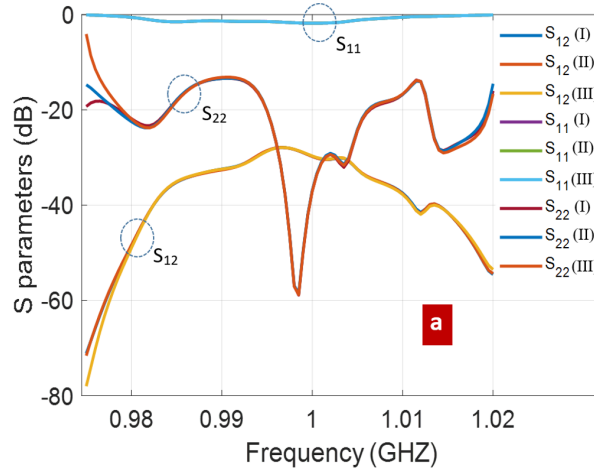
Chapter 4 SAWs as a phonon processing alternative

ing equations (7) and (9), and considering that β is known from parallel analysis, not reported here for the sake of readability, we obtain the scattering parameters S_{11} , S_{12} ($=S_{21}$ by reciprocity) and S_{22} , of the IDT-to-waveguide transition (Fig. 4.10b, with $n=1$): subscripts 1 and 2 refer to electrical and mechanical ports respectively.

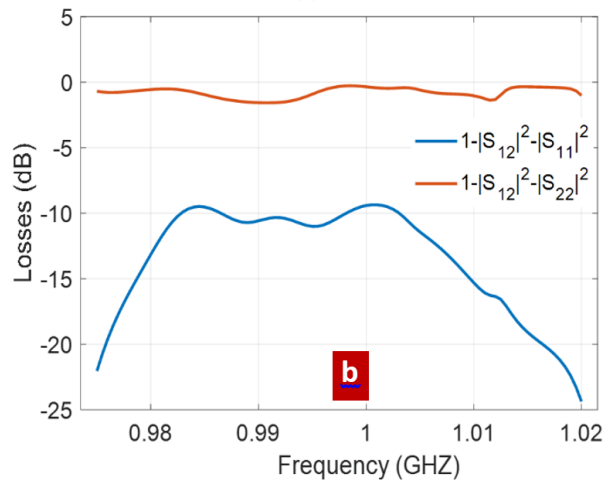
Final results are shown in Fig. 4.11 cases (I), (II), and (III) in the legend refer to different conditions for the calibration procedure: in (I) and (II) $L= 2.65 \mu\text{m}$ and $L= 5.3 \mu\text{m}$ respectively, with reference section (see Fig. 4.8b) for the mechanical port at $W= 16$ unit cells; in (III) $L= 2.65 \mu\text{m}$, but the mechanical section is at $W= 17$ unit cells. These repeated (I, II, III) simulations served to check the numerical consistency of the calibration approach. Some numerical discrepancies among them start to appear at the edges of the considered frequency band, due to the almost complete reflection S_{11} (~ 0 dB), and to the almost vanishing transmission S_{12} (< -40 dB), which make the calibration potentially inaccurate. Such low transmission follows from the frequency bandgaps of the periodic membrane, that appear as moving away from the central frequency of 1 GHz.

The power lost in the IDT-to-waveguide transition is reported in Fig. 4.11b. Interestingly, losses are much higher when the transition is excited from the mechanical port (red curve): in this case, the back scattering is small (S_{22}), and the mechanical power is mostly lost due to transmission to substrate waves. In comparison, the high reflection experienced by the electromagnetic signal at port 1 (S_{11}) implies low transmission, but also low losses (blue curve). In close analogy with experimental TRL calibration, which is intrinsically robust against systematic errors, namely repeatable errors due to imperfections/connectors/etc., also the numerical emulation of TRL is not too much impacted by systematic numerical errors, as apparent from Fig. 4.11b. This is an important consequence of the fact that calibration involves simulations (Thru, Reflection, and Line) which differ from each other only in the limited region of the suspended membrane: in particular, the IDT and its underlying regions are not changed when passing from one calibration step to another. Regarding the mechanical waveguide under test, namely the suspended periodically patterned membrane, its mode spectrum is known by dispersion analysis: all higher modes, which are evanescent in the present study, are properly and rigorously calculated in the simulation. It is noted that, if the evanescent modes were not properly accounted, the calibration procedure would not provide consistent results, especially when the length of the *Line* test (L) and the reference section for TRL calibration (W) are purposely changed - providing that the latter is placed at a proper distance away from discontinuities. The repeated (I, II, III) simulations served to check the numerical consistency of the calibration approach, also in terms of evanescent mode contribution.

4.2 TRL Calibration of SAW-based devices

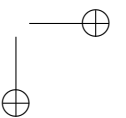
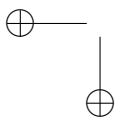
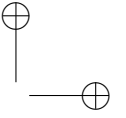
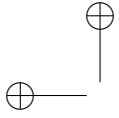


(a)



(b)

Figure 4.11: (a) Calibrated parameters of the embedding IDT-to-waveguide transition: S_{11} , S_{22} , S_{12} ($= S_{21}$); (I) $W= 16$ unit cells and $L= 1$ unit cell, (II) $W= 16$ unit cells and $L= 2$ unit cells, (III) $W= 17$ unit cells and $L= 1$ unit cell; (b) net power lost in case of excitation from the mechanical waveguide (red), and from the IDT (blue): losses are due to radiation of mechanical waves into the substrate [31].



Chapter 5

Conclusions

In this thesis, an extensive analysis of the theoretical approaches aimed to investigate the intersection of photonics, RF signal processing and phononics has been presented. The concept is based on cavity OM to develop GHz-frequency on-chip phononic circuit for room temperature operation. The work that has been discussed here is framed within the (still on-going) EU FET-Open project PHENOMEN.

The main action plan concerning the theoretical description and design of OM-based systems, can be summarized in three points, that have been addressed in the previous chapters:

- *to investigate the efficiency of the OM coupling taking place in a Si-based resonant cavity by mean of advanced numerical methods.*
- *to extract the phononic signal from the OM cavity, by developing a proper phononic waveguide in which the wave is able to propagate in the millimeter scale range.*
- *to process the generated phononic information in order to enable a fully phononic driven circuit.*

5.1 Numerical methods for the rigorous prediction of an OM based system

In chapter II, a fully-coupled numerical approach which accurately predicts the optomechanical dynamics in micro-structured resonant cavities has been presented. The results coming from the method have been tested with respect to the experimental ones from the literature, and a good agreement between the two has been showed. Our method considerably differs from the standard perturbative analysis [25] by giving the effective final displacement of the mechanical resonating mode under investigation caused by the optical excitation and, also, the possibility to evaluate the various optomechanical interaction forces as the electrostriction and the radiation pressure. A further addition concerns the possibility of conducting a multi-modal analysis and taking into account for the material losses, both in mechanical and optical terms, which is

Chapter 5 Conclusions

of key importance in order to correctly characterize the optomechanical phenomenon [27].

Although the accuracy of Transformation Optics (TO) has been already proven elsewhere by means of relevant examples [16], the novelty factor of this work is represented by porting the Stimulated Brillouin Scattering (SBS) analysis from a propagative-like environment like that of a waveguide to a resonant one like that of an high-Q OM cavity [27, 13]. Typically, the SBS is due to the interaction of travelling waves, like in waveguides, or in structures where waves can freely propagate, such as azimuthally traveling waves in micro-disks [41]. In the present study, optical/mechanical modes are localized, but still travelling, as confirmed by the dispersion curves - not reported for compactness - of the photonic/phononic crystal forming the OM cavity. Thus, the above modes can lead to SBS effect, by travelling back and forth in the cavity after multiple reflections (like in simple Fabry-Pérot) [23]. The underlying physicals is not different from micro-disk or related structures, and the mathematical treatment can be unified thanks to TO [13].

In general, the present approach is thought to include the effect of i) moving boundaries ii) multimodal optical/mechanical propagation, and iii) spatial transients. However, extremely high quality factors may pose numerical issues due to the fact that the intrinsic nonlinear character of the problem may be strongly emphasized. Such numerical limits are the object of current work and simulations [13].

Opto-mechanical (OM) coupling in micro- and nano-cavities could help in developing a new generation of microwave photonic devices with extremely small foot-print, sub-mW power consumption and tunable frequency. Here, full-wave modeling of coupled OM cavities has been addressed by extended TO, in order to include the effects of strong mechanical and EM resonances, that enhance non-linearity and make the analysis numerically challenging. In the future, this kind of analysis could also help to explore the quantum world in a convenient way: in particular, OM cavities, at a sub-micron scale, may be used to test the ultimate limits of quantum physics when the entanglement of EM radiation and mechanical waves takes place [13].

In addition, the numerical model that accurately predicts the opto-mechanical dynamics in micro- and nano-structured resonant cavities has been embedded in a COMSOLTM-based application [29]. Such application aims to serve as a user-friendly tool for any researcher/student (without a strong background on computational physics) willing to investigate the OM phenomenon in a generic resonant cavity.

5.2 Design and optimization of phonon generators and phonon waveguides

In chapter III, the focus of the analysis has been shifted from the evaluation of the OM coupling strength that takes place in the resonating cavity to two of the main

5.3 SAW as a phonon processing alternative

issues related to the design of a coherent phonon source, namely i) a proper solution for the optical excitation of the cavity and ii) the most efficient way for extracting the generated coherent phonons.

In order to overcome the current limitations imposed by the fiber-loop based optical excitation of a general optical cavity, mainly related to the difficulties in integrating such a solution with an on-chip environment, a Si-slab has been placed alongside the cavity, aiming to achieve an high EM energy transfer by keeping the approach of the evanescent E-field tail coupling. The design process has been particularly problematic for mainly two reasons. Firstly, the high-values of the E-field generated by the high-Q factor of the targeted cavity requires a considerably fine mesh, and the resulting increased computational effort affects a lot the overall optimization process. Additionally, the mesh must also be carefully designed in order to maintain, in those regions where the gradient of the E-field is particularly high, the same number of mesh elements when evaluating two different configurations. Secondly, the system under investigation requires four numeric ports to be set, and this simple facts creates numerous geometrical issues since such ports tend to overlap. Once the optimal solution has been found, a fully-coupled OM analysis has been performed on the cavity-slab system. Even though the geometry of the cavity has not been changed since the one presented in chapter II, the above mentioned analysis had to be repeated because the presence of the slab acts as a perturbation to the optical resonating mode, slightly changing the resonating frequency.

For what concerns the coherent phonons extraction, basing on [28] a structure made of a Si-slab (acting as a phonon waveguide) surrounded by phonon shielding block, which have been tuned to the selected operating frequency for stopping any mechanical leaking, has been proposed and investigated. It has been observed that, in comparison with the design of [28], the proposed system cavity-phononic waveguide provides a much higher population of coherent phonons flowing out of the resonating cavity, and this is due to the lower Q-factor of the latter that provides a weaker level of confinement.

5.3 SAW as a phonon processing alternative

Chapter IV tackles the issue of defining a device capable of shooting SAWs either into an i) OM cavity or ii) slab, e.g. the conversion of electrically generated RF mechanical waves into either confined mechanical or guided phononic modes.

The main outcome of the study is the design of a structure presenting radially curved fingers of IDT capable of reaching a conversion efficiency of ~ -22 dB, which is a value perfectly reasonable to be experimentally observed [32]. The results that have been obtained are in line with the ones related to a ZnO-based piezoelectric system, where an efficiency of 1% was reached [32]. It must be anyway underlined that, contrary to [32], i) the investigated system converts SAW into guided modes in a Si-

Chapter 5 Conclusions

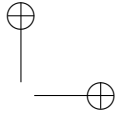
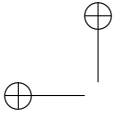
slab, and such conversion surely affects the efficiency of the overall system, and ii) it is, in theory, possible to reduce the return loss either by applying a Bragg mirror to the slab section or by increasing the complexity of the IDT fingers geometry (one may think, for example, of using double fingers).

For what concerns the injection of mechanical energy into an OM cavity by using a SAW, this study numerically demonstrated the possibility of doing so with an acceptable level of efficiency, which sets a key-point that may pave the road for multiple possibilities. For example, one may think on electrically pumping phonons into a mechanical cavity when the standard OM-approach is not feasible for either technological or design-like reasons. The electrically-driven OM cavity can then be mechanically coupled to other cavities [33], which would form a complex on-chip excitation system. Another possible usage for the SAW/OM configuration is the incoming phonons detection: if the considered cavity is supposed to act as the recipient for coherent phonons traveling along a phononic waveguide, SAWs could transfer such information to an electrical system, which may subsequently interface the OM system to a standard Si-based technology chip.

The second part of chapter IV presents a novel numerical approach for characterizing the electrical excitation of SAW, where the transition from IDT terminals to mechanical waves in matter has been described by means of a general circuit representation that makes use of SM formalism [31]. By using the TRL approach, which is largely spread among the RF community thanks to its efficiency and simplicity, the numerical simulations successfully emulate the experimental conditions of a SAW based device when measured, allowing for the de-embedding of numerous acoustic components as filters or resonators from the outer IDT structure (regardless of complexity and size of the latter). For a first verification of the obtained results, an independent analytic approach has also been developed, and the outcomes have been satisfactorily matched with the numerical ones. The proposed approach has been tested on the rather simple example of a suspended Si-membrane used as a mechanical waveguide, which has been carefully designed to support only the propagating mode. Given its versatility, the developed numerical method may serve as an efficient tool for both the synthesis and optimization of SAW-based devices.

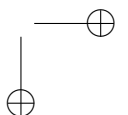
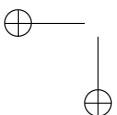
5.4 Final conclusions

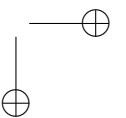
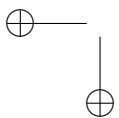
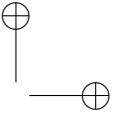
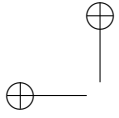
In this thesis, the theoretical investigation of various OM-based components has been performed by means of both analytic and numerical methods. In particular, this research focuses on the design of i) phonon generators, ii) phonon detectors and iii) phonon waveguides, having the aim of proposing numerical tools capable of rigorously predicting the behavior of an OM system rather than simply predicting, in a qualitative way, the strength of the coupling between the two physics of EM and mechanics. In order to create a complete simulation environment, capable for example of simulating



5.4 Final conclusions

an entire OM circuit (and therefore to reach the level of a Cadence or an ADS for a circuit designer), further efforts must be put on the simplified description of the OM behavior of each component, e.g. from its circuitual representation.





Bibliography

- [1] M. Aspelmeyer, S.Gröblacher, K.Hammerer and N.Kiesel, “Quantum optomechanics—throwing a glance,” *J. Opt. Soc. Am.*, **B27**, pp. 189—197 , 2010.
- [2] F. Marquardt and S.M.Girvin, “Optomechanics (a brief review),”, *arXiv:0905.0566*.
- [3] M.V.Gustafsson, T.Aref, A.F.Kockum, M.K.Ekstrom, G.Johansson and P. Delsing, “Propagating phonons coupled to an artificial atom,” *Science*, vol. 346, no. 207, 2014.
- [4] M.J.A.Schuetz, E.M.Kessler, G.Giedke, L.M.K.Vandersypen, M.D.Lukin and J. I. Cirac, “Universal Quantum Transducers Based on Surface Acoustic Waves,” *Physical Review X*, vol. 5, no. 031031, 2015.
- [5] E.R.MacQuarrie, T.A.Gosavi, N.R.Jungwirth, S.A.Bhave, and G.D.Fuchs, “Mechanical Spin Control of Nitrogen-Vacancy Centers in Diamond“, *Physical Review Letters* , vol. 111, no. 227602, 2013.
- [6] O.O.Soykal, R.Ruskov, and C.Tahan, “Sound-Based Analogue of Cavity Quantum Electrodynamics in Silicon,“ *Physical Review Letters* , vol. 107, no. 235502, 2011.
- [7] S.D.Bennett, N.Y.Yao, J.Otterbach, P.Zoller, P.Rabl, and M.D.Lukin, “Phonon-Induced Spin-Spin Interactions in Diamond Nanostructures: Application to Spin Squeezing,” *Physical Review Letters*, vol. 110, no. 156402, 2013.
- [8] D.Leibfried, R.Blatt, C.Monroe, and D.Wineland, “Quantum dynamics of single trapped ions,” *Review of Modern Physics* , vol. 75, no. 281, 2003.
- [9] D.J.Wineland, “Nobel Lecture: Superposition, entanglement, and raising Schrodinger’s cat,” *Review of Modern Physics*, vol. 85, no. 1103, 2013.
- [10] M.Aspelmeyer, T.J.Kippenberg, and F.Marquard, “Cavity optomechanics“, *Reviews of Modern Physics*, vol. 86, no. 1391, 2014.
- [11] M.Metcalf, “Applications of cavity optomechanics“, *Applied Physics Reviews*, vol. 1, no. 031105 , 2014.

Bibliography

- [12] K.Fang, M.H.Matheny, X.Luan and O.Painter, “Optical transduction and routing of microwave phonons in cavity-optomechanical circuits“, *Nature Photonics*, vol. 10, pp. 489—496 , 2016.
- [13] L. Pierantoni, D. Mencarelli, M. Stocchi, “Rigorous simulation of optomechanically modulated electromagnetic micro- and nano-cavities“, *Proc. of the 17th IEEE International Conference on Nanotechnology (IEEE NANO 2017)*, July 25-28, 2017, Pittsburgh, PA, USA.
- [14] J. B. Pendry; D. Schurig and D. R. Smith, “Controlling Electromagnetic Electromagnetic Fields,“ *Science*, vol. 312, no. 5514 , 2006.
- [15] C.Wolff, M.J.Steel, B.J.Eggleton, and C.G.Poulton, “Stimulated Brillouin Scattering in integrated photonic waveguides: forces, scattering mechanisms and coupled mode analysis,“ *Physical Review A*, vol. 92, no. 013836 , 2015.
- [16] R.Zecca, P.T.Bowen, D.R.Smith, S.Larouche, “Transformation-optics simulation method for stimulated Brillouin scattering,“ *Phys. Rev. A*, vol. 94, no. 063818 , 2016.
- [17] D.Schurig, “Metamaterial Electromagnetic Cloak at Microwave Frequencies,“ *Science*, vol. 314, no. 5801 , 2006.
- [18] R. W. Boyd, “Nonlinear optics,“ *Academic Press, 2008) Chap. 9, pp. 429, 3rd Ed.*
- [19] O. Gonzalez and A. M. Stuart, “A first course in continuum mechanics,“ (*Cambridge University Press, 2008) Chap. 3, 5, pp. 94, 179–193, 1st ed.*
- [20] W. Qiu, P. T. Rakich, H. Shin, H. Dong, M. Soljačić and Z. Wang, “Stimulated Brillouin scattering in nanoscale silicon step-index waveguides: a general framework of selection rules and calculating SBS gain,“ *Optics Express*, vol. 21, no. 25 , 2013.
- [21] B. D. Hauer, C. Doolin, K. S. D. Beach and J. P. Davis, “A general procedure for thermomechanical calibration of nano/micro-mechanical resonators,“ *arXiv:1305.0557*.
- [22] G. Bahl, M. Tomes, F. Marquardt and T. Carmon, “Observation of spontaneous Brillouin cooling,“ *Nature Physics*, vol. 8, 2012.
- [23] D. Navarro-Urrios, J. Gomis-Bresco, S. El-Jallal, M. Oudich, A. Pitanti, N. Capuj, A. Tredicucci, F. Alzina, A. Griol, Y. Pennec, B. Djafari-Rouhani, A. Martinez and C. M. Sotomayor Torres “Dynamical back-action at 5.5 GHz in a corrugated optomechanical beam,“ *AIP Advances*, vol. 4, no. 124601, 2014.

Bibliography

- [24] J. Gomis-Bresco, D. Navarro-Urrios, M. Oudich, S. El-Jallal, A. Griol, D. Puerto, E. Chavez, Y. Pennec, B. Djafari-Rouhani, F. Alzina, A. Martínez and C.M. Sotomayor Torres “A one-dimensional optomechanical crystal with a complete phononic band gap“ *Nat. Comm.*, vol. 5, no. 4452, 2014.
- [25] S. J. Johnson, M. Ibanescu, M. A. Skorobogatiy, O. Weisberg, J.D. Joannopoulos and Y.Fink “Perturbation theory for Maxwell’s equations with shifting material boundaries“ *Phys. Rev. E*, vol. 65, no. 066611, 2002.
- [26] P. T. Rakich, P. Davids and Z. Wang “Tailoring Optical Forces in Waveguides Through Radiation Pressure and Electrostriction“ *Opt. Expr.*, vol. 18, no. 14, 2010.
- [27] M. Stocchi, D. Mencarelli, Y. Pennec, B. Djafari-Rouhani and L. Pierantoni "Rigorous simulation of nonlinear optomechanical coupling in micro- and nano-structured resonant cavities" *Int. Jou. of Optomechatronics*, vol. 12, pag. 11-19, 2018.
- [28] J. Chan, A. H. Safavi-Naeini, J. T. Hill, S. Meenehan and O. Painter, "Optimized optomechanical crystal cavity with acoustic radiation shield," *Appl. Phys. Lett.*, vol. 101, no. 081115, 2012.
- [29] M. Stocchi, D. Mencarelli and L. Pierantoni, "Transformation Optics: Large Multiphysics Simulation of Nonlinear Optomechanical Coupling in Microstructured Resonant Cavities," *IEEE Microwave Magazine*, vol. 19, no. 5, pp. 79-84, 2018.
- [30] A. V. Korovin, Y. Pennec, M. Stocchi, D. Mencarelli, L. Pierantoni, T. Makkonen, J. Ahopelto and B. Rouhani Djafari, "Conversion between surface acoustic waves and guided modes of a quasi-periodic structured nanobeam," *Journal of Physics D: Applied Physics*, vol. 52, no. 32, pp. 32LT01, 2019.
- [31] D. Mencarelli, B. Rouhani Djafari, Y. Pennec, A. Pitanti, S. Zanotto, M. Stocchi and L. Pierantoni, "Numerical emulation of Thru-Reflection-Line calibration for the de-embedding of Surface Acoustic Wave devices," *Scientific Reports*, vol. 8, no. 9256, 2018.
- [32] K. Y. Hashimoto, “Surface Acoustic Wave Devices in Telecommunications“ *Spring. Pub.*, 2000.
- [33] M. Colombano Sosa, G. Arregui Bravo, N. Capuj, A. Pitanti, J. Marie, A. Griol, B. Garrido, A. Martinez, C. Sotomayor Torres and D. Navarro-Urrios, "Synchronization of Optomechanical Nanobeams by Mechanical Interaction," *Physical Review Letters*, vol. 123, no. 7, 2019.

Bibliography

- [34] D. Fuhrmann, S. Thon, H. Kim et al. "Dynamic modulation of photonic crystal nanocavities using gigahertz acoustic phonons". *Nature Photon*, vol. 5, pag. 605–609, 2011.
- [35] K. Balram, M. Davanço, J. Song et al. "Coherent coupling between radiofrequency, optical and acoustic waves in piezo-optomechanical circuits". *Nature Photon*, vol. 10, pag. 346–352, 2016.
- [36] K. Balram et al. "Acousto-Optic Modulation and Optoacoustic Gating in Piezo-Optomechanical Circuits". *Phys. Rev. Applied*, vol. 7, no. 2, pag. 024008, 2017.
- [37] A. Vainsencher et al. "Bi-directional conversion between microwave and optical frequencies in a piezoelectric optomechanical device". *App. Phys. Lett.*, vol. 109, no. 3, pag. 033107, 2016.
- [38] Bhattacharyya, A. B., Tuli, S. and Majumdar, S. "SPICE Simulation of Surface Acoustic Wave Interdigital Transducers". *IEEE Transactions on Ultrasonics, Ferroelectrics, and Frequency Control*, vol. 40, no. 6, pag. 784–786, 1995.
- [39] Soluch, W. "Admittance Matrix of a Surface Acoustic Wave Interdigital Transducer". *IEEE Transactions on Ultrasonics, Ferroelectrics, and Frequency Control*, vol. 40, no. 6, pag. 828–831, 1993.
- [40] Moszynski, M., Lis, W. "A Spice equivalent circuit for modelling the performance of dual frequency echo-sounder". *Hydroacoustics*, vol. 14, pag. 165–170, 2011.
- [41] Y. A. V. Espinel, F. G. S. Santos, G. O. Luiz, T. P. Mayer Alegre and G. S. Wiederhecker, "Brillouin Optomechanics in Coupled Silicon Microcavities," *Sci. Rep.*, vol. 7, no. 43423, 2017.